




Cite this: *Chem. Soc. Rev.*, 2018, **47**, 6296

## 2D library beyond graphene and transition metal dichalcogenides: a focus on photodetection

Feng Wang,<sup>†a</sup> Zhenxing Wang,<sup>†a</sup> Lei Yin,<sup>ab</sup> Ruiqing Cheng,<sup>ab</sup> Junjun Wang,<sup>ab</sup> Yao Wen,<sup>ab</sup> Tofik Ahmed Shifa,<sup>ab</sup> Fengmei Wang,<sup>a</sup> Yu Zhang,<sup>a</sup> Xueying Zhan<sup>a</sup> and Jun He <sup>\*,ab</sup>

Two-dimensional layered materials (2DLMs) have attracted a tremendous amount of attention as photodetectors due to their fascinating features, including high potentials in new-generation electronic devices, wide coverage of bandgaps, ability to construct van der Waals heterostructures, extraordinary light–mass interaction, strong mechanical flexibility, and the capability of enabling synthesis of 2D nonlayered materials. Until now, most attention has been focused on the well-known graphene and transition metal dichalcogenides (TMDs). However, a growing number of functional materials (more than 5619) with novel optoelectronic and electronic properties are being re-discovered, thereby widening the horizon of 2D libraries. In addition to showing common features of 2DLMs, these new 2D members may bring new opportunities to their well-known analogues, like wider bandgap coverage, direct bandgaps independence with thickness, higher mechanical flexibility, and new photoresponse phenomena. The impressive results communicated so far testify that they have shown high potentials with photodetections covering THz, IR, visible, and UV ranges with comparable or even higher performances than well-known TMDs. Here, we give a comprehensive review on the state-of-the-art photodetections of two-dimensional materials beyond graphene and TMDs. The review is organized as follows: fundamentals of photoresponse first are discussed, followed by detailed photodetections of new 2D members including both layered and non-layered ones. After that, photodiodes and hybrid structures based on these new 2D materials are summarized. Then, the integration of these 2D materials with flexible substrates is reviewed. Finally, we conclude with the current research status of this area and offer our perspectives on future developments. We hope that, through reading this manuscript, readers will quickly have a comprehensive view on this research area.

Received 3rd April 2018

DOI: 10.1039/c8cs00255j

[rsc.li/chem-soc-rev](http://rsc.li/chem-soc-rev)

<sup>a</sup> CAS Center for Excellence in Nanoscience, CAS Key Laboratory of Nanosystem and Hierarchical Fabrication, National Center for Nanoscience and Technology, Beijing 100190, China. E-mail: [hej@nanoctr.cn](mailto:hej@nanoctr.cn)

<sup>b</sup> University of Chinese Academy of Sciences, Beijing 100049, P. R. China

<sup>†</sup> These two authors contributed equally to this work.



**Feng Wang**

*Dr Feng Wang received his Bachelor's and Master's degrees from Yanshan University in 2010, and Zhejiang University in 2013, respectively. Then he worked as a Research Assistant in the Department of Mechanical and Automation Engineering, the Chinese University of Hong Kong. After receiving PhD degree in 2013, he continued doing research in the National Center for Nanoscience and Technology. His current research interest is developing two-dimensional materials for electronic and optoelectronic applications.*



**Zhenxing Wang**

*Dr Zhenxing Wang received his BS and PhD degrees from University of Science and Technology of China (USTC) in 2002 and 2009, respectively. After two-year post-doctoral work at Peking University, he joined the National Center for Nanoscience and Technology (NCNST) in 2011, where currently he is a Professor. His current research interests focus on low dimensional materials, properties and optoelectronic devices.*

# 1. Introduction

Photodetectors are sensors that detect photons (or electromagnetic waves) and transfer them to electric signals. According to the wavelength of the responsive spectra, photodetectors can work at UV (ultraviolet, 10–300 nm), visible (400–700 nm), IR (infrared, 700 nm–1 mm), and THz (0.1 to 1 mm, or 0.3 to 30 THz) ranges with various applications that play indispensable roles in our daily life.<sup>1–3</sup> Several conventional semiconductors with appreciable properties like suitable bandgaps have been used as photo-sensitive materials to construct photodetectors. For instance, Si has been widely used for visible and NIR (near infrared) light detection because of the ease of synthesis and, more importantly, its compatibility with well-developed Si-based circuits technologies. However, Si has a bandgap of  $\sim 1.1$  eV, which means it can't absorb most of the IR spectrum. In addition, due to its indirect bandgap nature which gives rise to a quadratic dependence of absorption coefficient on photon energy, Si has a relatively weak absorption (only exceeding  $10^4$  cm<sup>-1</sup> at 500 nm).<sup>4</sup> In another case, Hg<sub>x</sub>Cd<sub>1-x</sub>Te has been commercially utilized for IR detection owing to a tailorable bandgap over the 1–30  $\mu$ m range, large optical coefficients that enable high quantum efficiency, and favourable inherent recombination mechanisms that lead to high operating temperatures.<sup>5</sup> Nevertheless, an additional cooling system (at least 77 K) is still needed, which largely restricts their applications in portable devices. As a result, new strategies including the use of novel materials with advanced structures are crucially sought.

Two-dimensional layered materials (2DLMs), or van der Waals materials, referring to the materials family that naturally have van der Waals gaps between chemically bonded atomic layers (in some special cases like the Bi<sub>2</sub>O<sub>2</sub>Se family, there is no van der Waals gap but weak electrostatic forces exist<sup>6</sup>), are one of the recently developed candidates for these new-generation photodetectors.<sup>7–10</sup> Sharing the feature of van der Waals

structure, 2DLMs have the following advantages in photodetectors: the first is the potentials they have shown on constructing these new-generation electronic devices, which is mainly because of their high charge carrier mobility, nearly perfect switching performance, strong gate voltage controllability, and immunity to the short-channel effect, *etc.*<sup>11</sup> Hence, photodetectors based on these new stars are straightforward expected. The second advantage relies on the wide coverage of their bandgaps originating from both the extremely diversified members in this family and extraordinary tunability by thickness, external strain, electric field, *etc.* Furthermore, different 2DLMs building blocks can even be stacked together to form so-called van der Waals heterostructures (vdWHs) through weak van der Waals forces, whereby the lattice mismatch requirement is waived, hence providing a platform that can combine different properties of the components together to achieve outcomes that individual(s) can't accomplish.<sup>12–14</sup> In addition, even though they have atomically thin thickness, many 2DLMs may have strong light–matter interaction due to their special band structures. For instance, due to the existence of Dirac cones, the absorption of monolayer graphene (G) is independent with the wavelength of the incident white light but solely determined by the fine structure constant, which gives rise to a high absorption of  $\sim 2.3\%$ .<sup>15</sup> On the other hand, most TMDs have the so-called van Hove singularities in their band structures, also leading to strong light–matter interactions.<sup>16</sup> Moreover, considering the beam theory, the ultrathin body thickness of 2DLMs brings them high flexibility providing an opportunity to fabricate wearable devices.<sup>17</sup> Besides, novel photoresponse phenomena and new mechanisms may result with these materials, like a strong photogating effect which can induce high gain,<sup>18</sup> polarization selected photodetection due to strong anisotropic properties,<sup>19</sup> and naturally hyperbolic properties which can be utilized for nano-imaging,<sup>20</sup> *etc.* Finally, but not the end, the rise of 2DLMs also makes the synthesis of 2D non-layered materials (which are isotopically bonded by strong chemical bonds) possible, which further extends the definition and properties of 2D materials.<sup>21</sup> Meanwhile, 2DLMs also enable transferable synthesis of conventional semiconductor nanostructures and/or films, like GaAs and GaN in the III–V group,<sup>22</sup> *via* using ultrathin 2DLMs as van der Waals buffer layers, which further makes possible the integration of these traditional materials with arbitrary substrates like flexible polymers.

Initially, 2DLMs-based photodetectors mainly focused on the well-known G and TMDs (transition metal dichalcogenides).<sup>23–31</sup> However, as time went on, more and more materials with novel optoelectronic and electronic properties were being re-discovered and joined the big 2D family. Very recently, Mounet and his colleagues predicted that about 5619 compounds naturally appear layered and 1036 of them can be easily exfoliated like G.<sup>32</sup> These identified compounds include (semi)metals, semiconductors with variable band structures, magnets, ferroelectrics, *etc.* Hence, it is eagerly anticipated to see what these 2DLMs beyond G and TMDs can bring to us. As candidates for photodetectors, these new 2D members (both layered and non-layered) may possess additional advantages/features compared with their



Jun He

*Dr Jun He received his PhD in Semiconductor Physics from the Institute of Semiconductors, Chinese Academy of Sciences (CAS), in 2003. Then he worked successively at Applied Physics Department of Technische Universiteit Eindhoven, Netherlands, Material Department of University of California, Santa Barbara, and California NanoSystem Institute (CNSI), University of California, Los Angeles, USA. He joined the “100-Talents” Program*

*of CAS in Nov. 2010 and became a Full Professor of the National Center for Nanoscience and Technology since then. His main research interest is the synthesis, characterization, and devices of low dimensional semiconductor materials.*

well-known analogues. For example, most TMDs become direct bandgap semiconductors only while thinning down to monolayers. However, many of the newcomers have intrinsic direct bandgaps, such as GaTe and BP.<sup>33,34</sup> In addition, the bandgaps of semiconducting TMDs only cover a finite range of  $\sim 1$ – $2.4$  eV, which largely restricts their applications. As a result, other 2D materials can provide an important supplement. Fig. 1a summarizes bandgaps distributions of selected 2DLMs, which clearly demonstrates the supplementary role of these new 2DLMs. Furthermore, these new members may even bring new possibilities. For instance, the topologically protected surface states (SS) of 2D topological insulators like  $\text{Bi}_2\text{Se}_3$  endow wavelength-independent high absorption in the IR to THz range.<sup>35</sup> In another case, some of these newcomers may have better mechanical flexibility than TMDs. Based on the common advantages of 2DLMs and special properties that the new members have, studies of their photodetections are really anticipated.

Until now, a number of these new 2DLMs have been studied by both theoretical and experimental methods. They include elementals, main group metal chalcogenides (MMCs), transition

metal trichalcogenides (TMTs), tetradymites, metal halides (MHs), transition metal chalcogenophosphates (TMCPs), *etc.* However, due to their relatively short history, some of them are recently rediscovered and their photoresponse properties have not been fully studied. Nevertheless, based on the finite results, they have shown high potentials in photodetections covering THz, IR, visible, and UV ranges with comparable or even higher performances than well-known TMDs (Fig. 1b and c summarize reported values of responsivity of selected members). As a result, a comprehensive overview on this arising area is needed.

Here, we give a brief review on state-of-the-art photodetections of two-dimensional materials beyond graphene and TMDs with the manuscript's organization stated as below. Fundamentals of photoresponse, including response mechanisms and figure of merits to evaluate their photodetection performances are first introduced. After that, the photodetections of these new 2D members that are divided into two big categories, *i.e.*, 2DLMs and 2D non-layered materials, will be discussed in detail. In each part of this section, basic properties, including the crystalline structures, band structures, and

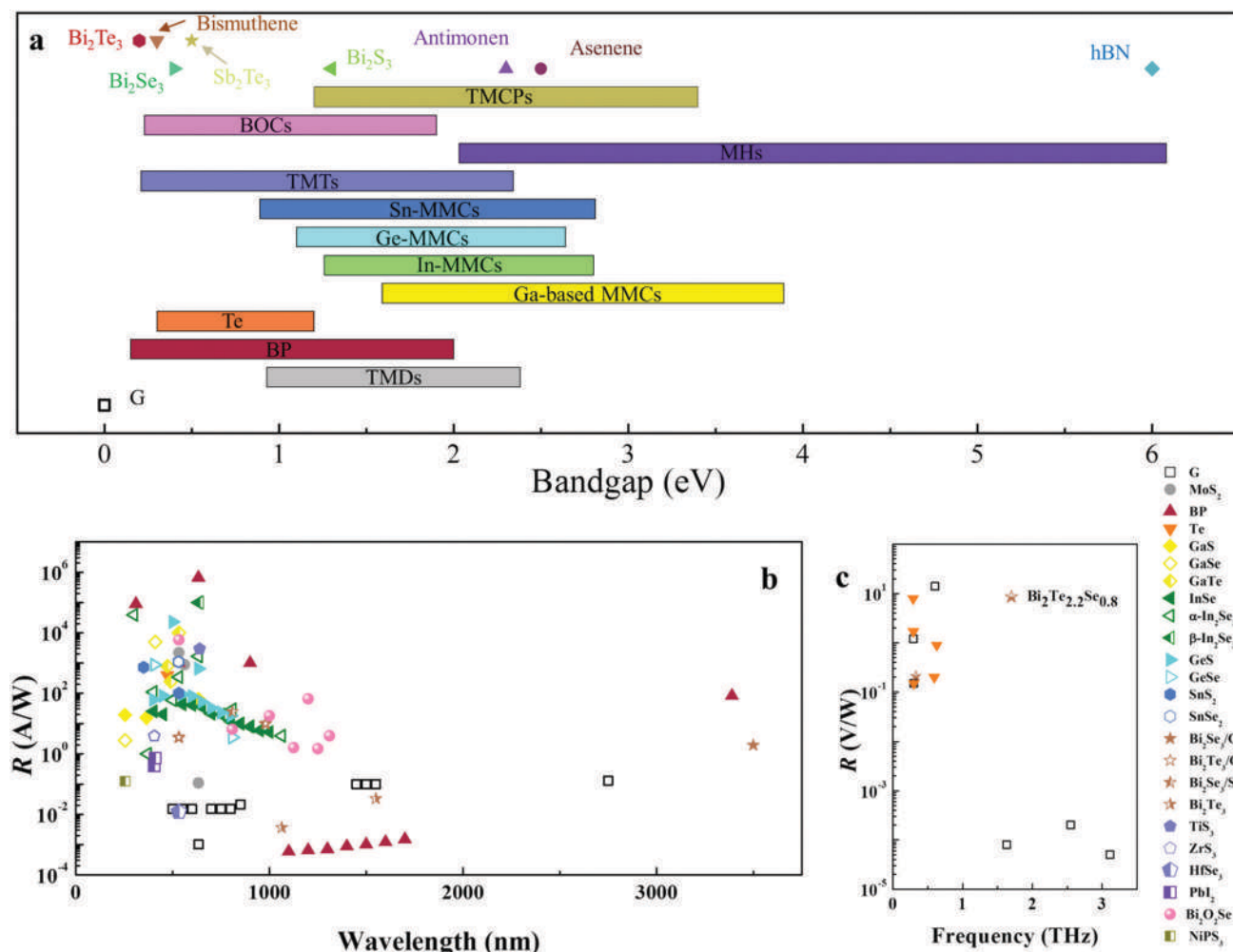


Fig. 1 Summary of the (a) bandgaps as well as responsivities to the (b) visible and IR and (c) THz ranges of selected 2DLMs. Data are extracted from the literatures. Please see the corresponding sections for details.

absorptions, are illustrated before discussions of the corresponding photodetections. Here, considering the variety of figure of merits and calculation methods (detectivity for example) used to evaluate performances of photodetectors on 2D materials, the most basic parameter of responsivity is used as the main clue. In the fifth part, we give an overview on photodiodes and hybrid structures based on these new 2D materials. Then, the integration of these 2D materials with flexible substrates is discussed. Finally, conclusions on the conditions of the research area and perspectives on future developments are provided.

## 2. Fundamentals

According to the mechanisms of switching from photons to electrical signals, a photoresponse can be classified as several types: photovoltaic effect, photoconductive effect, photogating effect, photo-thermoelectric effect, and bolometric effect, *etc.* Here, a brief introduction of the various detection mechanisms will be given. Following that, commonly used parameters to evaluate the performances of photodetectors are summarized.

### 2.1 Mechanisms of photoresponse

**2.1.1 Photovoltaic effect (PVE).** This refers to the generation of electrical potential difference at the existence of built-in junctions (space area), like p-n and Schottky junctions, under light illumination. Taking p-n junction as an example, when the incident photon energy ( $h\nu$ , where  $h$  and  $\nu$  are Planck constant and frequency of the light) is higher than the semiconductor bandgap ( $E_g$ ), then photo-generated carrier (electron-hole) pairs can be separated spontaneously by built-in electric fields at the interface of the junction and accumulated on the edge of the junction. As a result, a photostimulated electric field opposite to the direction of the built-in electric field will be formed, which is equivalent to producing a positive photovoltage (open-circuit voltage,  $V_{oc}$ ). On the other hand, photo-generated carriers could flow along the external circuit and generate a photocurrent (short-circuit current,  $I_{sc}$ ) when a p-n junction is short-circuit connected ( $V_{DS} = 0$  V, here  $V_{DS}$  refers to the source-drain voltage). On the basis of the photovoltaic effect, photodiodes (PN photodiodes, PIN photodiodes, Schottky photodiodes, *etc.*) have been developed for photodetection.

In general, photodiodes work at a modest reverse bias condition *i.e.*, avalanche breakdown voltage  $< V_{DS} < 0$  V, that benefits a shortened carrier transit time and lower diode capacitance. Besides, owing to the rectification characteristic of p-n and Schottky junctions, the dark current under reverse bias is low so that a high detectivity ( $D^*$ , see below) can be realized. Note that there is no gain in a majority of photodiodes (due to the fast sweep of carriers in the space area) except for avalanche photodiodes (APDs). An APD is based on the avalanche effect under a large reverse bias. Under illumination, photo-generated carriers will be accelerated by the larger reverse bias, giving rise to additional electron-hole pair generation through collisional ionization. As a result, high current gain can be achieved in APDs.<sup>36</sup> In addition, phototransistors

(here this refers to bipolar junction transistors) working with a photovoltaic effect also exhibit a considerable photocurrent gain.<sup>37</sup>

**2.1.2 Photoconductive effect.** Different from PVE, a photoconductive effect (PCE) stems from the light-induced modification of carrier density of photosensitive materials, thus leading to a change in its conductivity. Photodetectors based on PCE are usually known as photoconductors (and photo-field effect transistors, photo-FETs). We note that some literature references call the PCE at the existence of an external field also as PVE. However, for a better distinction, here we separate them into two categories. Owing to the large amount of photo-generated carriers produced in the channel, recombination between the electrons and holes also are usually prominent. And the recombination rate increases with its quantity. For an effective separation of photoexcited electron-hole pairs by  $V_{DS}$ , ohmic contact is generally desired.

As for practical applications of photoconductive detectors, photoconductive gain and relaxation are two important aspects. The former reflects the magnitude of photoconductance and the latter shows the response speed of photoconductance to light intensity variation, both of which are related to the accumulation and disappearance processes of photo-generated carriers. Generally, the photoconductive gain ( $G$ ) can be described as the ratio of the photo-generated carrier lifetime ( $\tau_{\text{photocarries}}$ ) over the transit time ( $\tau_{\text{transit}}$ ):<sup>38</sup>

$$G = \frac{\tau_{\text{photocarries}}}{\tau_{\text{transit}}} = \frac{\tau_{\text{photocarries}} \cdot \mu \cdot V_{DS}}{L^2} \quad (1)$$

Here, the transit time is quantified by the formula:  $\tau_{\text{transit}} = L^2/\mu V_{DS}$ , where  $L$  and  $\mu$  are the separation distances of source-drain electrodes and the carrier mobility, respectively. Thus, the longer the carrier lifetime and the larger the carrier mobility the photosensitive materials have, the higher the photoconductive gain the photodetectors will have. However, a longer carrier lifetime will give rise to a prolonged relaxation time, reducing the response speed of the device. Therefore, it is essential to eclectically select the appropriate parameters according to the actual needs.

**2.1.3 Photogating effect.** Actually, a photogating effect (PGE) is a special case of the PCE. It generally exists in defective semiconductors or hybrid structures. According to the position of photo-electron-hole pairs generation, two cases can be differentiated. In the first case, photoexcited electron-hole pairs are generated in the semiconductor serving as a conducting channel. Subsequently, one type of the charge carriers (electrons or holes) is captured by the trap states inside the semiconductor or at the surface adsorbates. Using a defective n-type semiconductor with hole trap states as an example, photo-generated electrons contribute to the photocurrent, whereas photo-generated holes are trapped in the defects that cannot participate in photo-conducting but induce an extra gate voltage on the channel. In the second case, electron-hole pairs generate only in the surface adsorbates, and subsequently one type of charge carriers is transferred into the channel material. Both of these cases share a fact that the charge



carriers captured/kept could apply an additional gate voltage on the conducting channel, hence effectively modulating the resistance of channel. It's worth noting that the negative photoresponse may occur in PGE<sup>4,39</sup> with ambipolar channel materials.<sup>39,40</sup> Due to additional gate voltage resulting from the captured/kept charge carriers, gate voltage corresponding to the minimum current ( $V_{\min}$ ) in a transfer characteristic curve could be horizontally shifted. Consequently, the current on one side of  $V_{\min}$  increases (positive photoresponse), whereas a decrease of current (negative photoresponse) takes place in the opposite direction. In other words, if the increase in conductivity caused by the increase of carrier density is not higher than the decrease by the gating effect, a negative photoresponse will occur. Additionally, the lifetime of excess carriers becomes longer because of the capture of opposite carriers. Therefore, considering eqn (1), a large photogain can be achieved. This effect is particularly pronounced in low dimensional semiconductors due to a large surface-to-volume ratio and reduced screening effects.<sup>41</sup> Besides the PGE mentioned above, there are also other mechanisms that use a gating effect to achieve a photoresponse, like photovoltage field-effect transistor<sup>33</sup> and interfacial effect.<sup>42,43</sup>

**2.1.4 Photo-thermoelectric effect.** A photo-thermoelectric effect (PTE) involves a process in which a heat gradient from light-induced heating produces a temperature difference ( $\Delta T$ ) at the two ends of a photosensitive channel and leads to a photo-thermoelectric voltage difference ( $\Delta V_{\text{PTE}}$ ) by the Seebeck effect. The magnitude of the photo-thermoelectric voltage difference is determined by  $\Delta V_{\text{PTE}} = \Delta T \cdot (S_1 - S_2)$ , where  $S_{1,2}$  is the Seebeck coefficient.<sup>44</sup> To acquire an effective photo-thermoelectric signal in a photo-thermoelectric device with a homogeneous semiconductor, it must be locally illuminated with a focused laser spot to form a  $\Delta T$  between both of its ends. However, a photo-thermoelectric effect within the devices would not have been observed under global illumination due to uniform temperature distribution.

**2.1.5 Bolometric effect.** In a bolometric effect (BE), the resistivity of photosensitive materials is modified by the light heating effect. Under homogeneous illumination, the magnitude of this effect is associated with the conductance change of photosensitive materials with temperature ( $dG/dT$ ) and the homogeneous temperature increase ( $\Delta T$ ) caused by laser heating. When the gradient ( $dG/dT$ ) is greater than zero, a positive photoresponse (PP) arises and leads to an increasing photocurrent ( $I_{\text{PP}}$ ). On the contrary, a negative photoresponse (NP) is observed deriving from the negative gradient.<sup>45,46</sup>

**2.1.6 Pyro-phototronic effect.** The pyro-phototronic effect is a recently proposed photodetection mechanism based on pyroelectric effects.<sup>47-50</sup> It generally occurs in a crystal with spontaneous polarization properties. Under illumination, the transient temperature increase of photosensitive semiconductors will produce pyroelectric polarization potentials ( $V_{\text{pyro}}$ ), promoting photogenerated carrier separation. Until a new thermal equilibrium is established due to the sustained illumination, the  $V_{\text{pyro}}$  disappear gradually. Similarly, when shutting off light, the transient temperature reduction generates an opposite  $V_{\text{pyro}}$

with respect to light-induced  $V_{\text{pyro}}$ . As a result, a bump up in current is observed before backing to a dark state.

**2.1.7 THz detection.** Three main types of detectors, including homodyne (or direct), heterodyne, and optoelectronic detectors, have been utilized for THz response. Each is composed of a few numbers of subtypes.<sup>51</sup> For example, Golay cells, pyroelectric detectors, thermoelectric detectors, plasma-waves in field effect transistors (FETs), and bolometers are common types for homodyne detectors. So far, both thermoelectric and bolometric effects, and plasma-wave-assisted FET have been demonstrated in THz detectors based on two-dimensional materials.<sup>52-54</sup>

While there is an incoming THz radiation, ac current will be induced in a FET channel due to the excitation of 2D electron plasma in it. Hence, a photoresponse in the form of dc voltage may appear if the induced ac current was rectified by asymmetry in the FET.<sup>55,56</sup> This asymmetry can be due to different electrode contact conditions, or artificially designed asymmetric metal antennas. Especially, radiation applied between source and gate modulates both charge density and velocity. Depending on the radiation frequency and parameters of FET (life time and effective mass of charge carrier, gate length, and voltage bias), the THz detectors can work in resonant and nonresonant overdamped regimes. For the former, a plasma wave launched from one end of the channel can reach the other side before damping and forming a standing wave; hence, the channel acts as a resonator for plasma oscillations. In this regime, a FET exhibits a strong photoresponse. As for the latter, the plasma wave damps at a distance smaller than the channel length. However, from the point of view of practical applications, this regime is the most important case because FET detectors can show a broad band response and operate at room temperature.<sup>51</sup> THz detectors based on 2D FETs are also mainly focused on an overdamped regime. In addition, a properly designed metal antenna is usually used to enhance coupling capability between THz radiation and the devices. According to a diffusive hydrodynamic model, the generated photovoltage ( $\Delta U_{\text{F}}$ ) follows the relation:<sup>57</sup>

$$\Delta U_{\text{F}} = -\frac{a}{1 + \frac{R_{\text{CH}}}{Z}} \frac{d}{dV_{\text{GS}}} \ln[I_{\text{DS}}(V_{\text{GS}})] \quad (2)$$

where  $a$  is the coupling efficiency of the THz radiation to the antenna,  $R_{\text{CH}}$  is the resistance of the channel,  $Z$  is the complex impedance of the measurement setup,  $V_{\text{GS}}$  is the gate voltage, and  $I_{\text{DS}}$  is the drain current.

For a bolometric effect, the generated photovoltage ( $\Delta U_{\text{B}}$ ) is determined by:<sup>54,58</sup>

$$\Delta U_{\text{B}} = \frac{I_{\text{B}}}{\sigma} \propto \frac{\beta}{\sigma} = \frac{1}{\sigma} \frac{d\sigma}{dT} \quad (3)$$

where  $I_{\text{B}}$  is the bolometric effect induced current,  $\sigma$  is the conductivity, and  $\beta = d\sigma/dT$  is the bolometric coefficient with a positive/negative value meaning the positive/negative contribution to the current.

For a thermoelectric effect, the generated photovoltage ( $\Delta U_{\text{T}}$ ) is determined by the Seebeck coefficient ( $S$ ). Usually,  $S$  has the

form of:<sup>54</sup>

$$S = -\frac{\pi^2 k_B^2 T}{3q} \frac{1}{\sigma} \frac{d\sigma}{dV_{GS}} \frac{dV_{GS}}{dE_F} \quad (4)$$

where  $k_B$  is the Boltzmann constant,  $q$  is the elementary electron charge, and  $E_F$  is the Fermi energy.

For a practical FET-based THz detector, a photoresponse is usually a combination of mechanisms mentioned above. To elucidate the dominant or the contribution of each mechanism, a commonly adopted way is to compare experimentally measured results with theoretically predicted ones.<sup>52–54</sup>

## 2.2 Figure of merits

**2.2.1 Photocurrent ( $I_{ph}$ ).** The photocurrent of a photodetector can be defined by a phenomenological formula:<sup>38</sup>

$$I_{ph} = I_{illumination} - I_{dark} = \frac{P_{in} \eta \mu q E \tau_{photocarriers}}{h\nu L} \quad (5)$$

where  $P_{in}$  is the incident light power,  $h$  is Planck constant,  $\nu$  is the frequency of incident light,  $\eta$  is quantum efficiency, *i.e.*, is the ratio between the number of generated electron–hole pairs and the amount of incident photons,  $E$  is the strength of electric field, and  $L$  is the separation distance of source–drain electrodes. For photodetectors without trap states, the photocurrent exhibits a linear dependence on the incident light power before saturated absorption is reached. In other words, the exponent  $\alpha$ , calculated by  $I_{ph} \propto P_{in}^\alpha$ , is equal to 1 or very close to 1. Otherwise, a nonlinear photoresponse ( $0 < \alpha < 1$ ) implies the intricate process of carrier generation, trapping, and recombination within semiconductors.<sup>41</sup>

**2.2.2 Responsivity ( $R$ ).** Responsivity is the ratio of the photocurrent ( $I_{ph}$ ) or photovoltage ( $V_{ph}$ ) to the incident power density ( $P_{in}$ ), in units of  $A W^{-1}$  or  $V W^{-1}$ . It can be expressed as:

$$R = \frac{I_{ph} \text{ or } V_{ph}}{P_{in} A} \quad (6)$$

where  $A$  is the effective illumination area of devices. This parameter describes the ability of photoelectric conversion in photodetectors.<sup>33,59</sup>

**2.2.3 Gain ( $G$ ).** Gain represents the number of detected charge carriers per single incident photon and is given by:

$$G = \frac{I_{ph}/q}{\eta P_{in}/h\nu} = R \frac{hc}{\eta q \lambda} \quad (7)$$

where  $c$  is the light velocity and  $\lambda$  is the excitation wavelength, and  $\eta$  is quantum efficiency. When  $\eta$  is ignored (assuming 100%), then gain is equivalent to the external quantum efficiency.

**2.2.4 External quantum efficiency (EQE).** External quantum efficiency is equal to the number of electron–hole pairs producing a photocurrent divided by the number of incident photons. The formula can be written as:

$$EQE = \frac{I_{ph}/q}{P_{in}/h\nu} = R \frac{hc}{q\lambda} \quad (8)$$

In many cases, the calculated EQE or  $G$  is larger than one, *i.e.*, more than one carrier is induced by an incident photon.

Actually, this is because the photo-generated carrier lifetime is longer than the transit time, stemming from the charge trapping and/or mobility difference between electron and hole. As a result, electron (hole) repeatedly contributes to the current until recombination or hole (electron) extraction.

**2.2.5 Internal quantum efficiency (IQE).** IQE is the ratio of the number of electron–hole pairs producing a photocurrent to the number of absorbed photons. Note that photon absorption in an ultrathin photosensitive layer can be strengthened through optical interference effects.<sup>60,61</sup> To accurately assess the number of photon absorptions and IQE, these effects should be considered.

**2.2.6 Signal to noise ratio (SNR).** Signal to noise ratio refers to the ratio of signal power and noise power in a photodetector. It is in units of decibel (dB) and described as:

$$SNR = \frac{\text{signal power}}{\text{noise power}} \quad (9)$$

Low noise is beneficial to extend the lower limit value of detectable signals. Therefore, a highly sensitive photodetector requires a high value of SNR.

**2.2.7 Noise equivalent power (NEP).** Noise equivalent power is defined as the minimum incident radiation power demanded to realize an SNR of 1 in a 1 Hz bandwidth. Normally, it is commonly expressed in  $W Hz^{-1/2}$ . The NEP also can be calculated by:

$$NEP = \frac{\overline{i_n^2}^{1/2} \text{ or } \overline{v_n^2}^{1/2}}{R} \quad (10)$$

where  $\overline{i_n^2}^{1/2}$  and  $\overline{v_n^2}^{1/2}$  is the mean-square noise current and mean-square noise voltage measured at the bandwidth of 1 Hz in darkness (in  $A Hz^{-1/2}$  and  $V Hz^{-1/2}$ ). From this equation we see that a smaller NEP implies a low noise signal and a large responsivity. As a result, the smaller the NEP is, the better the performance a detector has.

**2.2.8 Specific detectivity ( $D^*$ ).** Specific detectivity characterizes the capacity of detection for the lowest optical singles. The  $D^*$  of a photodetector is expressed as:

$$D^* = \frac{\sqrt{AB}}{NEP} \quad (11)$$

where  $A$  and  $B$  are the area and bandwidth of photodetectors. It is expressed in units of Jones ( $cm Hz^{1/2} W^{-1}$ ). When normalizing per square root of the area and bandwidth of the photodetector, the specific detectivity is equal to the reciprocal of NEP. If the total noise is assumed to be principally contributed by shot noise from the dark current, the  $D^*$  can be given by:

$$D^* = \frac{A^{1/2} R}{(2eI_d)^{1/2}} \quad (12)$$

where  $I_d$  is the dark current. Thus, a photosensitive material with a low dark current will benefit achieving a large  $D^*$  in a photodetector. Notably, a calculated  $D^*$  according to the assumption is at least one order of magnitude larger than the true measured values.<sup>62</sup>

**2.2.9 Response time ( $\tau$ ).** Response time reflects the speed of photodetectors to follow a light intensity variation. Generally, there are two methods to determine the rise time ( $\tau_r$ ) and decay/fall time ( $\tau_d$ ). In the first, the rise time and decay time are defined as the required time that photocurrent rise (decay) from 10% (90%) to 90% (10%) of the entire current increment. In the second, they are extracted by fitting the rising and falling parts of the time-resolved photoresponse using a single exponential function:<sup>63</sup>

$$I = I_{\text{pho}} e^{-(\tau/t)\beta} \quad (13)$$

where  $I_{\text{pho}}$  is the photocurrent when switching off the light and  $\beta$  is an exponent reflecting the relaxation mechanism. Response time is strongly associated with trap states and metal contact.<sup>64,65</sup> The response time of photodetectors based on layered material is universally in a micro- to millisecond level nowadays.<sup>66</sup>

### 3. Photodetectors based on 2D layered materials

These materials share a layered structure with intrinsic van der Waals gaps like G and TMDs, including elementals, main group metal chalcogenides (MMCs, with stoichiometric ratios between metals and chalcogenides of 1:1, 1:2, and 2:3), transition metal trichalcogenides (TMTs), tetradymites, metal halides (MHs), transition metal chalcogenophosphates (TMCPs), Bi-based oxychalcogenides (BOCs), metal oxides, *etc.* Some of them, like MCs, were studied soon after TMDs and others like TMCPs were re-discovered very recently. In this section, we review the photodetections of these 2D members organized by material categories. And in each category, the basic properties of the corresponding materials, including crystalline structure, band structures, and absorption, are first discussed followed by photodetection applications.

#### 3.1 Elementals

Elemental 2D layered materials, including group IVA materials (silicene, germanene, stanene), group VA ones (black phosphorus, arsenene, antimonene, bismuthene), and tellerene in group VIA, are the most similar analogues of graphene. Unlike the planar hexagonal structure of graphene, these elemental 2D layered materials share a buckled structure composed of puckered atomic sheets (see the structure of BP in Fig. 2a as an example) with the so-called “chair, boat, and washboard” like crystalline structures.<sup>67</sup> According to theoretical and experimental results, the electric band gaps of these materials cover a very wide range of from 0 eV for semimetal to  $\sim 2.5$  eV. In addition, their simple composition makes synthesis of high-quality 2D elementals feasible which is very important for controllable scaling up. The two advantages mentioned above, but not limited, make this family of 2D layered materials stand out. However, due to the difficulty of synthesis and bad stability in ambient conditions, only a few kinds of these materials (BP and Te) based photodetectors have been fabricated and studied.

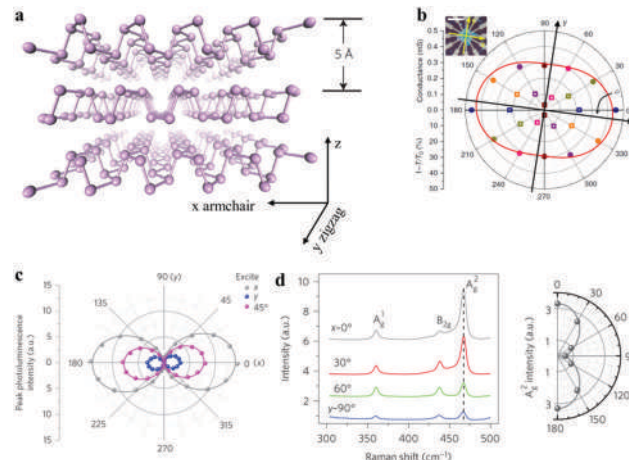


**Fig. 2** (a) Atomic structure of black phosphorus. (b) The angle-resolved DC conductance (solid dots) and the polarization-resolved IR relative extinction (at  $2700 \text{ cm}^{-1}$ , hollow squares) of a BP flake shown in the inset. Scale bar: 50 nm. (c) Polarization resolved Raman scattering spectra of monolayer black phosphorus with linearly polarized laser excitation. Right panel shows the intensity of the  $A_2^{\text{g}}$  mode as a function of the excitation laser polarization angle in the  $x$ - $y$  plane. (d) Photoluminescence peak intensity as a function of polarization detection angle for excitation laser polarized different directions. (a) is reproduced from ref. 68 with permission from Macmillan Publishers Ltd, Copyright 2014. (b) is reproduced from ref. 69 with permission from Macmillan Publishers Ltd, Copyright 2014. (c) and (d) are reproduced from ref. 70 with permission from Macmillan Publishers Ltd, Copyright 2015.

Hence, in this subsection, we will introduce the basic properties of 2D elementals with the main focus on BP and Te.

**3.1.1 Black phosphorus.** Since its rediscovery in 2014, black phosphorus (BP) has become the favourite among the big family of 2D layered materials because of its wide thickness-tunable direct bandgaps ( $\sim 0.3$  to 2 eV), strong intralayer anisotropy, and potentials in FETs with high mobility.<sup>68,69,71–73</sup> Bulk BP has an orthorhombic structure with a  $D_{2h}^{18}$  space group symmetry (see Fig. 2a).<sup>68</sup> In the atomic layer, each phosphorous atom connects to three neighboring atoms, leading to two special directions: armchair and zigzag directions along the  $x$  and  $y$  axis, respectively. This highly anisotropic arrangement of phosphorous atoms leads to anisotropic electric band dispersion, further bringing the anisotropic electronic and optical properties, hence optoelectronic properties. Electrodes with circular symmetry (the inset in Fig. 2b for example) have been widely used to study anisotropy in electrics of 2D layered materials.<sup>69</sup> Utilizing this simple method, Xia *et al.* found BP with the best/worst conductivity along armchair ( $x$ )/zigzag ( $y$ ) directions (solid dots in Fig. 2b), which agrees well with what was found by Liu *et al.*<sup>34</sup> And the directional conductivity  $\sigma_{\theta}$  can be quantitatively defined as  $\sigma_{\theta} = \sigma_x \cos^2(\theta - \phi) + \sigma_y \sin^2(\theta - \phi)$ , where  $\theta$  and  $\phi$  are the angle differences between the electric field and reference direction and that between reference direction and  $x$  axis;  $\sigma_x$  and  $\sigma_y$  are the conductivities along  $x$  and  $y$  axis, respectively. At the same time, an anisotropic IR absorption has been also found (hollow squares in Fig. 2b).<sup>70</sup> On the other hand, the light emission of BP is also anisotropic. Using photoluminescence



microscopy with isolated polarized excitation and detection sources, Wang *et al.* found the anisotropic PL spectra of monolayer BP (Fig. 2c). The highest PL intensity occurs when both excitation and detection are along the armchair ( $x$ ) direction. They ascribed this anisotropy to two aspects: the anisotropic light absorption with  $x$  as the strongest absorption direction, and the anisotropic exciton which is due to the anisotropic mobile ability of charge carriers (also highest along the  $x$  axis). Considering the strong anisotropy of BP mentioned above, it is necessary to identify the orientation of BP flakes before fabricating devices like photodetectors. To do this, polarized Raman microscopy is a feasible tool through which the obvious direction-dependent Raman intensity has been widely observed. Fig. 2d shows Wang and his colleagues' work as an example.<sup>70</sup> Among the three main Raman peaks,  $A_g^2$  mode shows the strongest anisotropy with the maximum intensity along the armchair ( $x$ ) direction. It is based on this method that orientation-controlled photodetectors could be fabricated and studied (as discussed in following part).

The second feature of BP is its wide thickness-dependent bandgaps which come from the relatively strong interlayer interaction of buckled BP atomic sheets. Fig. 3a summarizes its thickness-dependent bandgaps from both first-principle

calculation and experimental results.<sup>34,74–77</sup> For the former method, there is variability in the calculated values because of the different approximation methods and parameters used. A commonly used value is based the GW method which gives  $\sim 0.3$  and 2 eV for bulk and monolayer, corresponding to light with wavelength of  $\sim 4 \mu\text{m}$  and 600 nm wavelength, respectively. No matter what methods are used, the bandgap of BP exhibits a huge blue shift while decreasing the number of layers. More importantly, BP always keeps its direct-bandgap nature while changing its thickness. Fig. 3b shows Castellanos-Gomez *et al.*'s work as an example, where band edges of conduction and valence bands always locate at the  $\Gamma$  point.<sup>75</sup> It is because of the above two advantages that makes BP one of the most promising candidates for detecting wide range spectra (from UV to middle and far IR).

Besides thickness, the bandgap of BP can also be modulated by other strategies, including applying strain,<sup>79–83</sup> electric field,<sup>80,84–86</sup> and composition alloying.<sup>78</sup> Liu *et al.* used arsenic, an element in the same group with P, as the alloying component to synthesize black arsenic–phosphorous (b-As $_x$ P $_{1-x}$ ).<sup>78</sup> Multilayer b-As $_x$ P $_{1-x}$  with various compositions were obtained by exfoliating the corresponding bulks synthesized through a chemical vapor transport reaction method. The authors found that the as-obtained b-As $_x$ P $_{1-x}$  have a similar crystalline structure

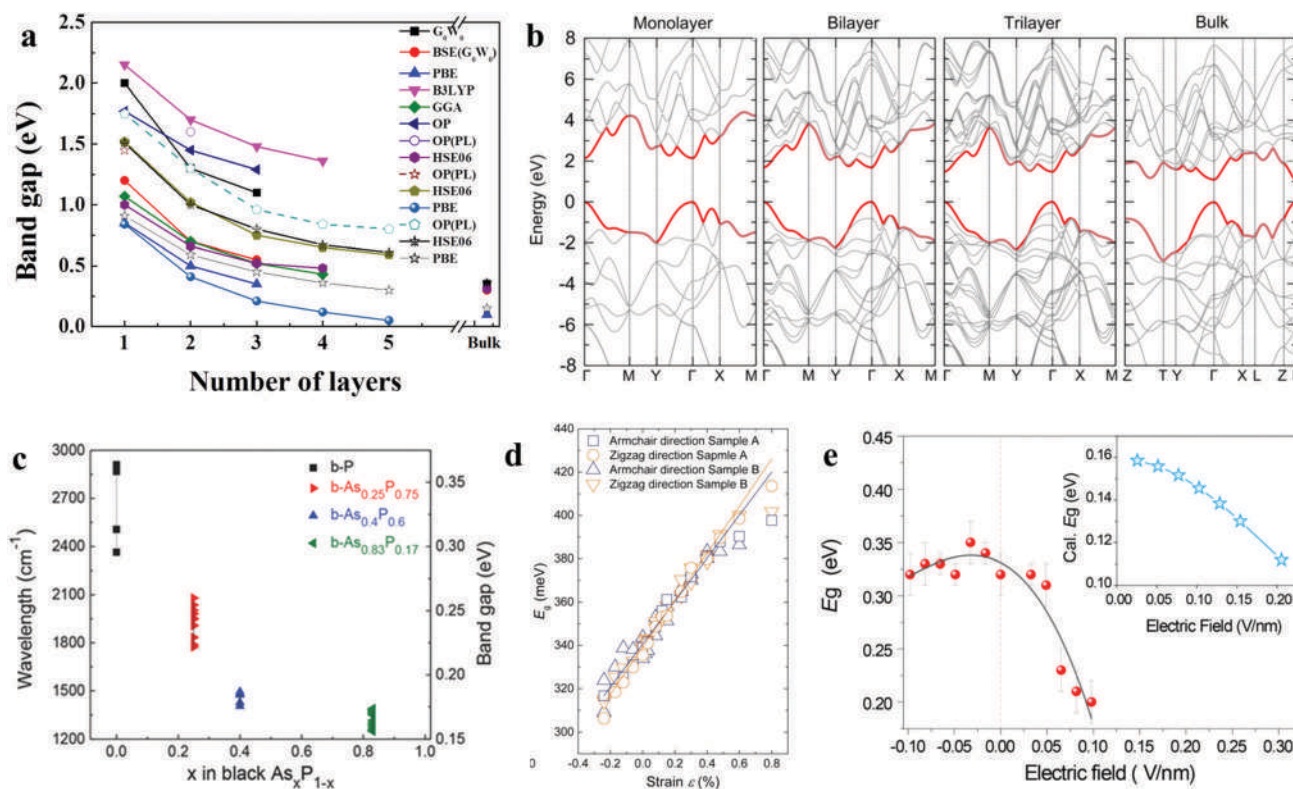


Fig. 3 (a) Bandgaps of BP as a function of thickness extracted from literatures. The calculation methods and optical bandgaps (OP) are denoted. (b) Calculated electronic band structures of BP with different numbers of thickness. (c) Bandgaps of b-As $_x$ P $_{1-x}$  with various compositions. (d) Bandgaps plotted as a function of strain. (e) Measured bandgaps of 11-layer BP as a function of electrical field with the inset showing calculated values in the presence of electrical fields. (a) Data are extracted from ref. 34 and 74–77; (b) is reproduced from ref. 75 with permission from IOP Publishing Ltd, Copyright 2014; (c) is reproduced from ref. 78 with permission from John Wiley & Sons, Inc., Copyright 2015; (d) is reproduced from ref. 79, and (e) is reproduced from ref. 80 with permission from American Chemical Society, Copyright 2017.



with pure BP and, more importantly, a wide-range bandgap of 0.3–0.15 eV (Fig. 3c). On the other hand, calculations have shown that the deformation in the structure along the armchair direction can affect the bandgap of monolayer BP dramatically due to a special energy dispersion.<sup>81</sup> And, considering the superior mechanical flexibility of an ultrathin 2D configuration, applying moderate strain has been a special means to modulate bandgaps of 2D layered materials. With this in mind, Zhang *et al.* fabricated flexible BP FETs on PET substrates and found a continuous modulation of the multilayer BP bandgap from ~0.31 eV to ~0.42 eV (Fig. 3d).<sup>79</sup> Another interesting method to tune the bandgap of semiconductors is the so-called Stark effect, *i.e.*, the shifting/splitting of atomic/molecular energy levels due to the presence of an external electric field. This effect is usually negligible in conventional materials; however, it becomes noticeable for 2D layered materials due to a significantly reduced electric screening. For instance, Liu *et al.* found a monotonic narrowing of the bandgap of multilayer BP from ~0.31 eV to 0.2 eV.<sup>80</sup> From the above analysis, we can see that the bandgap of BP (and its compounds) itself covers an extremely wide range of ~0.15–2 eV, corresponding to ~8–0.6  $\mu\text{m}$ , which definitely has not been achieved in any other 2D layered materials.

Owing to the features mentioned above, photodetectors based on BP were studied immediately after its rebirth. Buscema *et al.* fabricated phototransistors based on few-layer BP (3–8 nm) and demonstrated a wide-range photoresponse from visible (475 nm) to near infrared (940 nm) region with a highest  $R$  of 0.7 and 4.8  $\text{mA W}^{-1}$ , respectively.<sup>71</sup> At the same time, a fast response with  $\tau_r$  and  $\tau_d$  of 1 ms and 4 ms were demonstrated, respectively. A wider-range (532–1220 nm) photoresponse and higher  $R$  (5 and 20  $\text{mA W}^{-1}$ , respectively) were found by Engel and his colleagues.<sup>72</sup> Notably, they utilized the as-fabricated BP photodetector for point-by-point imaging in both the visible and near-infrared spectral regimes and demonstrated the diffraction-limited imaging capability. To further enhance photoresponse performance, Huang *et al.* adopted nickel as an electrode metal to fabricate few-layer BP photodetectors, in which  $R$  as high as  $6.7 \times 10^5 \text{ A W}^{-1}$  and  $10^3 \text{ A W}^{-1}$  for 633 nm and 900 nm lights could be achieved.<sup>87</sup> The large variation in responsivity is probably due to: different contact qualities through using different electrode metals (Ni or Ti), hence a different extraction capability of photo-generated charge carriers; different thickness of BP; and different trap densities at the flake/substrate interface, which may induce totally different photoresponse mechanisms (the photogating or PV effect as has been discussed in the Fundamentals section).

By maximizing the photo-absorption and photo-stimulated charge carriers, extraction capability through designing photodetectors along the armchair direction (both for electrodes and polarization of incidence light), high  $R$  of  $\sim 10^3 \text{ A W}^{-1}$  and gain of  $\sim 10^4$  at 532 nm light were also demonstrated by Guo *et al.*<sup>18</sup> More importantly,  $R$  as high as 82  $\text{A W}^{-1}$  and NEP as low as  $10^{-12} \text{ W Hz}^{-1/2}$  can be achieved for 3.39  $\mu\text{m}$  light at room temperature (Fig. 4a–c), which is already at the level of

commercialization. In addition, the authors found that the relationship between  $I_{\text{ph}}(R)$  and  $P_{\text{in}}$  (incident light power) can be described by the Hombeck–Haynes model:

$$I_{\text{ph}} = q\gamma(\tau_{\text{photocarriers}}/\tau_{\text{transit}})[F/(1 + F/F_0)],$$

where  $\gamma$  and  $F$  are the absorption of BP and photon absorption rate in units of  $\text{s}^{-1}$ , respectively, and  $F_0$  is the photon absorption rate when trap saturation occurs. In this model, the photo-generated charge carriers first fill the many trap states, giving rise to a remarkable PGE (photogating effect), then it changes to the conventional PCE (photoconductive effect) after the traps are fully filled at higher illumination density, inducing a decreased  $I_{\text{ph}}(R)$  due to the increased probability of electron–hole recombination. In total, this model displays a feature of a platform followed with monotonous decrease in the  $I_{\text{ph}}(R)$ – $P_{\text{in}}$  curves (Fig. 4b). This transition can be also observed from the  $P_{\text{in}}$  dependent  $I_{\text{ph}}$ – $V_{\text{GS}}$  curves (Fig. 4c). At low illumination, the  $I_{\text{ph}}$ – $V_{\text{GS}}$  follows exactly the same trend with conductance– $V_{\text{GS}}$  (a feature of PGE that has been discussed in the Fundamentals section), and gradually deviates from it while at higher  $P_{\text{in}}$ .

Various mechanisms have been claimed for BP photodetectors in the wavelength range of visible to IR (~500 nm to 3.39  $\mu\text{m}$ ), including PCE,<sup>87</sup> PGE,<sup>18</sup> PTE, and BE.<sup>73</sup> Actually, for photodetectors based on low-dimensional materials like BP, the photoresponse usually comes from a combination of different mechanisms and may switch from one type domination to another while changing the measurement parameters (the power density for example). Hence, it will be more accurate to provide details, such as temperature, flake thickness, charge carrier density, incident light wavelength, power density, and voltage bias, while speaking of the photoresponse mechanism. For BP, it has been found that  $P_{\text{in}}$  plays a considerable role. For  $P_{\text{in}}$  at the level of  $10^{-3}$  – a few  $\text{W cm}^{-2}$  (varies for different cases), PGE may play a dominant role. And PCE gradually stand out for  $\sim$  a few-100  $\text{W cm}^{-2}$ . Finally, PTE and BE may predominate for  $P_{\text{in}}$  of 1000  $\text{W cm}^{-2}$  or higher. Meanwhile, voltage bias may also affect the result. For instance, Yuan *et al.* found that the PTE and PCE will mainly contribute to photocurrents for low (0–0.15 V) and high  $V_{\text{DS}}$  (>0.15 V) ranges, respectively.<sup>70</sup> To elucidate the proportion of each mechanism, measurements/analysis of relationships between  $I_{\text{op}}$  and  $P_{\text{in}}$ ,  $V_{\text{GS}}$ , channel length, and position are usually needed.

The response range of BP can be further expanded, even down to the UV region. Wu *et al.* found the  $R$  of photodetectors based on few-layer BP (~4.5 nm) could achieve as high as 175  $\text{A W}^{-1}$  at 390–310 nm light, which is almost 3 orders higher than that of visible light (~90  $\text{mA}$  for 800 nm) at the same condition.<sup>88</sup> By applying  $V_{\text{GS}}$  (–80 V), this value could reach  $\sim 9 \times 10^4 \text{ A W}^{-1}$ . With the help of theoretical calculations, they found this high UV photoresponse of BP is due to the so-called band nesting effect, *i.e.*, the existence of points in a band with  $\nabla_{\mathbf{k}} = (E_{\text{C}} - E_{\text{V}}) = 0$ , where  $E_{\text{C}}$  and  $E_{\text{V}}$  are the conduction and valence bands respectively.

Besides high response to wide-spectra light, BP-based photodetectors have another feature – polarization-sensitivity – which originates from the in-plane crystalline anisotropy induced

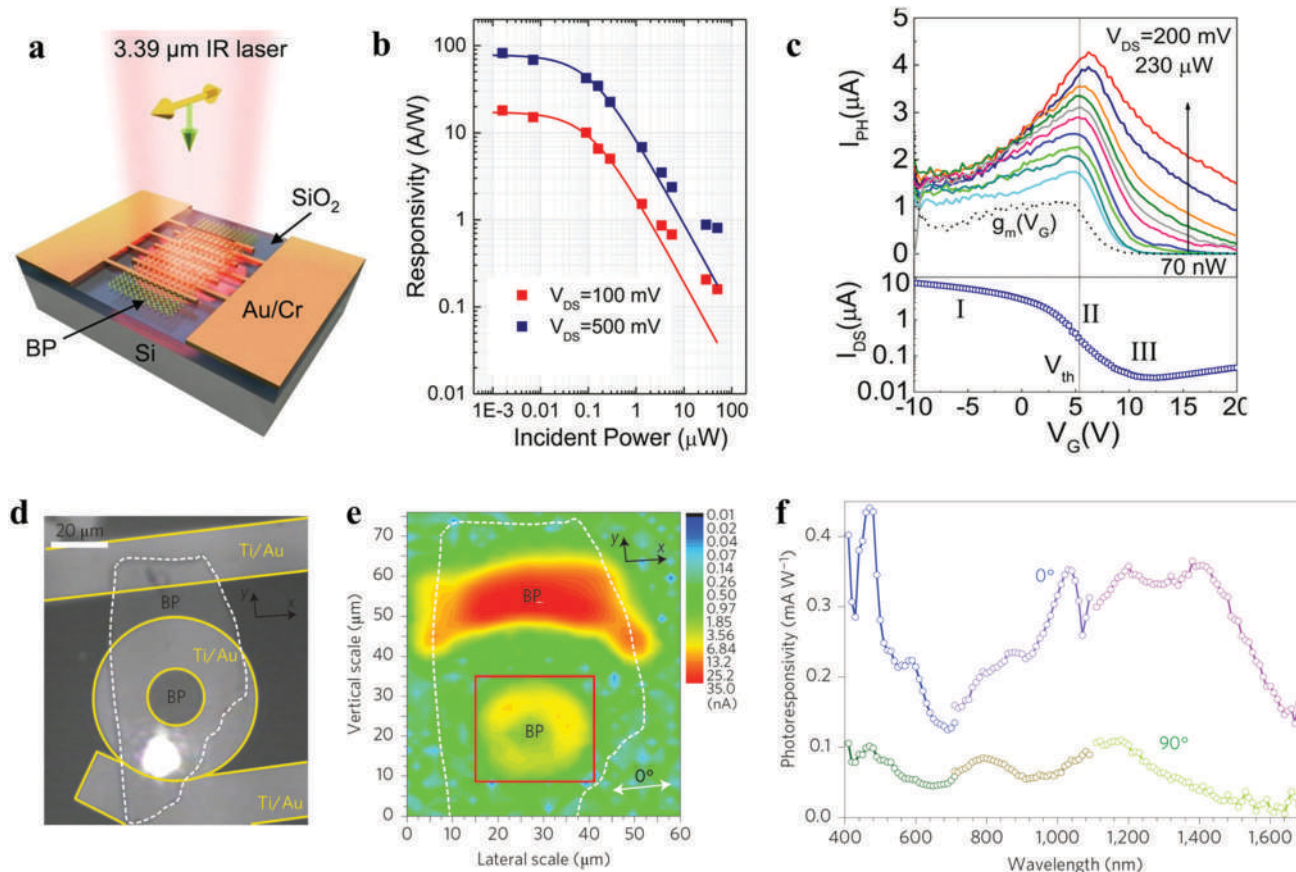


Fig. 4 (a) Schematic of the BP photodetector operating at 3.39  $\mu\text{m}$ . (b) Power dependence of the responsivity. Solid lines: fitting results with Hornbeck-Haynes model. (c) Upper panel: Photocurrents as a function of gate voltage under various incident optical powers. The dashed line sketches the gate-dependent channel trans-conductance. Lower panel: Transistor transfer characteristic for reference. (d) Optical image of the BP photodetector with a ring-shaped photocurrent collector. The corresponding photocurrent microscopy image is shown in (e). (f) Polarization dependence of responsivity; (a–c) are reproduced from ref. 87 with permission from American Chemical Society, Copyright 2016; (d–f) are reproduced from ref. 19 with permission from Macmillan Publishers Ltd, Copyright 2015.

linear dichroism (as discussed in Fig. 2). To verify the role of anisotropic absorption on the polarized photoresponse, devices with ring-shape electrodes which can eliminate the possible effects of asymmetric contacts (as shown in Fig. 4d and e) are essential. Utilizing this device configuration combined with a series of optical studies, Yuan and his colleagues demonstrated BP-based photodetectors with polarization-sensitive photoresponse capability to a wide-spectra range of  $\sim 400$  nm to  $3.75$   $\mu\text{m}$  (Fig. 4f).<sup>70</sup>

BP can be also utilized for THz detection. Miriam S. Vitiello's research group has done a series of works on this research field.<sup>52–54</sup> They found that both plasma-wave rectification, thermoelectric, and bolometric effects can dominate the mechanism of BP-based THz detectors. And the contributions of them can be modulated by using different device configurations, tuning the incident radiation frequency, and applying  $V_{\text{GS}}$ , *etc.* For example, under radiation with a resonant frequency of  $\sim 0.29$  THz (Fig. 5d shows the optical image of the BP FET device); a plasma-wave rectification effect dominates the photovoltage verified by the coincidence between experimental and calculation results (as shown in Fig. 5a and b, respectively).

However, it turns to a thermoelectric effect while detuning the radiation frequency to  $\sim 0.32$  THz (Fig. 5c). Through these strategies,  $R$  as high as  $\sim 5\text{--}8$   $\text{V W}^{-1}$  can be achieved for radiation with frequency of around 0.3 THz. Based on this, BP-based THz detectors have been exploited for practical imaging as illustrated in Fig. 5e.<sup>54</sup>

Although BP has shown promising photodetection properties, poor stability has become one of the greatest concerns and limit its further development.<sup>89–95</sup> It has been shown that BP flakes will quickly degrade after exfoliation and lose their electrical properties after a few hours/days at atmosphere conditions.<sup>89,96,97</sup> This situation gets more serious for thinner flakes, which heavily restricted their exploration. The underlying mechanism has not been totally understood yet. But it seems that the exposure to  $\text{O}_2$  and moisture, as well as light, may play a key role.<sup>93,98</sup> Up to now, only a few strategies have been developed to enhance the stability of BP, including passivation with protecting layers like  $\text{Al}_2\text{O}_3$ ,<sup>89,97,99</sup>  $\text{TiO}_2$ ,<sup>100</sup> hBN,<sup>53</sup> graphene,<sup>101</sup> and even  $\text{MoS}_2$ ,<sup>102</sup> surface modifications with molecular through chemical and/or physical interactions,<sup>90,96,103</sup> and doping with specific elements.<sup>91</sup> Table 1 summarizes the

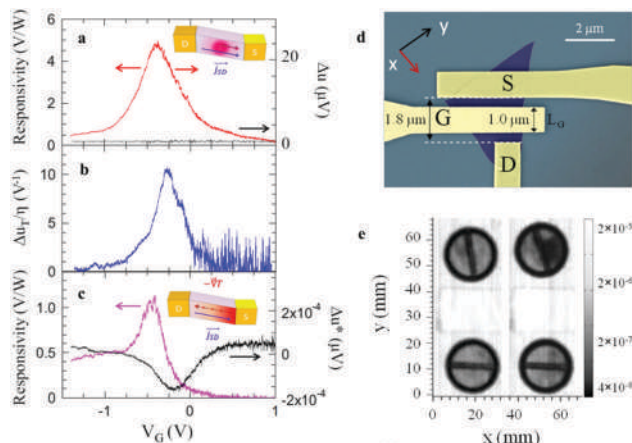


**Fig. 5** Gate-bias dependent (a) experimental  $R$  and (b) predicted photo-voltage using overdamped plasma-wave regime. Inset: Schematics of the overdamped plasma-wave dynamics. Here 0.29 THz radiation is used. (c) Gate bias dependences of the experimental  $R$  (left axis) and measured photovoltage (right axis). Inset: Schematics of the thermoelectric dynamics. Here 0.32 THz radiation is used. (d) False-colored scanning electron microscope image of the BP FET. (e) Transmission THz imaging (obtained at 0.29 THz radiation) of a box of two tablets before (left) and after (right) injecting 3  $\mu\text{L}$  water. Figures (a–e) are reproduced from ref. 54.

reported strategies, stability after treatments, and the methods used to evaluate performances. As we can see, the stability of BP can be much enhanced after the treatments. However, for most of these proposed strategies, one issue needs to be considered: the inevitable modifications on the electrical properties of BP after the treatments. Taking this into consideration, encapsulation with

stable 2DLMs like hBN and/or graphene may be one of the most promising ways, plus it won't considerably increase the thickness of the hybrid structures.

**3.1.2 Te.** Very recently, another elemental 2D layered material – Te – has received growing attention. Unlike its analogues, at normal conditions bulk Te is a so-called one-dimensional van der Waals material in which covalently bonded Te atom chains, not planes, are connected by weak van der Waals forces ( $\alpha$  phases as shown in Fig. 6a).<sup>108</sup> Inside a chain, each Te atom is bonded with its neighboring two forming a repeating unit consisting of three atoms. Interestingly, three more phases will appear while decreasing the dimensionality down to 2D:  $\beta$ ,  $\gamma$  (2H MoS<sub>2</sub>-like), and 1T phases, which can be seen as reconstructions based on the  $\alpha$  phase (note that different names may be used in different literatures).<sup>108,109</sup> This multi-phase character originates from the multivalent feature of Te element. For example, in the 2H and 1T like MoS<sub>2</sub> structures, the central-layer Te behaves more metal-like and the two outer layers more semiconductor-like. And the thermodynamically stable phase may switch among them while varying body thickness. For example, according to Qiao *et al.*'s work,  $\alpha$  phase is always the most stable when the number of layers is larger than 1; however, the 1T phase becomes more stable for monolayer tellerene.<sup>108</sup> In addition, the energy differences between these phases are rather small (only a few meV) for a few-layer sample, meaning that they could change from one phase to another easily. Consequently, external field tunable electronic and optoelectronic properties are predictable. Like its analogues, Te also exhibits thickness tunable bandgaps. For instance,  $\alpha$ -phase Te experiences a wide  $E_g$  tunability of from  $\sim 0.3$  eV

**Table 1** Comparison of different strategies to stabilize BP

Methods	Stability duration	Tools	Ref.
Few-layer MoS <sub>2</sub> as a vdW passivation layer	① exposing to the ambient environment for 3 weeks; ② annealing at 350 °C for 2 h.	Raman spectroscopy	102
[BMIM][BF <sub>4</sub> ] ionic liquid treated, which can sequester reactive oxygen species	Remain stable for over 13 weeks	Electrical characteristics	104
Aryl diazonium modification, which can form covalent phosphorus-carbon bonds.	① improved on/off current ratio; ② three weeks of ambient exposure.	AFM; electrical characteristics	96
Atomic layer deposited AlO <sub>x</sub> overlayers	Over 2 weeks in ambient conditions.	AFM; electrical characteristics	89
Forming h-BN/BP/h-BN heterostructure	Reaching record mobility, 1350 cm <sup>2</sup> V <sup>-1</sup> s <sup>-1</sup> at room temperature	Electrical characteristics	53
Graphene as an encapsulation layer	60 days under ambient conditions	Photoresponse characteristics	101
Solvation (CHP) shell protecting the nanosheets from reacting with water/O <sub>2</sub>	Stable for $\sim 200$ h in ambient conditions	Absorbance, AFM, Raman and TEM	90
Solvation (DPPC) shell passivated Al <sub>2</sub> O <sub>3</sub> encapsulation	Kept in air for more than two weeks.	AFM, electrical characteristics	105
Metal ion (Ag <sup>+</sup> ) modification	At least eight months.	Electrical characteristics	99
Electrochemical molecular intercalation approach	Enhanced ON/OFF ratio; exposed to air for 5 days	AFM, electrical characteristics	106
	300 h exposure in ambient conditions, high on/off current ratio exceeding 10 <sup>7</sup> , high mobility of 328 cm <sup>2</sup> V <sup>-1</sup> s <sup>-1</sup>	Electrical characteristics	107
Plasma treatment and PMMA passivation	15 days exposure; high on/off current ratio of 10 <sup>5</sup> , high mobility of 1150 cm <sup>2</sup> V <sup>-1</sup> s <sup>-1</sup>	AFM, Raman, electrical characteristics	92
Oxygen plasma etching followed by passivation with an Al <sub>2</sub> O <sub>3</sub> coating	30 days in ambient condition	PL, OM	97
Depositing a passivating organic monolayer (CA, M)	Under ambient conditions over a month.	AFM, XPS	103
Doping with tellurium (Te)	Three weeks exposure to air and moisture at ambient conditions	AFM, nuclear magnetic resonance (NMR), electrical characteristics	91
Titanium suboxide (TiO <sub>x</sub> ) as an encapsulation layer	Exposure in air for 5 days, n-type doping	AFM, electrical characteristics	100



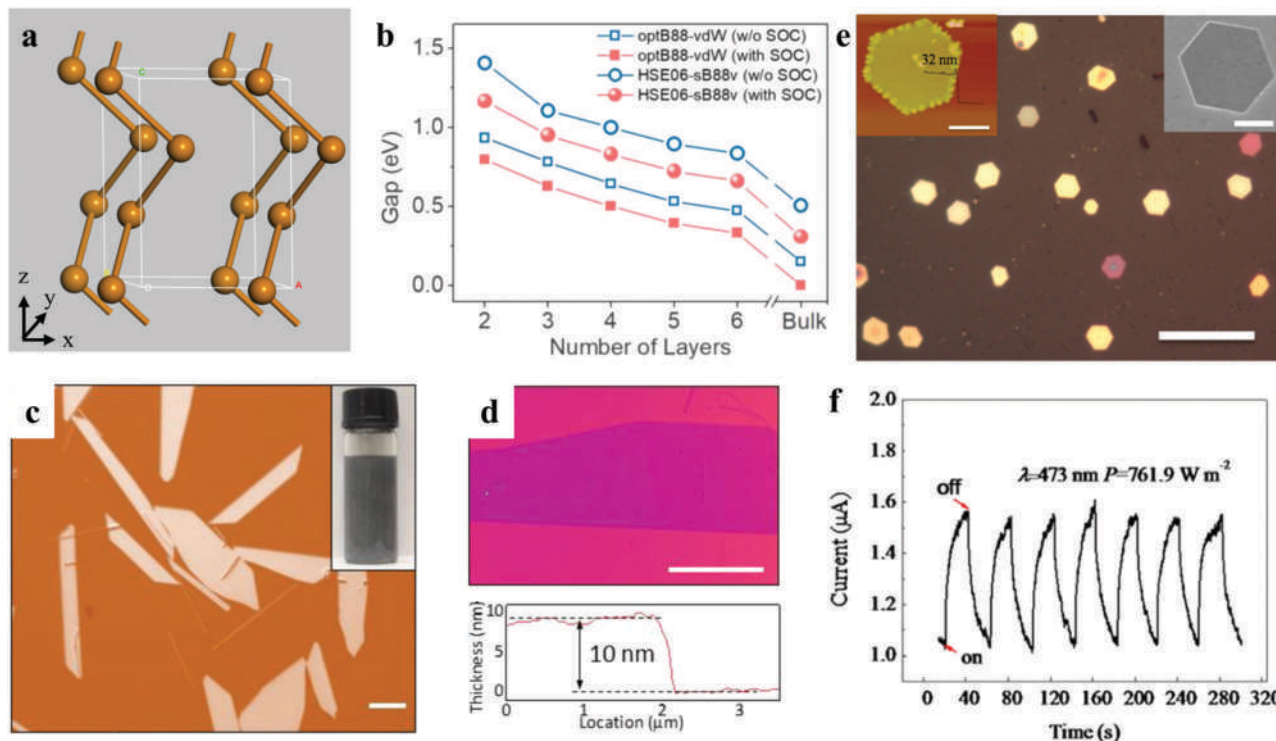


**Fig. 6** (a) Schematic of a bulk Te unit cell. (b) Evolution of the bandgaps as a function of the body thickness. (c) Optical image of solution-grown Te flakes. Inset: Optical image of the Te solution dispersion. The scale bar is 20  $\mu\text{m}$ . (d) AFM image of a 10 nm Te flake. The scale bar is 30  $\mu\text{m}$ . (e) Typical optical image of 2D Te hexagonal nanoplates with scale bar of 30  $\mu\text{m}$ . Left inset: AFM image of a Te hexagonal nanoplate with thickness of 32 nm. The scale bar is 2  $\mu\text{m}$ . Right inset: SEM image of a single 2D Te hexagonal nanoplate. The scale bar is 4  $\mu\text{m}$ . (f) Time-dependent photoresponse of Te hexagonal nanoplate device with  $V_{\text{DS}}$  of 2 V. (b) Reproduced from ref. 108 with permission from Elsevier B.V. and Science China Press, Copyright 2018; (c) and (d) are reproduced from ref. 111 with permission from Macmillan Publishers Ltd, Copyright 2018; (e) and (f) are reproduced from ref. 281 with permission from American Chemical Society, Copyright 2014.

for bulk to  $\sim 1.2$  eV for 2L (Fig. 6b), while monolayer tellerene with 1T phase becomes a metal, which is almost comparable with BP.<sup>108</sup> In addition, bulk  $\alpha$ -phase has a nearly direct bandgap with the conduction and valence band edges located around the H point in the Brillouin zone. While thinning down to 2L, Te becomes an indirect bandgap semiconductor with the conduction band edge changing to locate at the Z point and the valence band edge at a point on the S–G line. Note that spin orbit coupling plays an important role on defining the band structures of Te. Strain has also been demonstrated to show the capability of modulating  $E_g$  of Te. For example, Zhu *et al.* predicted that a  $-10\%$  strain along the zigzag or biaxial direction will modulate the  $E_g$  of tellerene down to zero.<sup>110</sup> All the results mentioned above predict Te with similar features as BP, but with larger numbers of freedom like phase transition and higher potential in optoelectronic applications like photodetectors.

Up to now,  $\alpha$ -phase Te as thin as 1L has been successfully synthesized by a MBE and solution method. Zhu *et al.* and Chen *et al.* independently demonstrated the synthesis of  $\alpha$ -phase Te films on HOPG *via* MBE and studied the corresponding electronic properties.<sup>109,113</sup> These two works have shown that the as-grown 1L Te have a thickness of  $\sim 0.4$  nm, well matched with the theoretical prediction. Wang *et al.* reported a high-production solution method, in which  $\text{Na}_2\text{TeO}_3$ ,

$\text{N}_2\text{H}_4$ , and PVP are used as Te source, reductant, and surface passivation agent, respectively.<sup>111</sup> Through this method,  $\alpha$ -phase Te flakes with thicknesses from 10 to 100 nm and lateral dimension from 50 to 100  $\mu\text{m}$  have been obtained (see Fig. 6c and d), based on which the Raman and magneto-transport properties were studied.<sup>114</sup> The as-grown Te shows three main Raman peaks located at  $\sim 94$ , 122, and 142  $\text{cm}^{-1}$ , corresponding to the  $E_1$  ( $x$ -axis rotation),  $E_2$  (mainly  $z$ -axis asymmetric stretching), and  $A^1$  (chain expansion) modes, respectively. Due to its strong anisotropic crystalline structure, Te shows obvious anisotropic Raman-strain response and magneto-resistance behaviors, providing a feasible method to define sample alignments. Unfortunately, according to the best of our knowledge, no study about the photodetection property of these 2D layered Te has been reported, which is probably because of the short history (only about half a year before this manuscript was prepared). However, the related research must be just around the corner considering the handy synthesis method and the high potentials theoretically predicted.

One thing should be noted is that, even though the photoresponse of 2D layered Te has not been studied, the ‘non-layered’ 2D Te have been. Here, the so-called layered or non-layered Te is determined by the viewing direction on the crystalline structure: ‘non-layered’ for cross section along the  $x$ - $y$  plane, and ‘layered’ along the  $z$  direction (Fig. 6a).



Even though having the ‘non-layered’ crystalline structure, nanostructures with 2D morphology can be synthesized. Using a van der Waals epitaxy method, Wang *et al.* grew hexagonal non-layered Te nanoplates with a thickness of 30–80 nm and lateral dimension of 6–10  $\mu\text{m}$  on flexible mica substrate (Fig. 6e). The *in situ* fabricated photodetectors show  $R$  of  $\sim 162\text{--}390 \text{ A W}^{-1}$  to 473 nm light and good bending stability (Fig. 6f).<sup>112</sup>

**3.1.3 Others.** Besides BP and Te, elemental 2D layered materials also include silicone, germanene,<sup>115,116</sup> and stanene<sup>117</sup> in group IVA, and arsenene,<sup>118</sup> antimonene,<sup>119,120</sup> and bismuthene<sup>121–123</sup> in group VA,<sup>124,125</sup> *etc.* However, photodetection properties of practical devices based on these materials have not been reported due to a few issues. The first is bad stability. For group IVA materials, their monolayers are artificially predicted without knowing their natural 3D parents, making them unable to survive in ambient conditions by themselves. Although there have been some strategies to enhance their stability, such as interaction with substrates<sup>126,127</sup> and encapsulation,<sup>128</sup> based on which practical FET devices have been fabricated, there is still a long way to go for studying photodetection properties with real cases. On the other hand, the issue of stability is not that serious for the group VA materials family.<sup>119,120,123</sup> However, these materials show metallic properties in bulk and become semiconductors only while thinning down to 2L (for As and Bi) or 1L (for Sb), which largely limits their photodetection study.<sup>129,130</sup>

Nevertheless, there is still something worth expecting based on the following considerations. Group IVA materials, especially silicone and germanene, show high compatibility with existing technologies due to a long history of commercialized devices based on their 3D parents.<sup>131</sup> For group VA, especially Bi and Sb, air-stable monolayers have been synthesized by MBE and/or van der Waals epitaxy.<sup>119,120,123</sup> In addition, monolayers of both of these two material families have shown appealing properties.<sup>132</sup> For example, silicone, germanene, stanene and bismuthene have shown strong substrate-tunable properties, and bismuthene on a SiC substrate has been demonstrated to have a quantum spin Hall wide-gap state.<sup>121,122</sup>

## 3.2 Main group metal chalcogenides

Main group metal chalcogenides (MMCs) in the forms of MX, MX<sub>2</sub>, and M<sub>2</sub>X<sub>3</sub>, where M = Ga, In, Ge, and Sn, and X = S, Se, and Te, are the analogues of well-studied TMDs. Unlike TMDs which are mainly studied as candidates for FETs, MMCs have attracted great attention due to their novel optoelectronic properties. In this subsection, we will discuss the photodetection properties of this material family organized by the types of main metals.

**3.2.1 Ga-Based MMCs.** GaS, GaSe, and GaTe compose the Ga-based 2D layered MMCs. Compared with TMDs like MoS<sub>2</sub>, they have more complex layered structures and totally different thickness dependence of  $E_g$ . For GaS/Se, first principle calculation predicts that their electric bandgaps change from 1.59/2.34 to 2.50/3.89 eV keeping their indirect nature while tuning the thickness from bulk to monolayer.<sup>133,134</sup> For bulk GaS, the

conduction band minimum (CBM) and valence band maximum (VBM) locate at  $\Gamma$  and  $M$  points, respectively. Interestingly, for GaS with thickness less than 4L, the VBM changes to be a saddle-like shape around the  $\Gamma$  point. This double peaks feature improves the density of charge carriers involved in the photo-adsorption process, enhancing their photodetection performance.<sup>133</sup> A similar phenomenon was also found in few-layer GaSe.<sup>134</sup> On the other hand, monoclinic GaTe has a direct bandgap for all the thicknesses ( $\sim 1.7$  eV for bulk), making it more appealing for photodetection.<sup>33,135</sup> In addition, for hexagonal GaTe, even though the indirect bandgap nature for all the thickness range, the VBM shifts quickly towards the  $\Gamma$  point as the thickness goes beyond 1L. This allows for a considerable photo-absorption at the local band position, indicating reasonable photodetection performance for multilayer hexagonal GaTe.

Research on the photoresponse properties of Ga-based MMCs began soon after that of TMDs. In a pioneering work, Hu *et al.* found few-layer GaS flakes had a wide-spectra response with  $R$  gradually increasing from  $\sim 10^{-4} \text{ A W}^{-1}$  to  $4.24 \text{ A W}^{-1}$  to 610–254 nm light.<sup>133</sup> In addition, bendable photodetectors were demonstrated by fabricating devices on PET substrate. Yang *et al.* studied the influence of gas environments on the photoresponse performances of mechanically exfoliated few-layer GaS.<sup>137</sup> Higher  $R$  were observed in NH<sub>3</sub> environment (as high as  $\sim 64 \text{ A W}^{-1}$ ) compared with that in air or O<sub>2</sub> environments. Very recently, Carey *et al.* reported a two-step method to achieve controllable large-scale synthesis of bilayer ( $\sim 1.5$  nm) GaS films, with a schematic of the synthesis process shown in Fig. 7a.<sup>136</sup> Utilizing Ga with a low melting point and the naturally existing thin oxide layer (GaO) on the liquid–air interface, they could print this thin GaO layer onto the substrates with high adhesion. After removing the extra Ga liquid and sulfurizing the GaO layer, bilayer GaS films can be then obtained. Based on this scalable method, the authors fabricated arrays of photodetectors with  $R$  of  $\sim 6 \text{ A W}^{-1}$  to solar simulator as shown in Fig. 7b and c.

Hu *et al.* also studied the photoresponse properties of few-layer GaSe.<sup>138</sup> Similar with GaS, wide-spectra response to 620–254 nm, with a highest  $R$  of  $2.8 \text{ A W}^{-1}$  to 254 nm light, was demonstrated. Lei *et al.* studied the photodetection of CVD-grown GaSe (4–6 layers in thickness), and found a peak response to 380 nm light with  $R$  of  $17 \text{ mA W}^{-1}$ . Zhou *et al.* synthesized GaSe nanoplates on mica by van der Waals epitaxy and *in situ* fabricated bendable photodetectors with  $R$  of  $30 \text{ mA W}^{-1}$  to halogen light.<sup>139</sup> Based on a thicker mechanically exfoliated GaSe flake ( $\sim 12$  nm), Huang *et al.* improved the  $R$  to  $2.2 \text{ A W}^{-1}$  under the illumination of 510 nm light.<sup>140</sup> Through localized illumination, Cao *et al.* found that the as-fabricated GaSe devices with Ti contact are actually photodiodes, evidenced by the phenomenon that the photocurrent is mainly focused in the contact area.<sup>141</sup> With this in mind,  $R$  as high as  $5000 \text{ A W}^{-1}$  to 410 nm light and response time as fast as 270  $\mu\text{s}$  were achieved by shrinking the channel length and using graphene contact, respectively.

Taking advantage of the direct bandgap nature, Liu *et al.* demonstrated an exfoliated multilayer GaTe-based photodetector

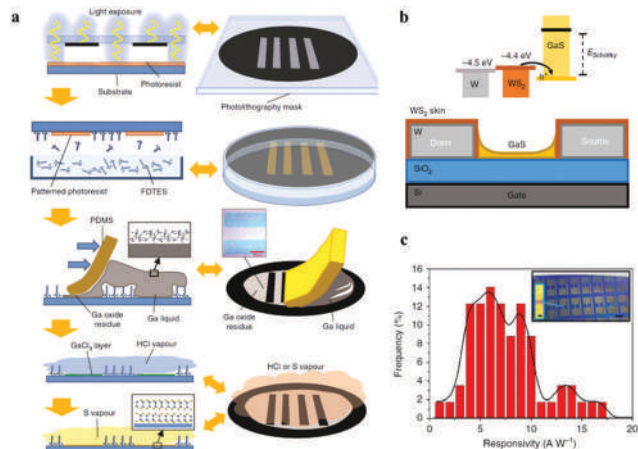


Fig. 7 (a) Schematics of the synthesis process for 2D GaS. First, a pattern of the photoresist is done by lithography. After that, the exposed area of the substrate is covered with vaporized FDTES. Then, place Ga liquid and remove it by PDMS. The final step is a chemical vapour treatment: GaCl<sub>3</sub> layer is formed via exposure to HCl vapour followed by sulfurization through exposure to S vapour to form GaS. (b) Device schematic GaS FET with tungsten/WS<sub>2</sub> electrodes. The inset features the band alignment of the system. (c) The distribution of  $R$  with insets showing the optical image of the fabricated devices and two electrodes. The scale bars are 500 and 20 μm, respectively; (a–c) are reproduced from ref. 136 with permission from Macmillan Publishers Ltd, Copyright 2017.

with responsivity of  $10^4 \text{ A W}^{-1}$  to 532 nm light.<sup>33</sup> Later after that,  $R$  as high as  $244 \text{ A W}^{-1}$  and  $800 \text{ A W}^{-1}$  to 490 nm and 473 nm lights were subsequently demonstrated by Hu *et al.* and Wang *et al.*, respectively.<sup>135,142</sup> Stimulated by the high performances that GaTe had shown, Wang *et al.* successfully synthesized GaTe nanoflakes on mica through van der Waals epitaxy, based on which flexible photodetectors were demonstrated.<sup>143</sup>

**3.2.2 In-Based MMCs.** In-Based MMCs refer to  $\text{In}_x\text{X}_y$ , where  $x = 1$  or 2, and  $y = 1$  or 3. Specifically,  $\text{In}_x\text{Se}_y$  has been the main focus which has diverse structures in bulk state, including  $\alpha$ ,  $\beta$ ,  $\gamma$ ,  $\delta$ , and  $\kappa$  ( $\beta$  and  $\gamma$ ) phases for  $\text{In}_2\text{Se}_3$  (InSe).<sup>147,151–153</sup> Up to now,  $\alpha$ -,  $\beta$ -, and  $\gamma$ -phase  $\text{In}_2\text{Se}_3$ , and  $\gamma$ -phase InSe have been experimentally proven to have layered structures, while the formers/latter are van der Waals connected by Se–In–Se–In–Se quintuple layers or Se–In–In–Se quadruple layers (Fig. 8a–e).<sup>147</sup> Depending on the atom stacking configuration inside the quintuple layer,  $\text{In}_2\text{Se}_3$  can be divided into  $\alpha$  (Fig. 8a and d),  $\beta$  (Fig. 8e), and  $\gamma$  phases (defective wurtzite structure based on Fig. 8d). On the other hand,  $\gamma$ -InSe (or InSe for simplicity) has a structure as shown in Fig. 8f.<sup>148</sup> Companied with this diversity in crystalline structure,  $\text{In}_x\text{Se}_y$  covers a wide-range of bandgaps. For instance, InSe has a direct bandgap of  $\sim 1.26 \text{ eV}$  in bulk, and gradually increases to  $\sim 2.72 \text{ eV}$  for monolayer (Fig. 8g) along with a direct-to-indirect transition at thickness of  $\sim 5 \text{ nm}$ .<sup>144,148,154</sup> while  $\alpha$ - $\text{In}_2\text{Se}_3$  has a thickness-independent direct bandgap with values covering from  $\sim 1.3 \text{ eV}$  for bulk to  $2.8 \text{ eV}$  for  $\sim$  bilayer as shown in Fig. 8g and h.<sup>145,146,149</sup> Note that there may be big differences between optical bandgaps and electric ones because of the considerable exciton binding energy in 2D systems. For example, the PL signal of monolayer

$\alpha$ - $\text{In}_2\text{Se}_3$  was found to locate at  $\sim 801 \text{ nm}$ , corresponding to  $\sim 1.55 \text{ eV}$ .  $\beta$ - $\text{In}_2\text{Se}_3$  was predicted to have an indirect bandgap for all thicknesses with values covered from  $\sim 1.45 \text{ eV}$  for bulk and  $1.58 \text{ eV}$  for  $6.2 \text{ nm}$  (Fig. 8h).<sup>149,152</sup> And  $\gamma$ - $\text{In}_2\text{Se}_3$  was found to have a direct bandgap for the thickness range of  $125\text{--}6 \mu\text{m}$  with the value changing from  $\sim 2.1 \text{ eV}$  to  $\sim 2.5 \text{ eV}$  (Fig. 8i). Besides, similar with its layered analogues, the bandgaps of  $\text{In}_x\text{Se}_y$  can also be modulated by applying in-plane stress. For example, it has been shown that the bandgap of few-layer InSe can decrease/increase by  $160/79 \text{ meV}$  while applying uniaxial tensile/compressive strain of  $1.06\%/0.62\%$ .<sup>155</sup>

Based on the thickness-tunable  $E_g$ , Lei *et al.* systematically studied the photoresponses of InSe with different thicknesses.<sup>157</sup> They found that InSe flakes with 3–4 layers in thickness had an obvious response to light with a wide-range wavelength of  $\sim 400\text{--}800 \text{ nm}$  with a peak located at  $\sim 500 \text{ nm}$ . As the thickness increased, the photoresponse became stronger to a wider range. Using a  $10 \text{ L}$  flake, they demonstrated a photodetector with  $R$  of  $34.7 \text{ mA W}^{-1}$  and response time of  $488 \mu\text{s}$  to  $532 \text{ nm}$  light. Combined with resonant Raman spectra and temperature-dependent photocurrent measurements, the authors found that, due to the suppression of an interlayer interaction and the coupling between electrons and in-plane phonons, more localized orbitals will be involved in the photo-absorption for few-layer samples. This broad spectral response feature was also demonstrated by Tamalampudi and his colleagues where the  $R$  reached up to  $12.3/3.9 \text{ A W}^{-1}$  to  $450/633 \text{ nm}$  light.<sup>158</sup> Mudd *et al.* brought graphene as contact electrodes to construct InSe-based photodetectors.<sup>156</sup> Owing to the higher electron mobility in G and better band alignment of InSe/G, better photoresponse performances were achieved in G contact devices compared with that using traditional metal (Au) (Fig. 9). Under the illumination of  $633 \text{ nm}$  light,  $R$  of as high as  $10^5 \text{ A W}^{-1}$  could be achieved. A similar structure was adopted by Luo *et al.*, where the response time was decreased down to  $120 \mu\text{s}$ .<sup>159</sup> Notably, the response time of an InSe-based photodetector can be further decreased to  $87 \mu\text{s}$  by utilizing high voltage bias ( $50 \text{ V}$ ) where an avalanche photodetector is formed.<sup>160</sup> From the point view of synthesis, wafer-scale InSe film with a thickness down to  $1 \text{ nm}$  has been achieved by pulsed laser deposition (PLD), on the basis of which photodetectors with broad spectral response ( $370\text{--}1000 \text{ nm}$ ) and  $R$  of as high as  $27 \text{ A W}^{-1}$  were demonstrated.<sup>161</sup>

The ultrathin body thickness brings 2DLMs many advantages like strong gate voltage controllability; however, it also makes properties modulation through conventional strategies like chemical doping very difficult. Hence, functionalization by surface decorating has been one of the most widely studied methods to tune the properties of 2DLMs. As for InSe, Lei *et al.* used  $\text{Ti}^{4+}$ -based Lewis acids to decorate the surface of InSe and found that the as-treated flakes showed conduction transition from n- to p-type.<sup>162</sup> In addition, the  $\text{Ti}^{4+}$  cations anchored on the surface of InSe can also be used as a bridge to connect extra functional groups. The authors used a ruthenium-based dye molecule (N719) to the InSe–Ti complex as an example (Fig. 10a). After each step of surface decoration, the photo-absorption and photo-response would change accordingly (Fig. 10b–d). Quantitatively, the

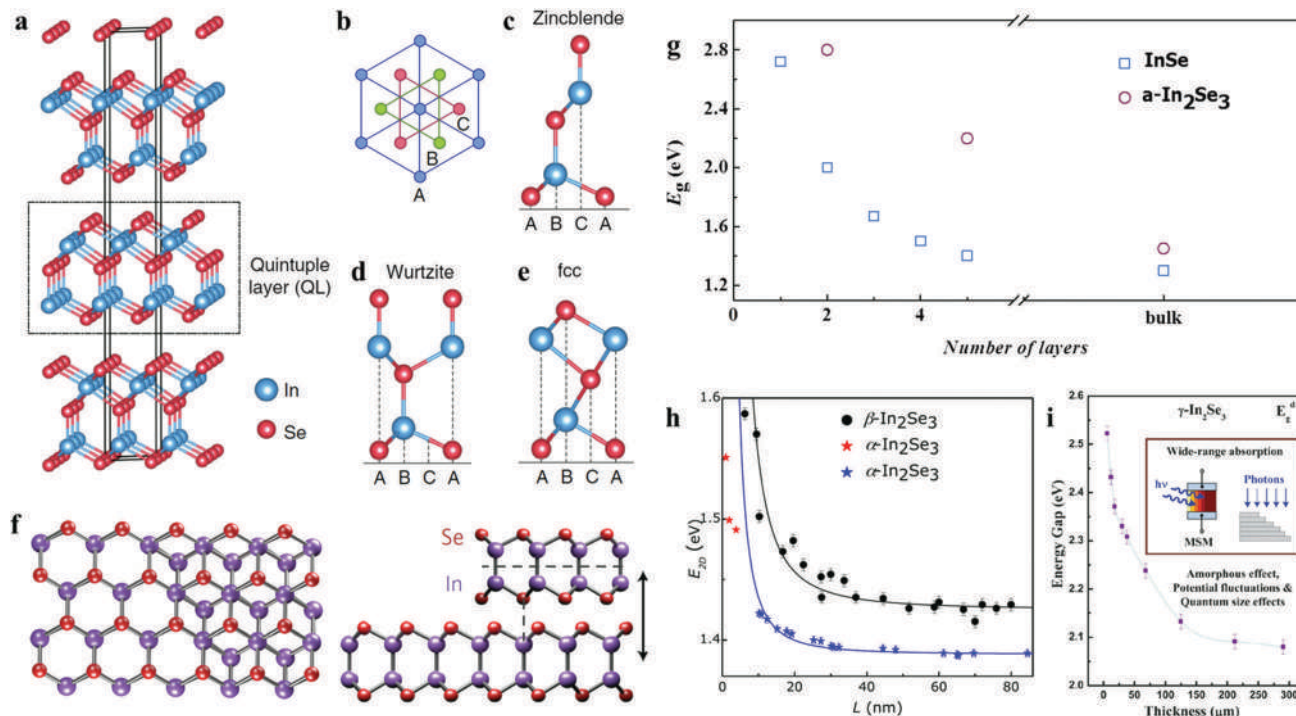


**Fig. 8** (a) Three-dimensional crystal structure of layered  $\alpha$ - $\text{In}_2\text{Se}_3$ , with the top view of the system along the vertical direction shown in (b). The atoms arrange in three types indicated as A, B and C. The representative structures of the quintuple layer for (c) zincblende crystals, (d)  $\alpha$  phase, and (e)  $\beta$  phase. (f) Crystal structure InSe with purple and red spheres corresponding to indium and selenium atoms, respectively. (g) Thickness dependent bandgaps of InSe and  $\alpha$ - $\text{In}_2\text{Se}_3$  with data collected from ref. 144 and 145. (h) Dependence of the PL energy on the layer thickness of  $\beta$ - $\text{In}_2\text{Se}_3$  (black dots), exfoliated  $\alpha$ - $\text{In}_2\text{Se}_3$  (blue stars) and  $\alpha$ - $\text{In}_2\text{Se}_3$  thin layers grown by a CVD method with data collected from ref. 146 (red stars). The lines show the calculated exciton recombination energy. (i) Thickness-dependent bandgaps of  $\gamma$ - $\text{In}_2\text{Se}_3$ . The inset shows a possible application for wide-spectra absorption; (a–e) are reproduced from ref. 147 with permission from Macmillan Publishers Ltd, Copyright 2017, (f) is reproduced from ref. 148 with permission from Macmillan Publishers Ltd, Copyright 2017, (h) is reproduced from ref. 149 with permission from IOP Publishing Ltd, Copyright 2016, and (i) is reproduced from ref. 150 with permission from the Royal Society of Chemistry, Copyright 2013.

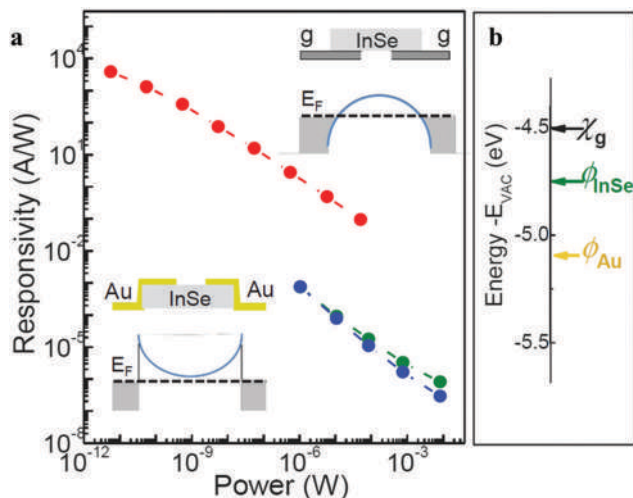


**Fig. 9** (a)  $R$  versus incident laser power at  $\lambda = 633$  nm for graphene/InSe/graphene (top) and Au/InSe/Au devices (bottom) ( $V_{DS} = 2$  V and  $V_{GS} = 0$  V). The inset sketches the band alignments of the two devices. (b) Work functions of Au and InSe, and the electron affinity of graphene; (a) and (b) are reproduced from ref. 156 with permission from John Wiley & Sons, Inc., Copyright 2015.

$R$  increased from 17 to 250, and further to 330  $\text{mA W}^{-1}$  after the treatments of  $\text{Ti}^{4+}$  and dye molecules. On the other hand, the

response became slower after the treatment but still kept in the range of microseconds (Fig. 10d).

The photoresponses of  $\text{In}_2\text{Se}_3$  have also been studied. Jacobs-Gedrim *et al.* used a mechanically exfoliated  $\alpha$ - $\text{In}_2\text{Se}_3$  flake with 10 nm in thickness to fabricate a photodetector.<sup>164</sup> The device exhibited photoresponse to light with wavelengths of  $\sim 300$ –1100 nm, with  $R$  of  $10^3$  to 59  $\text{A W}^{-1}$  to 300 and 500 nm lights. On the basis of synthesized  $\alpha$ - $\text{In}_2\text{Se}_3$  with thickness of  $\sim 10$  nm through van der Waals epitaxy, Lin *et al.* demonstrated a photodetector with  $R$  of  $\sim 2.5$   $\text{A W}^{-1}$ .<sup>165</sup> Zhou *et al.* reported photodetectors based PVD-grown few-layer  $\alpha$ - $\text{In}_2\text{Se}_3$  with  $R$  up to 340  $\text{A W}^{-1}$  to 532 nm light.<sup>146</sup> To approach a step further to practical applications, Zheng *et al.* synthesized single-crystal  $\alpha$ - $\text{In}_2\text{Se}_3$  micro-patterns at centimeter scale by combining a soft imprinting method (using PDMS as stamp) with van der Waals epitaxy, based on which the photodetector arrays were fabricated (Fig. 11a and b).<sup>163</sup> Under 633 nm laser illumination, the devices showed  $R$  of as high as 1650  $\text{A W}^{-1}$  at  $V_{DS} = 5$  V with good uniformity (Fig. 11c and d). Furthermore, the feasible packaging process of the as-synthesized arrays and the mechanical flexibility of the photodetectors after packaging were also demonstrated (Fig. 11e and f). On the other hand, wafer-scale  $\alpha$ - $\text{In}_2\text{Se}_3$  films have been synthesized by PLD, based on which the broad spectral photoresponse (370 to 1064 nm) with a highest  $R$  of 44  $\text{A W}^{-1}$  was illustrated.<sup>166</sup>



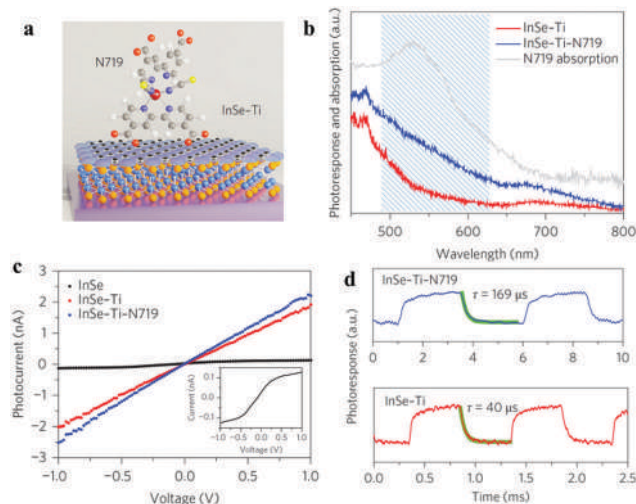


**Fig. 10** (a) Schematic of the N719-functionalized InSe-Ti complex. (b) Photo-absorption of InSe-Ti complex, InSe-Ti-N719, and N719 molecules. (c) Photocurrent of InSe before (black), after Ti treatment (red) and N719 treatment (blue). Inset: Magnified InSe photocurrent. (d) Response time of InSe-Ti and InSe-Ti-N719. (a–d) are reproduced from ref. 162 with permission from Macmillan Publishers Ltd. Copyright 2016.

$\beta$ - $\text{In}_2\text{Se}_3$  obtained from both mechanical exfoliation and bottom-up synthesis also have been found to show high-performance photoresponses. Using an exfoliated flake with a thickness of  $\sim 14$  nm, Island *et al.* reported a broad-spectra response (400–960 nm) of  $\beta$ - $\text{In}_2\text{Se}_3$ .<sup>167</sup> Due to a strong photogating

effect, the  $R$  of the device could reach  $10^5 \text{ A W}^{-1}$  under the illumination of 640 nm light. On the other hand, the high-performance wide-band response was also demonstrated in devices based on grown flakes.<sup>153</sup>

**3.2.3 Ge-Based MMCs.** Ge-Based MMCs, including GeS and GeSe, have a distorted NaCl-type crystalline structure. GeS has a direct electric bandgap of  $\sim 1.68$  eV in bulk, and gradually changes to an indirect bandgap of  $\sim 2.64$  eV for monolayer.<sup>168,169</sup> On the other hand, GeSe has an indirect bandgap of  $\sim 1.10$  eV in bulk, and gradually increases to 1.87 eV along with transition to direct bandgap in monolayer.<sup>170</sup> Research on photodetection of Ge-based MMCs started relatively later than its analogues, which is probably due to the difficulties of synthesizing/exfoliating atomically thin flakes with high-enough crystalline quality. Even now, reports on high-quality bottom-up synthesis of Ge-based MMCs is still rare. It has been shown that GeS/Se usually grew in a vertical way through a CVD method, which is probably due to poor control of the sources.<sup>171–173</sup> Photodetectors with planar configurations based materials usually need an additional transfer method.<sup>173</sup> Ulaganathan *et al.* fabricated a photo-detector based on a mechanically exfoliated GeS flake with a thickness of  $\sim 28$  nm showing response to wide spectra of  $\sim 400$ – $800$  nm with a highest  $R$  of  $\sim 655 \text{ A W}^{-1}$  at 633 nm light.<sup>169</sup> Similar wide-spectra response (300–800 nm) has been found by Tan *et al.*, but with higher  $R$  of  $2.3 \times 10^4 \text{ A W}^{-1}$  for 500 nm light.<sup>174</sup> Recently, Hsueh *et al.* studied the polarized light dependent band-edge absorption behavior of GeS.<sup>168</sup> Due to a special band dispersion, the bandgaps of GeS show a

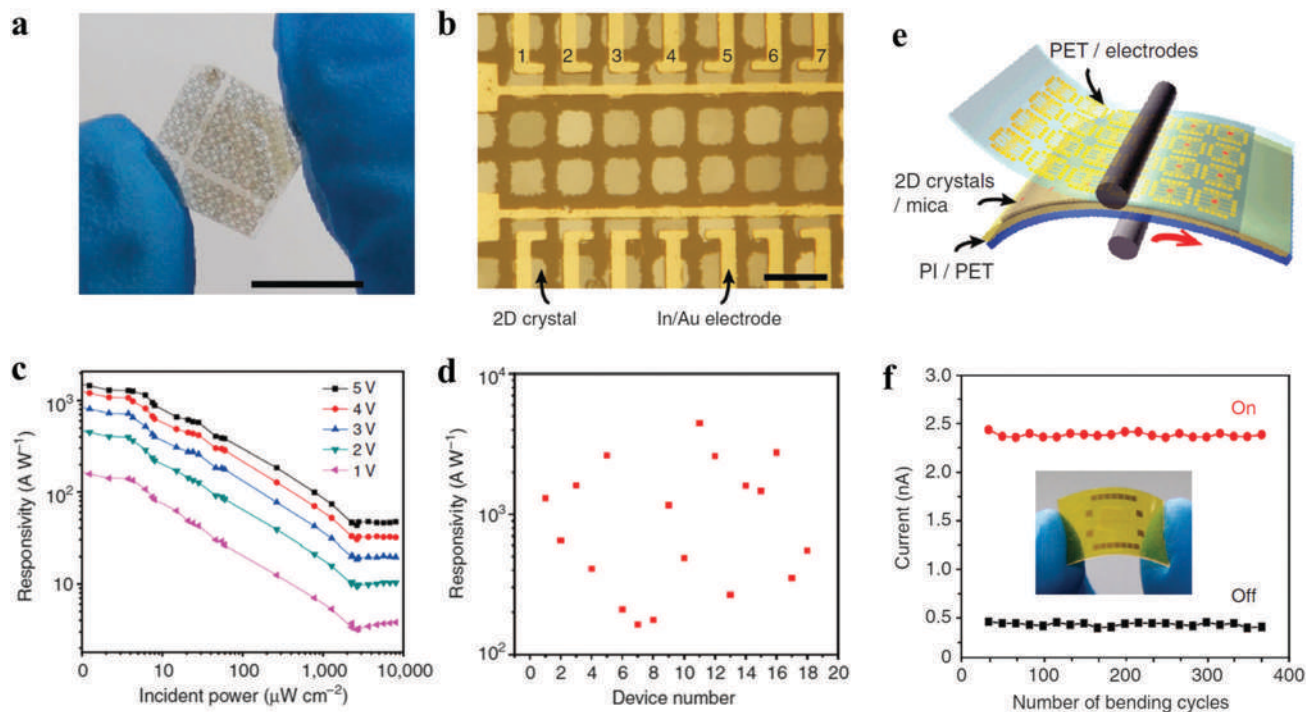


**Fig. 11** (a) Photograph and (b) optical microscope image of  $\alpha$ - $\text{In}_2\text{Se}_3$  photodetector arrays on mica substrate. Scale bars in (a) and (b) are 1 cm and 20 mm, respectively. (c) Dependence of  $R$  on illumination intensities and voltage bias. (d) Statistic distribution of  $R$   $\alpha$ - $\text{In}_2\text{Se}_3$  photodetectors. (e) Schematic of device packaging. (f) Current as a function of bending cycles (10 mm radius) of the packaged  $\alpha$ - $\text{In}_2\text{Se}_3$  photodetector devices at a bias voltage of 5 V. The inset shows the photograph of packaged device; (a–f) are reproduced from ref. 163 with permission from Macmillan Publishers Ltd, Copyright 2015.



sinusoidal variation of  $E_g = 1.6 + 0.05 \cdot |\sin \theta|$  eV with the polarization angle ( $\theta$ ) changes. Compared to GeS, GeSe may have more appealing photoresponse properties due to its special band structure. For GeSe, the CBM and VBM mainly consisted of Ge 4p and Se 4p orbits, respectively, leading to a large number of bands at the band extrema (which leads to a high DOS) and large directionally averaged effective masses. Consequently, GeSe has a large absorption for visible light even down to monolayer (38%).<sup>170</sup> This was more or less demonstrated by Ramasamy *et al.*'s study, in which a higher  $R$  for GeSe ( $870 \text{ A W}^{-1}$ ) compared with GeS ( $173 \text{ A W}^{-1}$ ) at 405 nm light was found.<sup>175</sup>

**3.2.4 Sn-Based MMCs.** Similar with In-based MMCs, the Sn-based materials family has a variety of forms with stoichiometric ratios of 2 : 1 and 1 : 1, including SnS/Se<sub>2</sub> and SnS/Se. The former has a 1T MoS<sub>2</sub>-like structure while the latter shares a similar structure with buckled BP.<sup>176–178</sup> This multi-formation brings Sn-based MMCs an additional freedom of property tunability. For example, SnS<sub>2</sub> and SnS exhibit n- and p-type conductions, respectively, making the fabrication of functional heterojunctions through only changing the stoichiometry available.<sup>176</sup> This potential is further enabled considering that controllable synthesis of SnSe/SnSe<sub>2</sub> and SnS/SnS<sub>2</sub> have been achieved by Huang *et al.* and Ahan *et al.* independently.<sup>176,178</sup> From the point view of band structure, SnSe<sub>2</sub>/SnSe keep an indirect bandgap nature while tuning the thickness from bulk ( $\sim 1.2/0.89$  eV) to monolayer ( $\sim 2.04/1.63$  eV). On the other hand, the bandgaps of SnS<sub>2</sub>/SnS can be modulated from 2.55/0.89 to 2.81/2.61 eV while decreasing down to monolayer.<sup>179–181</sup> For SnS/Se<sub>2</sub>, it has been calculated that VBMs reside at a point along the line  $\Gamma$ - $M$ , and the CBMs reside at the  $M$  point. While thinning down to monolayers, they both experience a slight flattening of the VBMs, which induces an increase in DOS (density of states). In addition, DOS of their monolayers and bilayers have van Hove singularities. Both of these characters may bring high photo-absorption to SnS/Se<sub>2</sub>.<sup>179</sup> Due to the large polarizabilities of Sn atoms, the exciton binding energies of their monolayers are 0.91 eV and 0.86 eV for SnS<sub>2</sub> and SnSe<sub>2</sub>, respectively, which is substantially more than those of MoS<sub>2</sub>, indicating that excitations may play a dominant role in their optoelectronic properties.<sup>179</sup> Notably, for SnSe, it has been shown that its CBM and VBM mainly consist of Sn 5p and Se 4p orbits, respectively, inducing a high DOS and large directionally averaged effective masses like GeSe. As a result, SnSe has a large absorption for visible light even down to bilayer (47%).<sup>170</sup>

Among various forms, the photoresponse properties of SnSe<sub>2</sub> and SnS<sub>2</sub> have been mainly studied. Zhou *et al.* fabricated a photodetector using CVD-grown SnSe<sub>2</sub> flakes with a thickness of  $\sim 3$  nm.<sup>177</sup> An optical bandgap of  $\sim 1.78$  eV and obvious response to light with wavelengths lower than  $\sim 600$  nm was found. The as-fabricated device showed  $R$  and  $G$  as high as  $1.1 \times 10^3 \text{ A W}^{-1}$  and 5000, respectively, to 530 nm light. At the same time, fast rise and decay times of 14.5 and 8.1 ms were observed, which the authors ascribed to the high quality of the as-synthesized samples as well as existence of a Schottky barrier

at the contact regions. Using micro-absorption spectra, Wu and his colleagues extracted an indirect bandgap of  $\sim 1$  eV for a CVD synthesized SnSe<sub>2</sub> with a thickness of 50 nm. On the basis of the same device, they observed fast photoresponse speed with rise and decay times of 17 and 45  $\mu\text{s}$ , respectively, which leads to a large bandwidth that can sustain frequency as high as 2 kHz.<sup>182</sup> Yu *et al.* fabricated a photodetector based on a bilayer exfoliated SnSe<sub>2</sub> flake which displayed  $R$  of  $0.5 \text{ A W}^{-1}$  to 633 nm light.<sup>183</sup> Raman spectroscopy has been shown to be a feasible tool to define the thickness of SnSe<sub>2</sub>, in which the difference between the two Raman peaks, namely  $E_g$  and  $A_{1g}$  (located at  $\sim 110$  and  $\sim 188 \text{ cm}^{-1}$ , respectively), increases as the thickness decreases.<sup>184</sup> The photoresponse range of SnSe<sub>2</sub> can extend to the IR range. Using thick films, Mukhokosi *et al.* demonstrated SnSe<sub>2</sub> photodetectors with  $R$  as high as  $\sim 2 \text{ mA W}^{-1}$  to 1064 nm light. On the other hand, Huang *et al.* fabricated photodetectors based on a mechanically exfoliated SnS<sub>2</sub> with a thickness of  $\sim 10$  nm which showed  $R$  of  $\sim 100 \text{ A W}^{-1}$  to 532 nm light.<sup>185</sup> On the basis of successful synthesis of SnS<sub>2</sub> flakes, Ahan *et al.* studied their thickness-dependent photodetection properties.<sup>176</sup> They also fabricated p-n junctions using the synthesized n-type SnS<sub>2</sub> and p-type SnS and demonstrated a photodetector and photodiode with  $R$  of 4.56 and 27.09  $\text{mA W}^{-1}$  (405 nm light) at forward and reverse bias, respectively. Recently, Zhou *et al.* further improved the  $R$  of photodetectors based on CVD-grown SnS<sub>2</sub> (10 nm in thickness) to  $722 \text{ A W}^{-1}$  (350 nm light).<sup>186</sup>

All the photodetectors mentioned above utilized a planar configuration based on individual single-crystal flakes, which has been the most commonly used strategy to study the intrinsic photodetection properties of 2DLMs. Nevertheless, this kind of device structure can only be used as a prototype because of its limited active area. To achieve practical applications, large-scale synthesis of 2DLMs films is necessary. However, 2D-film morphology may still suffer from strong light reflection of the substrate. On the other hand, vertically grown 2DLMs could be an alternative choice considering the high probability of light scattering inside the vertical "walls" and the higher in-plane charge carrier mobilities.<sup>187,188</sup> Recently, devices based on vertically grown SnS, SnS<sub>2</sub>, and SnSe have been reported.<sup>188–191</sup> For example, Liu *et al.* synthesized free-standing vertical SnS<sub>2</sub> on SiO<sub>2</sub>/Si and FTO substrates through a modified CVD method.<sup>188</sup> Using a FTO substrate and deposited Au with 20 nm in thickness as bottom and top electrodes, respectively, the authors fabricated photodetectors in vertical geometry. The devices showed  $R$  as high as  $1.85 \text{ A W}^{-1}$  with fast response times of  $\tau_r/\tau_d \sim 43.4/64.4$  ms to 490 nm light.<sup>188</sup> In another case, Patel *et al.* synthesized a wafer-scale SnS with vertical morphology through a two-step sulfurization method. By combining with an n-type Si substrate, a SnS-Si photodiode was fabricated which showed  $R$  as high as  $0.25 \text{ A W}^{-1}$  with a fast response time of  $\tau_r/\tau_d \sim 34/15.1$   $\mu\text{s}$  to 850 nm light.<sup>189</sup>

### 3.3 Transition metal trichalcogenides

Besides the well-known TMDs with a stoichiometric ratio of 1 : 2, transition metal trichalcogenides (TMTs) in the form of MX<sub>3</sub>, where M and X represent transition metals like Ti, Zr,

or Hf, and chalcogens of S, Se, or Te, respectively, also have a layered structure.<sup>192–194</sup> Two types of crystalline structures (with small differences) have been reported for this materials family, *i.e.*, TiS<sub>3</sub> type and ZrSe<sub>3</sub> type.<sup>194</sup> Fig. 12a shows TiS<sub>3</sub> as an example. Especially, each monolayer (*a*–*b* atomic plane) can be seen as a connection of [TiS<sub>6</sub>] triangle prisms along the *b*-axis (dashed red rectangle), which leads to a strong in-plane anisotropy or the so-called quasi-1D properties that is similar with Te.<sup>195–197</sup> For example, a theoretical calculation has shown that the effective mass of electrons are 1.47 and 0.41 along *a* and *b* directions, respectively, resulting a two-order difference in mobility.<sup>195</sup> Experimentally, in-plane anisotropy of 2.1 in conductivity at RT (4.4 at 25 K) was found using a circular electrodes configuration (Fig. 12b). In addition, TiS<sub>3</sub> also shows anisotropic light absorption with photon energy of 1.5 to 3 eV where a higher absorption can be observed for light polarized along *E*//*b*.<sup>195</sup> These features suggest TiS<sub>3</sub> may have similar properties with the well-studied BP.

In bulk states, most of TMTs, including (Ti, Zr, or Hf) (S or Se)<sub>3</sub>, are semiconductors with indirect bandgaps covering from ~0.21 to 1.87 eV, whereas transition metal tritellurides (Ti/Zr/HfTe<sub>3</sub>) are metals.<sup>192</sup> While decreasing the thickness, the bandgaps increase due to quantum confinement just like its 2D analogues, as summarized in Table 2. Among them, one specialty is TiS<sub>3</sub>, which undergoes an indirect-to-direct bandgap transition without a big change in value. TMTs also show strain-tunable bandgaps.<sup>193,199</sup> Through a DFT calculation, Li *et al.* predicted monolayers of TMTs can be modulated from 0.68 eV to 2.34 eV at a small tensile strain (<8%).<sup>193</sup> Fig. 12c and d show their results in detail. Interestingly, they found ZrS<sub>3</sub> and HfS<sub>3</sub> monolayers will exhibit an indirect-to-direct bandgap transition, while TiS<sub>3</sub> keep

Table 2 Bandgaps of bulk and monolayer Ti- and Zr-based TMTs, respectively. The data are extracted from ref. 192

		$E_g$ (eV) bulk	$E_g$ (eV) 1L			$E_g$ (eV) bulk	$E_g$ (eV) 1L
Ti	S	1.02 <sup>i</sup>	1.06 <sup>d</sup>	Zr	S	1.83 <sup>i</sup>	1.90 <sup>i</sup>
	Se	0.21 <sup>i</sup>	0.57 <sup>i</sup>		Se	0.75 <sup>i</sup>	1.17 <sup>i</sup>
	Te	0	0		Te	0	0

i and d: indirect and direct bandgap. 1L: monolayer.

the direct bandgap feature for the whole strain range, and metallic ZrTe<sub>3</sub> and HfTe<sub>3</sub> monolayers can change to be semiconductors at  $\epsilon = 4\%$  and  $\epsilon = 6\%$ , respectively.

Until now, research on TMTs is still rare and most of the works are done from a theoretical direction. As time goes on, a number of works on TMTs have recently been published with TiS<sub>3</sub> as the representative prototype. This is mainly because of its moderate bandgap (comparable with Si) and high theoretical mobility. Both bottom-up and top-down methods have been used to obtain nanostructured TiS<sub>3</sub>.<sup>198,200</sup> For the former, the as-synthesized TiS<sub>3</sub> usually appears in the morphology of a nanobelt due to its quasi-one dimensional crystalline structure as we have shown above.<sup>198,201–203</sup> For example, Island *et al.* grew TiS<sub>3</sub> nanobelts by *in situ* sulfurizing Ti disks, on the basis of which (22 nm in thickness) phototransistors were fabricated.<sup>198</sup> Broad-spectra response (~500 nm to 900 nm) with a highest *R* of 2910 A W<sup>-1</sup> to 640 nm light was demonstrated (Fig. 12i). In addition, the device was found to show fast response and could keep a *R* of ~16 A W<sup>-1</sup> at 1 kHz switching frequency. On the other hand, Liu *et al.* studied the anisotropic photoresponse properties of TiS<sub>3</sub> flakes obtained by a mechanical exfoliation method.<sup>200</sup> As expected, the devices showed stronger response to light (532 to 808 nm) with polarization along the *b* axis.

### 3.4 Tetradymites

Tetradymites refer to compounds with a form of M<sub>2</sub>X<sub>3</sub>, where M stands for Bi or Sb, and X stands for chalcogens (S, Se, or Te).<sup>204</sup> Among them, Bi<sub>2</sub>S<sub>3</sub>, Bi<sub>2</sub>Se<sub>3</sub>, Bi<sub>2</sub>Te<sub>3</sub>, and Sb<sub>2</sub>Te<sub>3</sub> are archetypical ones which share a similar layered structure: covalently bonded quintuple layers of X1–M–X2–M–X1 are connected by a weak van der Waals force.<sup>204</sup> Theoretical and experimental studies have shown that Bi<sub>2</sub>S<sub>3</sub>, Bi<sub>2</sub>Se<sub>3</sub>, Bi<sub>2</sub>Te<sub>3</sub>, and Sb<sub>2</sub>Te<sub>3</sub> have direct bandgaps of ~1.3, 0.35, 0.21, and 0.45 eV in bulk form, respectively, which makes them promising candidates for broad-spectra photodetection.<sup>205–208</sup> More importantly, another feature makes three members of them (Bi<sub>2</sub>Se<sub>3</sub>, Bi<sub>2</sub>Te<sub>3</sub>, and Sb<sub>2</sub>Te<sub>3</sub>) stand out, *i.e.*, the gapless surface states consisting of odd number of Dirac cones – the so-called topological insulators (TIs) – due to their strong spin-orbit.<sup>209–211</sup> These natural 2D TIs with macroscopic quantum-entanglement effects, like the quantum spin Hall (QSH) effect, have been predicted to show potential applications on brand-new electronic (low-power electronics and error-tolerant quantum computing, *etc.*) and optoelectronic devices.<sup>212</sup>

Holding small direct bandgaps in bulk states, tetradymites have been utilized to construct photodetectors and/or as light absorbers for broad-spectra wavelengths. For instance, Qiao *et al.*

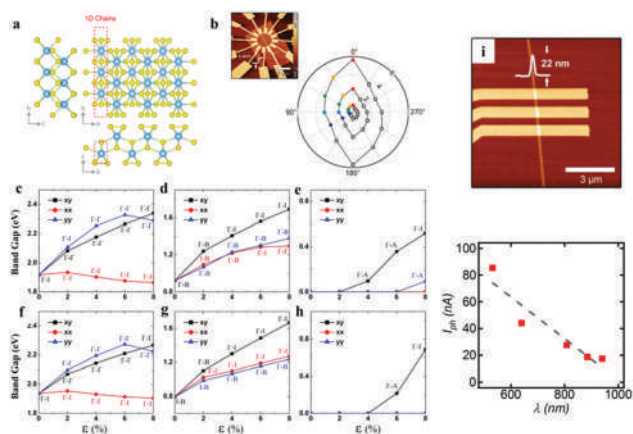


Fig. 12 (a) Crystal structure of TiS<sub>3</sub>. (b) Polar plot of conductance measured for all 12 pairs of electrodes at back gate voltages of -40 V, 0 V, and 40 V, respectively. The inset shows the AFM scan of the device. Computed bandgaps of (c) ZrS<sub>3</sub>, (d) ZrSe<sub>3</sub>, (e) ZrTe<sub>3</sub>, (f) HfS<sub>3</sub>, (g) HfSe<sub>3</sub>, and (h) HfTe<sub>3</sub> monolayers versus the biaxial or uniaxial tensile strain. (i) The top panel shows the AFM image of a device, while the bottom panel shows the photocurrent measured as a function of different laser wavelengths; (a and b) are reproduced from ref. 195; (c–h) are reproduced from ref. 193 with permission from the Royal Society of Chemistry, Copyright 2015, and (i) is reproduced from ref. 198 with permission from John Wiley & Sons, Inc., Copyright 2014.

fabricated photodetectors using a G/Bi<sub>2</sub>Te<sub>3</sub> hybrid structure with Bi<sub>2</sub>Te<sub>3</sub> nanoplates uniformly dispersed on the G channel.<sup>213</sup> With assistance of Bi<sub>2</sub>Te<sub>3</sub> light absorbers, the device showed obvious photoresponse to wide-wavelength light of ~400 to 1500 nm with a highest  $R$  of 3.5 A W<sup>-1</sup> at 532 nm, which is about two orders higher than from pure G photodetectors. In another case, Kim *et al.* fabricated Bi<sub>2</sub>Se<sub>3</sub>/G heterostructure and demonstrated good response to mid-infrared light (1.3 to 3.5 μm) with a highest  $R$  of 1.97 A W<sup>-1</sup> at 3.5 μm.<sup>214</sup> More importantly, the device exhibited a fast response speed (4 μs), which is remarkable for photodetectors working in the IR range. Zhang *et al.* synthesized Bi<sub>2</sub>Se<sub>3</sub> film on the top of a Si wafer, on the basis of which photodiodes were fabricated *in situ* and their photoresponse properties were studied.<sup>215</sup> Due to the sharp interface between Bi<sub>2</sub>Se<sub>3</sub> and n-doped Si, the photodiodes showed high-performance broadband photoresponse (300–1100 nm). Under reverse bias conditions, the devices showed fast response speed (a few microseconds) and high  $R$  (24.48 A W<sup>-1</sup> to 808 nm light). A similar structure was also studied for Bi<sub>2</sub>Te<sub>3</sub> but with the main focus on the IR range (1064 to 1550 nm), where Bi<sub>2</sub>Te<sub>3</sub> dominates photo-absorption.<sup>216</sup> All the works mentioned above demonstrate the high compatibility of tetradymites, whether in the forms of nanostructures or films, with both the widely studied 2DLMs and conventional semiconductors.

The second feature of tetradymites is their outstanding thermoelectric (TE) properties.<sup>204</sup> Simultaneously having high electron mobility/conductivity due to a strong SOC-induced small effective mass, and high thermopower, because of the high valley degeneracy and small phonon group velocities *etc.*, tetradymites, especially Bi<sub>2</sub>T<sub>3</sub>-based ones, have been proven to

show high  $ZT$  values for thermoelectric devices. As a result, tetradymites-based photodetectors utilizing PTE are expected soon. Very recently, Mauser *et al.* proposed a new-type of photodetector by combining PTE and plasmonic resonance.<sup>217</sup> The photodetector was composed of a Bi<sub>2</sub>Te<sub>3</sub>/Sb<sub>2</sub>Te<sub>3</sub> p-n array in an inter-finger configuration while two electrode pads independently connected to the p- and n-type materials (Fig. 13a). The periodic array acts as a resonator strongly enhancing coupling between the TE device and incident light with specific wavelengths. On the other hand, the electrode pads reflect most of the light and keep cooling for the whole period. As a result, a steep temperature gradient will be induced at the array and pads parts (Fig. 13b). PTE current is then produced due to the opposite flow directions of charge carrier between p- and n-type TE materials. One key advantage of this photodetector is tunable resonant light wavelength from the parameters of the array, which potentially offers broadband photodetection without a cut-off energy (Fig. 13c and d). In addition, high sensitivity ( $R$  and NEP as high/low as a few V W<sup>-1</sup> and nW Hz<sup>-1/2</sup>) and fast response (in the scale of microseconds) have been demonstrated by the authors (Fig. 13e and f).

The role of tetradymites, specifically TIs, goes beyond the traditional photoresponse process while considering the topologically protected surface states (SS). One of the specialties lay on the SS-related IR to THz detection. Zhang *et al.* first predicted this potential from a theoretical perspective.<sup>35</sup> Due to the Dirac nature of SS in Bi<sub>2</sub>Se<sub>3</sub> thicker than 6 QLs, the absorption of light with energy ranging from 0 to 0.3 eV (the bulk bandgap) is solely determined by the fine structure constant, just like what has

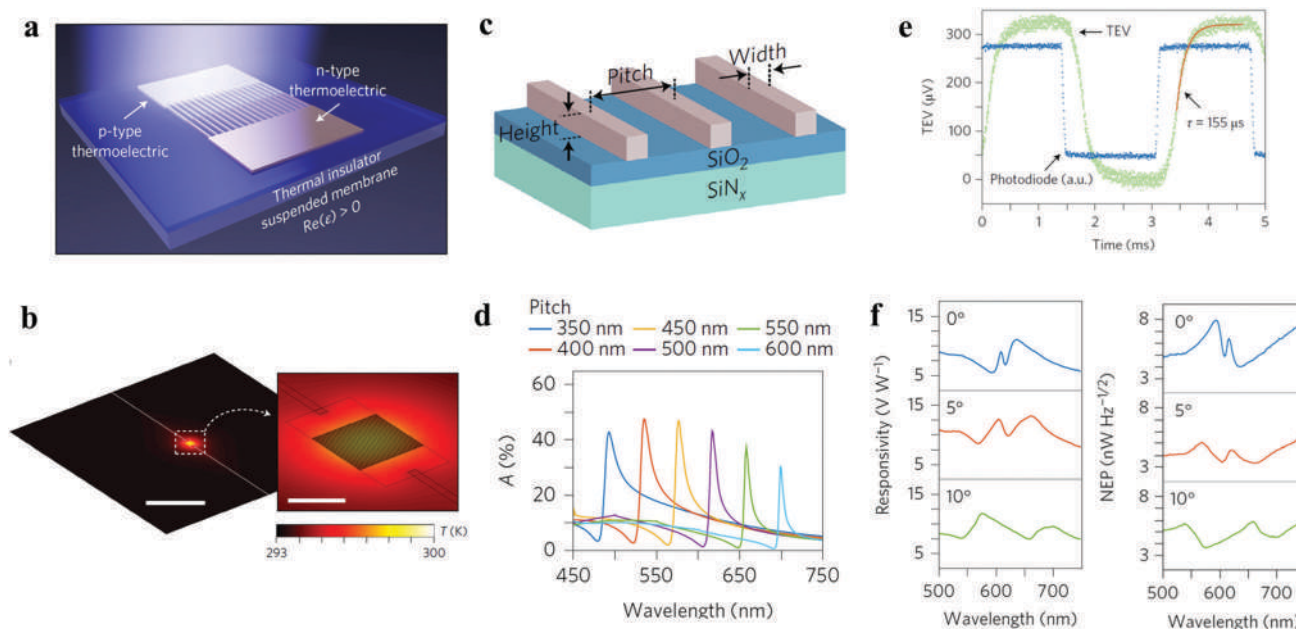


**Fig. 13** (a) Conceptual design of the Bi<sub>2</sub>Te<sub>3</sub>/Sb<sub>2</sub>Te<sub>3</sub> PTE device. (b) A thermal simulation of the Bi<sub>2</sub>Te<sub>3</sub>/Sb<sub>2</sub>Te<sub>3</sub> structure at peak absorption with input power of 20 μW. Scale bars, 500 μm (main image); 50 μm (inset). (c) Geometry of the Bi<sub>2</sub>Te<sub>3</sub>/Sb<sub>2</sub>Te<sub>3</sub> PTE device. (d) Calculated absorption of 60 nm-wide wires with thicknesses of 40 nm and varying pitch on suspended 50 nm SiO<sub>2</sub>/100 nm SiN<sub>x</sub> waveguides. (e) Time response of a Bi<sub>2</sub>Te<sub>3</sub>/Sb<sub>2</sub>Te<sub>3</sub> PTE device. (f) Responsivity (left) and NEP as a function of wavelength for unfocused, spatially uniform illumination; (a–f) are reproduced from ref. 217 with permission from Macmillan Publishers Ltd, Copyright 2017.



been found in G.<sup>15</sup> For suspended samples, the absorption is  $\sim 1.15\%$ , which is two orders higher than the commercially used  $\text{Hg}_{1-x}\text{Cd}_x\text{Te}$  with an equivalent thickness. For  $\text{Bi}_2\text{Se}_3$  thinner than 6 QLs, the opened gap at SS will lead to a further increase in absorption around the band edge (1.8%, 2.05%, 3.85%, and 6.22% for 2, 3, 4, and 5 QLs, respectively). With this high absorption,  $\text{Bi}_2\text{Se}_3$  has been predicted to show higher SNR than  $\text{Hg}_{1-x}\text{Cd}_x\text{Te}$  detectors.

Due to the strong relationship between THz response and gapless Dirac SS, THz technology was used as a tool to detect SS signals at an early age of TIs.<sup>219–222</sup> As research progressed, their role in room-temperature THz-IR detection began to attract growing attention. However, to explicitly define the contribution of SS is not easy because of the mixed role of intraband transition from the bulk gap and the complex mechanisms underlying THz-IR detection.<sup>223</sup> Recently, Viti *et al.* fabricated THz detectors based on  $\text{Bi}_2\text{Te}_{2.2}\text{Se}_{0.8}$  FETs (Fig. 14a and b).<sup>218</sup> The THz detectors were found to work under the rectification plasma-wave mechanism in an overdamped range, with a highest (lowest)  $R$  (NEP) of  $\sim 210 \text{ mV W}^{-1}$  ( $10 \text{ nW Hz}^{-1/2}$ ) at 332.6 GHz radiation (Fig. 14c and d). In addition, the detectors were also applied for practical imaging (Fig. 2e and f). The contribution of SS to the THz response was defined by comparing the properties with

$\text{Bi}_2\text{Se}_3$ -based devices, in which a photothermoelectric effect dominates the response process. And the reason(s) for the increased contribution of SS in  $\text{Bi}_2\text{Te}_{2.2}\text{Se}_{0.8}$  is probably decreased conductivity of the bulk states due to composite doping. Based on this high-performance THz detector, practical imaging has been demonstrated (Fig. 14e and f). Notably, besides chemical doping, the SS related photocurrent can be further enhanced by introducing a magnetic field into the device.<sup>224,225</sup>

Another feature caused by the SS of TIs is a spin polarized photocurrent that is sensitive to circular light (circular photogalvanic effect, CPGE). For the SS, the spin is strongly locked with momentum due to spin-orbit coupling. Hence, circularly polarized light can induce inter-band transitions of electrons with a probability that is sensitive to the momentum dependent spin orientation. As a result, the SS can be asymmetrically depopulated in  $k$ -space, which converts the pure spin currents to a net spin-polarized electrical current.<sup>227,228</sup> Theoretical works have shown that the CPGE is experimentally detectable on TIs like  $\text{Bi}_2\text{Se}_3$  (Fig. 15d).<sup>227</sup> However, effectively isolating the spin-polarized SS current from the spin-degenerate bulk current is challenging in practice. McIver *et al.* achieved this goal by carefully designing the experimental parameters.<sup>226</sup>

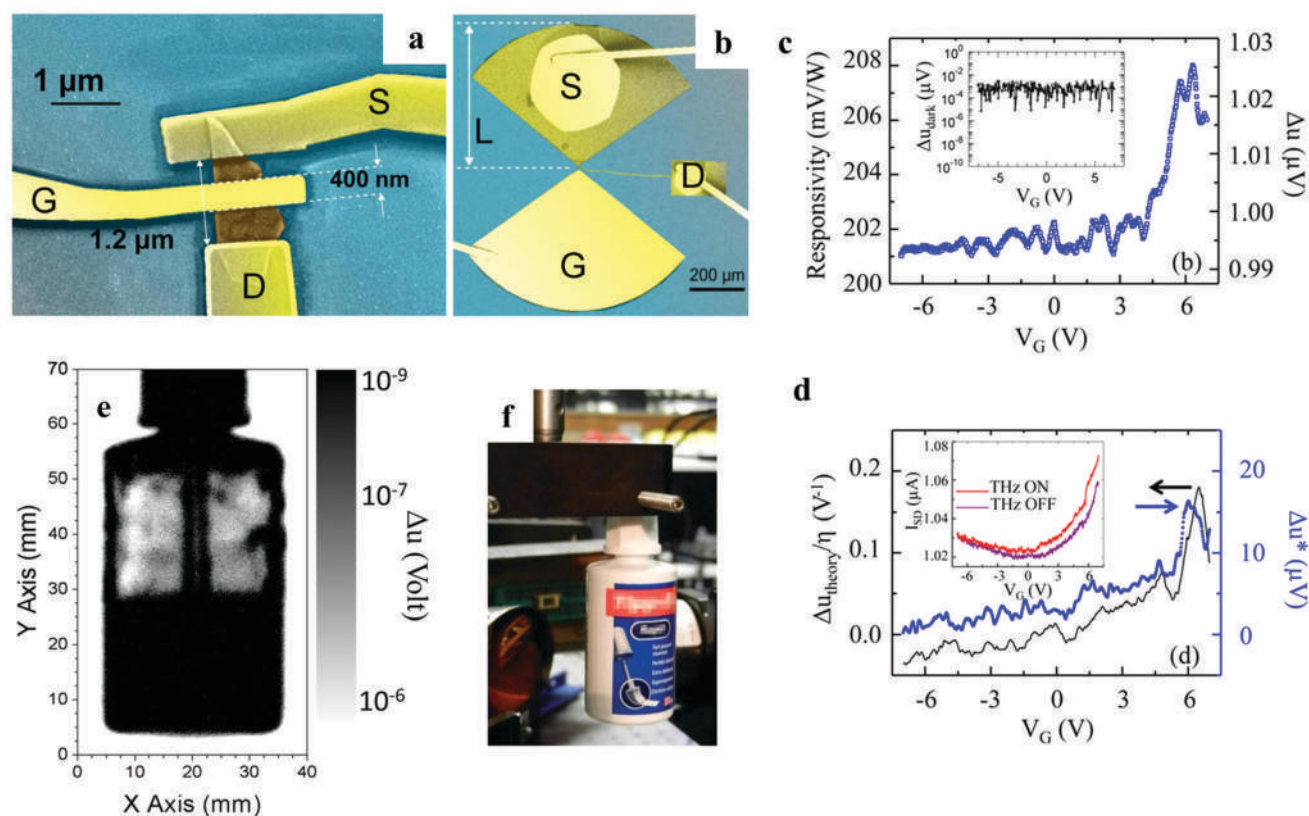


**Fig. 14** (a and b) False-colored SEM images of the top-gated FET. (c) Gate dependent responsivity (left vertical axis) and photovoltage (right vertical axis) measured at RT with a 332.6 GHz radiation. Inset: Background signal. (d) Left vertical axis: extrapolated photovoltage as predicted by the Dyakonov–Shur overdamped plasma-wave theory, divided by the antenna coupling constant. Right vertical axis: difference between the source–drain currents measured while focusing the THz beam on the sample and without it, multiplied by the channel resistance. Inset: Transconductance curve collected while shining the 332.6 GHz radiation on the detector.  $V_{DS} = 0.6 \text{ mV}$ . (e) RT THz imaging of a (f) glue jar obtained at 332.6 GHz radiation; (a–f) are reproduced from ref. 218 with permission from American Chemical Society, Copyright 2015.



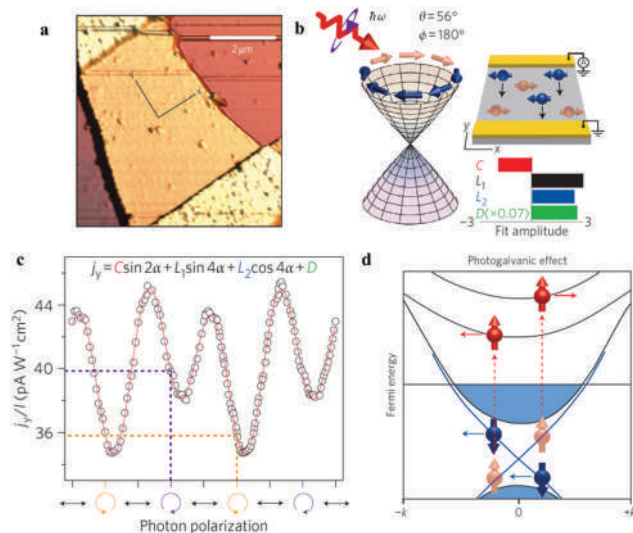


**Fig. 15** (a) AFM image of a typical two-terminal  $\text{Bi}_2\text{Se}_3$  device. (b) Schematics of the SS-related CPGE at a specular incident condition. (c) Polarization dependent spin current. The solid red line is a fit to the equation shown in the graph. (d)  $k$ -Space depiction of photon helicity-induced currents from the Dirac cone via the circular photogalvanic effect including contributions from excited states; (a–d) are reproduced from ref. 226 with permission from Macmillan Publishers Ltd, Copyright 2011.

They used  $\text{Bi}_2\text{Se}_3$  (Fig. 15a) as the TI and polarized 795 nm light as the radiation. At a particular incident angle, they found the photocurrent shows a strong polarization dependency (Fig. 15b and c), which is ascribed to the CPGE. This result shows the potential role of TIs on opto-spintronic applications.

### 3.5 hBN

Hexagonal BN (hBN) is a special 2DLM which has a crystalline structure with a honeycomb arrangement of alternating boron and nitrogen atoms. The similarity in structure with G makes hBN also known as “white graphene”. With a wide bandgap ( $\sim 6$  eV), large dielectric breakdown strength ( $\sim 8 \text{ MV cm}^{-1}$ ), high chemical stability, and atomically flat surface, hBN has been widely used for tunnelling barriers, encapsulation layers, and substrates/buffer layers to protect 2DLMs from interface scatterings to achieve high mobility. The bandgap nature of hBN experienced a long history of debating. Theoretical calculations showed that hBN has an indirect bandgap while light emission measurements indicated a direct nature.<sup>229–232</sup> Recently, this long-debated issue was resolved by two-photon spectra which demonstrated the indirect bandgap nature with a value of 5.955 eV.<sup>233</sup> Meanwhile, an exciton binding energy of 130 meV was revealed giving rise to a single-particle bandgap of 6.08 eV.

hBN itself has also been studied as a UV optoelectronics and natural hyperbolic material. It was first studied as a UV light-emitting material. In a pioneering work, Watanabe *et al.* demonstrated hBN room-temperature UV lasing at 215 nm, which was ascribed to the direct bandgap nature of hBN.<sup>232</sup> A step further, a far-ultraviolet (FUV, 225 nm) plane-emission device that emits FUV light from an hBN fluorescent screen source was fabricated.<sup>234,235</sup> On the other hand, hBN-based UV photodetectors have also

been explored. Jiang and his colleagues synthesized wafer-scale hBN epitaxial layers on sapphire substrates through MOCVD,<sup>236</sup> on the basis of which MSM photodetector arrays with a sharp cut-off wavelength of  $\sim 230$  nm were fabricated.<sup>237</sup> Feng *et al.* used PLD to grow nanostructured hBN and demonstrated UV detectors with an output power of  $\sim 2 \mu\text{W}$ .<sup>238–240</sup> Very recently, nanostructured hBN with an improved connection with substrates was synthesized by adding a flat 5 nm hBN buffer layer before PLD depositing.<sup>241</sup> Due to better hBN-substrates properties, UV detectors with high temperature endurance of up to 400 °C have been achieved. Although the potentials of hBN in UV-detection have been shown, the photoresponse properties of few-layer or even monolayer samples are rarely studied. This is probably due to two reasons: the first is that most of the so-far attentions about hBN have been paid on its role as passivation and dielectric layers for other 2DLMs because of its good stability and high dielectric breakdown strength. On the other hand, controlled growth and the transfer method of high-quality 2D hBN layers continue to be a big challenge, which becomes the main obstacle that limits the development of UV-detectors based on hBN.<sup>236,238,242–244</sup> Nevertheless, a number of emerging reports have studied the photodetection behavior of hBN layers on the basis of high-quality synthesis. For example, Wang *et al.* synthesized high-quality hBN domains by ion beam supporting deposition, based on which UV-detectors were fabricated.<sup>244</sup> Those devices showed low off-state current and a high on-state current to 190 nm light, giving a high on/off ratio of  $10^3$ . From the point view of synthesis, hBN films with thickness down to single layer have been achieved. For instance, Cun *et al.* recently reported the wafer-scale growth of h-BN with single orientation on Rh(111) substrates and subsequent high-quality transfer onto arbitrary substrates like  $\text{SiO}_2$ .<sup>242</sup>

As a natural hyperbolic material, hBN is sustainable with hyperbolic phonon-polaritons modes. Although this research area is more or less beyond the scope of photodetectors, this technology is very promising for applications beyond conventional optoelectronics, like nano-imaging. Hence, here we will give a short overview on this area related to hBN. Polaritons, referring to the collective excitations resulting from the coupling of photons with matter (like phonons, excitons, and plasmons), can sustain at the interface between materials with positive and negative permittivity.<sup>245</sup> With the feature of confinement of electromagnetic waves on a space much smaller than the wavelength, polaritons have been one of the focuses in nano-photonics. As one kind of polariton, phonon-polaritons (PPs) are collective oscillations originating from the coupling of photons with optical phonons. In hyperbolic materials like hBN, the permittivity tensor exhibits sign inversion between the in- and out-of-plane directions providing the possibility of polaritons (hyperbolic phonon-polaritons, HPPs). Specifically, hBN has two sets of infrared-active optical phonon modes denoted as upper and lower Reststrahlen bands.<sup>246</sup> Pioneering works done by Dai *et al.* and Caldwell *et al.* in 2014 have shown that hBN is sustainable for HPPs with low losses compared with polaritons based on InGaAs, graphene, and  $\text{SiO}_2$ .<sup>20,246</sup> Recently, Giles *et al.* synthesized isotopically pure hBN to decrease the

amount of point defect and increase the phonon lifetimes.<sup>247</sup> Through this method, the propagation length of HPPs in hBN can be enhanced three times reaching as high as 3.5  $\mu\text{m}$ . One promising application of HPPs is direct imaging of deeply subdiffractional sized objects.<sup>248</sup> Taking Li and his colleagues' work as an example, Au arrays underneath a hBN flake (150 nm in thickness) can be clearly identified with infrared scattering scanning near-field optical microscope (s-SNOM).<sup>249</sup>

### 3.6 Metal halides

Metal halides (MHs) in the form of  $\text{MH}_2$ , here  $\text{M} = \text{Mg}, \text{Ca}, \text{Zn}, \text{Cd}, \text{Ge},$  or  $\text{Pb}$ , and  $\text{H} = \text{Cl}, \text{Br},$  or  $\text{I}$ , are another group of 2DLMs. With a same stoichiometric ratio of 1:2 as with TMDs, MHs share a 1T  $\text{MoS}_2$  like structure as shown in Fig. 16a. Compared with its analogue of TMDs, the properties of MHs have been rarely studied so far. However, they began to cause attention very recently due to the synthesis of Pb-based MHs, which can be used as precursors to grow Pb-based organic-inorganic perovskites.<sup>250–252</sup> MHs themselves are semiconductors with bandgaps covering the visible to UV range. While decreasing down to monolayers, the response spectra modulate to a wider range. Fig. 16b shows Lu *et al.*'s work as an example.<sup>253</sup> According to the GGA calculation, the electric bandgaps of MHs monolayers range from 2.03 eV of  $\text{ZnI}_2$  to 6.08 eV of  $\text{MgCl}_2$ , and monolayer  $\text{MgCl}/\text{Br}_2$  are direct bandgap while the others are indirect. This predicts the potential application of MHs in UV and deep-UV photodetectors.

Until now, both solution and PVD methods have been used to synthesize 2D MHs flakes. However, considering the high water solubility of MHs, which greatly restricts the devices fabrication process, there are few experimental works on the photoresponse properties of 2D MHs. And most works adopted a shadow mask method to fabricate the devices. For instance,

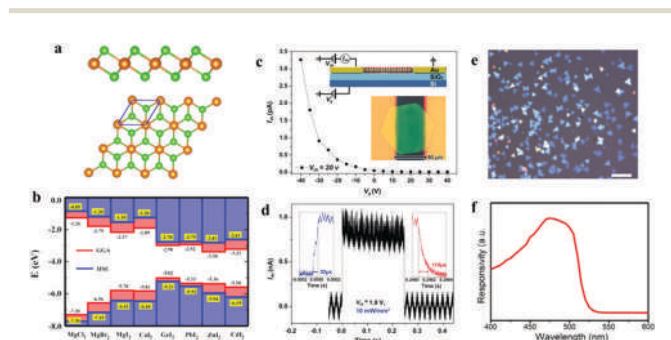


**Fig. 16** (a) Side view (top) and top view (bottom) of the MHs crystal structure. The unit cell is outlined by solid blue lines. (b) Band alignments of monolayer metal halogenides MHs. The "0" energy level is chosen as the vacuum level. For clarity, the absolute values of band edges are labeled. (c) Transfer characteristics of a few-layered  $\text{PbI}_2$  device. The inset shows the schematic diagram of the measurement system and an optical photograph of the device. (d) Time dependent response of the  $\text{PbI}_2$  device. Rise (e) optical image of the synthesized  $\text{PbI}_2$  flakes. And its spectrum response to 400–600 nm is shown in (f); (a) and (b) are reproduced from ref. 253 with permission from AIP Publishing LLC, Copyright 2016, (c) and (d) are reproduced from ref. 254 with permission from John Wiley & Sons, Inc., Copyright 2016, and (e) and (f) are reproduced from ref. 255 with permission from Elsevier B.V. and Science China Press, Copyright 2017.

Zheng *et al.* grew hexagonal  $\text{PbI}_2$  flakes through a facile solvent evaporation method.<sup>254</sup> Using  $\text{Pb}(\text{NO}_3)_2$  and  $\text{KI}_2$  aqueous solutions as sources,  $\text{PbI}_2$  with a thickness of tens of nanometers can be synthesized without any special requirements on the substrates. The as-obtained  $\text{PbI}_2$  mainly showed two Raman peaks located at  $\sim 76$  and  $96 \text{ cm}^{-1}$ , corresponding to the  $\text{E}_g$  and  $\text{A}_{1g}$  modes, respectively. In addition, a strong PL peak centered at 496 nm was observed at 80 K, demonstrating the high quality of the synthesized samples. The as-obtained  $\text{PbI}_2$  were found to show a weak p-type conduction with a fast response speed (55 and 110  $\mu\text{s}$  for the rise and decay process, respectively) to 450 nm light (Fig. 16c and d). On the other hand, Lan *et al.* grew  $\text{PbI}_2$  nanosheets through a PVD method and fabricated photodetectors with  $R$  of  $\sim 0.4 \text{ A W}^{-1}$  to 405 nm light.<sup>256</sup> Recently, monolayer  $\text{PbI}_2$  flakes with a triangle shape were synthesized by Wang *et al.*<sup>255</sup> The as-grown  $\text{PbI}_2$  flakes show obvious response to blue light with a peak at  $\sim 475$  nm light (Fig. 16e and f).

### 3.7 Transition metal chalcogenophosphates

Transition metal chalcogenophosphates (TMCPs) in the form of  $\text{MPX}_3$ , where  $\text{M} = \text{V}, \text{Cr}, \text{Mn}, \text{Fe}, \text{Co}, \text{Ni}, \text{Cu}, \text{Zn}, \text{Cd},$  and  $\text{X} = \text{S}, \text{Se},$  and  $\text{Te}$ , are an emerging 2DLMs group.<sup>257–260</sup> From the point of view of crystalline structure, the repeating layers inside TMCPs can be seen as a transformation from H-phase TMDs but with P atoms replacing the positions of transition metals in TMDs forming P–P dimers. The P–P dimers are covalently bonded with 6 neighboring S atoms forming  $[\text{P}_2\text{S}_6]$  units which are ionically connected by the interspersed M atoms.<sup>260</sup> Fig. 17a and b use  $\text{NiPS}_3$  as an example.<sup>261</sup> The atomic layers then can stack in the  $C2/m$  (for  $\text{MPS}_3$ ) or  $R3$  ( $\text{MPSe}_3$ ) space groups to construct the corresponding bulks.

Research on TMCPs dates back to 100 years ago but renewed interests very recently have been stimulated by big successes of other 2DLMs like G, TMDs, and so on. There are mainly three specialties that make this materials family very attractive compared with its analogues: the first is the large spanning bandgaps. For example, bulk  $\text{FePS}_3$ ,  $\text{NiPS}_3$ , and  $\text{FePSe}_3$  have bandgaps of 1.5, 1.7, and 1.3 eV, respectively, which covers the visible light range. On the other hand, bulk  $\text{MnPS}_3$ ,  $\text{CdPS}_3$ , and  $\text{ZnPS}_3$  have bandgaps of 3.0, 3.0, and 3.4, respectively, corresponding to the UV light range.<sup>257</sup> In addition, this wide-spectra coverage can be maintained while decreasing down to monolayers.<sup>263</sup> The second is that appropriate band positions of monolayers with band edges straddle the redox potentials of water, which makes them very appealing as photocatalysts for water splitting.<sup>260</sup> Finally, both theoretical and experimental works have predicted/demonstrated the existence of magnetic properties of some peculiar TMCPs monolayers (see Table 3), which makes them promising candidates for recently developed 2D magnetics.<sup>263,264</sup> As a "new" member of 2DLMs, studies on the 2D TMCPs are relative few, and theoretical works are ahead of experimental ones with most of the focus on basic properties explorations. Very recently, Chu *et al.* fabricated photodetectors based on CVD synthesized  $\text{NiPS}_3$  single flakes (Fig. 17c).<sup>262</sup> They found a  $\text{NiPS}_3$  flake (4.7 nm in thickness) had obvious response

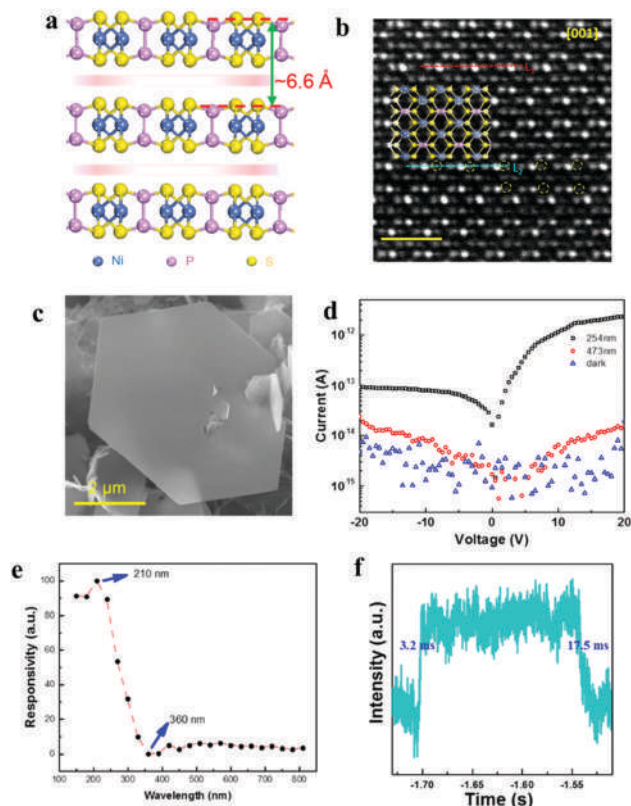


Fig. 17 (a) Schematic representation of NiPS<sub>3</sub> crystal structure from side view. (b) Atomic-level HAADF-STEM image of an ultrathin NiPS<sub>3</sub> nanosheet with the corresponding structural schematic. (c) SEM image of NiPS<sub>3</sub> nanosheets grown on carbon fibers. (d) Light response curve of the device under 254 and 473 nm light illuminations. (e) The wavelength- and dependent *R* of NiPS<sub>3</sub> device. (f) Time-dependent photocurrent of NiPS<sub>3</sub> device; (a) and (b) are reproduced from ref. 261 with permission from Elsevier Ltd, Copyright 2017 and (c)–(f) are reproduced from ref. 262 with permission from John Wiley & Sons, Inc., Copyright 2017.

to light with a wavelength smaller than 360 nm. In addition, the device showed *R* as high as 126 mA W<sup>-1</sup> and a fast response time of ~3.2 ms to 254 nm light (Fig. 17d–f). As with many other new 2DLMs, TMCPs are still at their early stage with many properties and applications yet to be explored. However, with the features mentioned above, their potentials are really worthwhile to look forward to.

### 3.8 Bi-Based oxychalcogenides

Bi-Based oxychalcogenides (BOCs), including Bi<sub>2</sub>O<sub>2</sub>S, Bi<sub>2</sub>O<sub>2</sub>Se, and Bi<sub>2</sub>O<sub>2</sub>Te, are new members that were recently rediscovered and joined the big 2DLMs family.<sup>6</sup> It should be noted that BOCs share a special 2DL structure: two neighboring covalently bonded [Bi<sub>2</sub>O<sub>2</sub>] layers are connected by one column of interfacial chalcogen anions (S<sup>2-</sup>, Se<sup>2-</sup>, or Te<sup>2-</sup>) through weak electrostatic interactions rather than the van der Waals forces in common 2DLMs.<sup>6,265,266</sup> Fig. 18a uses the structure of Bi<sub>2</sub>O<sub>2</sub>Se as an example. Hence, BOCs are actually quasi-2DLMs which are absent from van der Waals gaps. However, the weak electrostatic forces can also enable exfoliation from the planes of chalcogen anions layers but probably with atomic rearrangements at the

Table 3 Summary of the bandgaps and magnetic properties of selected TMCPs monolayers. Data were collected from ref. 263

Materials	<i>E<sub>g</sub></i> (eV)	Magnetic properties	Materials	<i>E<sub>g</sub></i> (eV)	Magnetic properties
V <sub>2</sub> P <sub>2</sub> X <sub>3</sub>	S 2.50	AFM	Co <sub>2</sub> P <sub>2</sub> X <sub>3</sub>	S 0	NM
	Se 2.10	AFM		Se 0	NM
	Te 1.57	NM		Te 0	NM
Cr <sub>2</sub> P <sub>2</sub> X <sub>3</sub>	S 0	FM	Ni <sub>2</sub> P <sub>2</sub> X <sub>3</sub>	S 2.83	AFM
	Se 0	FM		Se 2.22	AFM
	Te 0	FM		Te 0.27	NM
Mn <sub>2</sub> P <sub>2</sub> X <sub>3</sub>	S 3.05	AFM	Cu <sub>2</sub> P <sub>2</sub> X <sub>3</sub>	S 1.76	NM
	Se 2.24	AFM		Se 0.56	NM
	Te 1.06	NM		Te 0	NM
Fe <sub>2</sub> P <sub>2</sub> X <sub>3</sub>	S 2.07	AFM	Zn <sub>2</sub> P <sub>2</sub> X <sub>3</sub>	S 3.11	NM
	Se 1.48	NM		Se 2.19	NM
	Te 1.35	NM		Te 1.26	NM

FM, AFM, and NM: ferromagnetic, anti-ferromagnetic, and non-magnetic, respectively.

surfaces. In bulk states, Bi<sub>2</sub>O<sub>2</sub>S, Bi<sub>2</sub>O<sub>2</sub>Se, and Bi<sub>2</sub>O<sub>2</sub>Te are semiconductors with bandgaps of ~1.5, 0.85, and 0.23 eV, respectively.<sup>6,229,265</sup> This materials family has been attracting growing attention because of the outstanding electronic properties recently found in Bi<sub>2</sub>O<sub>2</sub>Se by Peng *et al.*<sup>6,229,267</sup> Through a van der Waals epitaxy method, they synthesized Bi<sub>2</sub>O<sub>2</sub>Se nanoflakes with thickness down to a monolayer for the first time. Two typical Raman peaks located at ~131 and 174 cm<sup>-1</sup> (corresponding to the E<sub>g</sub><sup>2</sup> and A<sub>1g</sub><sup>2</sup> modes, respectively) were observed. These as-synthesized Bi<sub>2</sub>O<sub>2</sub>Se were found to have an indirect bandgap of ~0.85 eV in bulk form, and this value gradually increased to ~1.9 eV as the thickness thinned to a monolayer (Fig. 18b and c).<sup>268</sup> The CBM located at the Γ point mainly consists of Bi p orbitals and disperses strongly along the Γ–X and Γ–M directions. More importantly, a small in-plane electron effective mass (0.14 ± 0.02*m*<sub>0</sub>) was predicted from the band structure, which finally leads to high intrinsic electron mobility. FETs based on Bi<sub>2</sub>O<sub>2</sub>Se have been demonstrated with remarkable performances at room temperature, including high mobility of ~450 cm<sup>2</sup> V<sup>-1</sup> s<sup>-1</sup>, large on/off ratios of 10<sup>6</sup>, and near-ideal SS of 65 mV dec<sup>-1</sup>, which is among the highest performances that have been achieved in 2DLMs.<sup>6</sup> At the same time, they also show the controllable synthesis of large-scale arrays of Bi<sub>2</sub>O<sub>2</sub>Se microplates (Fig. 18d).<sup>267</sup> All these results push Bi<sub>2</sub>O<sub>2</sub>Se to the very front edge of 2DLMs.

With these superiorities, interesting photoresponse properties of Bi<sub>2</sub>O<sub>2</sub>Se are anticipated. Recently, Li *et al.* reported their preliminary study. They fabricated photoconductors based on synthesized Bi<sub>2</sub>O<sub>2</sub>Se flakes and demonstrated a broadband response to 365–808 nm light. Without voltage gating, the response time and responsivity at 808 nm light reached up to 2.8 ms and 6.5 A W<sup>-1</sup>, respectively (Fig. 18d and f).<sup>269</sup> At the same time, the flexibility of the as-fabricated photoconductors was also exhibited. The performances of Bi<sub>2</sub>O<sub>2</sub>Se in Peng *et al.*'s work were extensively enhanced.<sup>270</sup> They found the *R* of Bi<sub>2</sub>O<sub>2</sub>Se can reach 10<sup>4</sup>–10<sup>-1</sup> A W<sup>-1</sup> covering an extremely wide spectrum



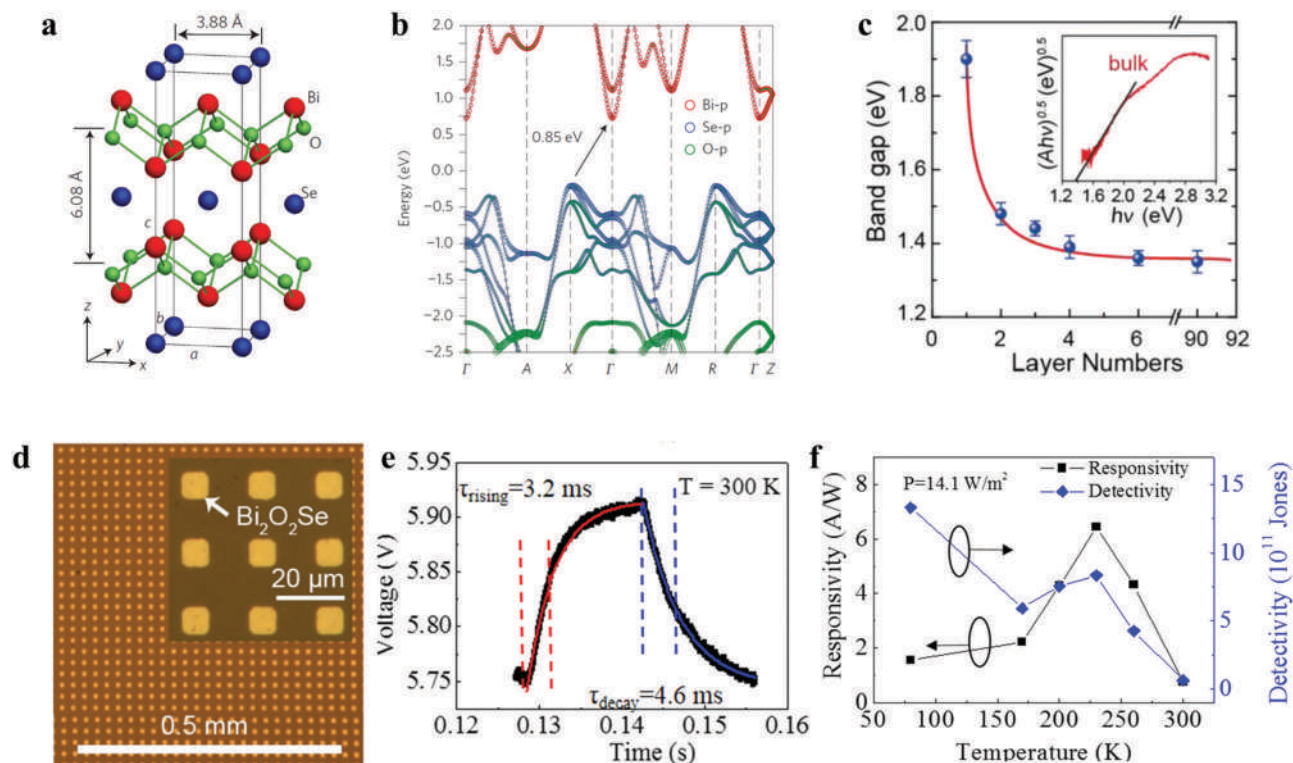


**Fig. 18** (a) Crystal structure of  $\text{Bi}_2\text{O}_2\text{Se}$ ; for clarity, the weak electrostatic interactions between Se and the  $[\text{Bi}_2\text{O}_2]$  layer are not presented. (b) Calculated band structure of  $\text{Bi}_2\text{O}_2\text{Se}$  with a bandgap of  $\sim 0.85$  eV. (c) Extracted optical band gaps as a function of layer number, and deduction of the band gap for bulk  $\text{Bi}_2\text{O}_2\text{Se}$  is shown in the inset. (d) Typical OM image of centimeter-scale 2D  $\text{Bi}_2\text{O}_2\text{Se}$  arrays fabricated with the help of photolithography. (e) Time dependent photoresponse of  $\text{Bi}_2\text{O}_2\text{Se}$  photodetector. (f) Temperature-dependent responsivity and detectivity of  $\text{Bi}_2\text{O}_2\text{Se}$  photodetector; (a) and (b) are reproduced from ref. 6 with permission from Macmillan Publishers Ltd, Copyright 2017, (c) is reproduced from ref. 268 with permission from American Chemical Society, Copyright 2017, (d) is reproduced from ref. 267 with permission from John Wiley & Sons, Inc. Copyright 2017, and (e) and (f) are reproduced from ref. 269 with permission from John Wiley & Sons, Inc., Copyright 2017.

range of  $\sim 500$ – $1550$  nm with a fast response speed of picoseconds. These parameters are also among the superb performances that have been achieved in 2DLMs. Up to now, the properties of  $\text{Bi}_2\text{O}_2\text{Se}$  and other BOCs still have been unclear due to their short history. However, considering the outstanding performances they have shown, it is very worthwhile expecting to see what this newcomer may bring.

## 4. Photodetectors based on 2D non-layered materials

Besides the layered materials with natural van der Waals gaps mentioned above, there are also many important semiconductors with three-dimensional isotropic crystal structures, such as III–V group (GaN, GaAs), II–VI group (ZnO, CdTe), and IV–VI group (PbS). Different from layered crystals, non-layered materials generally have bulk crystals formed *via* covalent bonding. As a result, lots of unsaturated dangling bonds will be formed on the surface of 2D non-layered structures, inducing a highly active surface. With a high optical absorption coefficient and direct band gaps, these traditional semiconductor materials have been widely used in optoelectronic devices. Inspired by the great success of 2D layered materials, more and more attention is

being paid to obtain artificial 2D thin layers from non-layered materials, which will not only greatly expand the scope of 2D materials, but also bring us exotic optoelectronic properties and heterostructure building blocks due to the strong 2D confinement effect of charge carriers, phonons, and photons. In a typical example, S. Ithurria *et al.* demonstrated that the absorption and emission spectra of 2D non-layered colloidal CdSe, CdS, and CdTe nanosheets strongly depend on their thickness.<sup>271</sup> Besides, the 2D planar structure also makes these materials more compatible with current film microfabrication techniques and flexible substrates. However, due to the 3D bonded structures, there is no intrinsic driving force for 2D anisotropic growth of non-layered structures. Although certain nanometer-thick non-layered materials, such as Te and Se,<sup>272,273</sup> have been fabricated by a liquid-phase exfoliation technique, their average lateral size was around 100 nm, which is not suitable for practical applications. Thus, most strategies for preparing 2D non-layered materials are based on a bottom-up method. In this section, we will give a brief review of photodetectors based on 2D nonlayered materials taking the synthesis method as a clue.

The most common strategy uses wet chemistry methods, which have been widely applied in high-throughput synthesis of 2D non-layered noble metals, metal chalcogenides, and metal oxides.<sup>274</sup> For example, Sun *et al.* reported a generalized

molecular self-assembly synthesis method to prepare various ultrathin 2D nanostructures of transition metal oxides, such as  $\text{TiO}_2$ ,  $\text{ZnO}$ ,  $\text{Co}_3\text{O}_4$ ,  $\text{WO}_3$ ,  $\text{Fe}_3\text{O}_4$ , and  $\text{MnO}_2$ .<sup>275</sup> The lateral sizes of  $\text{ZnO}$ ,  $\text{Co}_3\text{O}_4$ , and  $\text{WO}_3$  nanosheets could reach up to 1–10  $\mu\text{m}$  while maintaining a thin thickness around 1.6–5.2 nm. However, products fabricated by wet chemistry methods are always randomly distributed and easily aggregated, bringing huge challenges to device fabrication. A practicable method is depositing suspensions of ultrathin 2D metal oxide nanosheets by spin-coating techniques. Fig. 19a shows a flexible 2D nanosheet photodetector fabricated on a transparent polyethylene terephthalate (PET) substrate where single-layer graphene was designed as the back and counter electrode. By controlling the coating process, the thickness of the deposited 2D metal oxide layer is around 50 nm. With their wide bandgaps, these 2D metal oxide photodetectors exhibit good response to 325 nm ultraviolet light. As shown in Fig. 19b, by periodically switching on and off the 325 nm ultraviolet light, photodetectors display highly stable and reproducible photoresponse behavior. Although the spin-coating method shows great potential in photodetection applications, the crystalline quality of products is relatively poor and the optoelectronic properties of individual 2D single-crystalline layer can't be effectively studied.

A template-assisted synthesis method is considered as a feasible way to guide planar epitaxial growth of 2D materials. By introducing suitable organic surfactants or inorganic ions, the morphology of products can be effectively controlled. For example, Wang *et al.* demonstrated the synthesis of one to 2 nm-thick single-crystalline  $\text{ZnO}$  nanosheets by employing sodium dodecyl sulfate at the water–air interface as soft templates.<sup>276</sup> The sizes of these nanosheets can reach up to tens of micrometers. A corresponding schematic illustration and AFM images was displayed in Fig. 19c and d, respectively. However, due to the specific bonding between  $\text{Zn}^{2+}$  ions and sulfate groups, the surfactants are difficult to remove from the surfaces of nanosheets, thus impacting their optoelectronic performance.

2D layered material provides a natural template to prepare certain 2D non-layered structures under solid-state conditions. For example, Feng *et al.* demonstrated the synthesis of 2D single-crystalline non-layered  $\text{CuGaSe}_2$  nanosheets by a templated solid-state reaction from  $\text{GaSe}$  nanosheets.<sup>278</sup> In brief, 50 nm thick copper was deposited on the surface of 2D  $\text{GaSe}$  thin layers (obtained by mechanical exfoliation) by thermal evaporation. After annealing in a tube furnace and removing the residual Cu with 3 M aqueous  $\text{FeCl}_3$ , 2D non-layered  $\text{CuGaSe}_2$  nanosheets were obtained and share the same morphology with  $\text{GaSe}$ . Correspondingly, the PL peak value takes a blue shift from 2.05 eV ( $\text{GaSe}$ ) to 1.71 eV ( $\text{CuGaSe}_2$ ). The fabricated photodetectors exhibit a sensitive photoresponse from a UV to visible spectrum. Under 490 nm laser illumination, the photoresponsivity and approximate detectivity are as high as  $10^2 \text{ A W}^{-1}$  and  $10^{12}$  Jones, respectively. Similarly, a 2D polycrystalline non-layered  $\text{Ga}_2\text{O}_3$  nanosheet, which is an important wide bandgap semiconductor ( $E_g$ : 4.9 eV), was synthesized by directly oxidizing a 2D  $\text{GaSe}$  thin layer in air

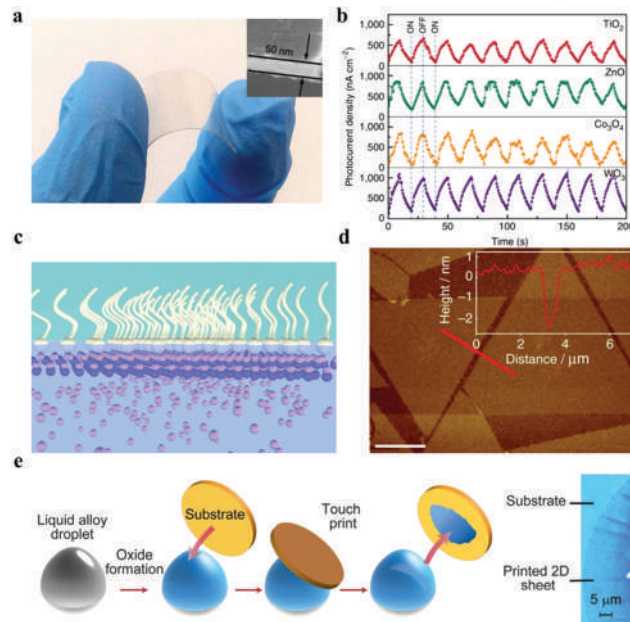


Fig. 19 (a) Optical image of a fabricated flexible 2D nanosheet photodetector. Inset: The SEM cross-section image. (b) Photoresponse behaviors of various 2D metal oxide photodetectors under periodically switching on and off the 325 nm ultraviolet light. (c) Schematic illustration of the epitaxial growth of 2D  $\text{ZnO}$  nanosheets directed by a surfactant monolayer. (d) AFM image of typical  $\text{ZnO}$  nanosheets on a Si substrate. Scale bar, 5  $\mu\text{m}$ . (e) Schematic illustration of the van der Waals exfoliation technique. An optical image of exfoliated 2D metal oxide nanosheet is displayed at the right; (a and b) are reproduced from ref. 275 with permission from Macmillan Publishers Ltd, Copyright 2014, (c and d) are reproduced from ref. 276 with permission from Macmillan Publishers Ltd, Copyright 2016 and (e) is reproduced from ref. 277, with permission from AAAS, Copyright 2017.

and it showed a sensitive and fast photoresponse to 254 nm ultraviolet light.<sup>279</sup> The photoresponsivity and approximate detectivity of this photodetector are  $3 \text{ A W}^{-1}$  and  $10^{12}$  Jones, respectively.

Recently, Zavabeti *et al.* proposed that gallium-based eutectic alloys can be utilized as a reaction solvent to produce ultrathin 2D polycrystalline metal oxide nanosheets at room temperature.<sup>277</sup> As shown in Fig. 19e, by adding appropriate metal (Hf, Al, and Gd) which has a lower Gibbs free energy for oxide formation than Ga, corresponding metal oxides ( $\text{HfO}_2$ ,  $\text{Al}_2\text{O}_3$ , and  $\text{Gd}_2\text{O}_3$ ) will form on the surface of a liquid metal droplet and can be transferred onto specific solid substrates using a van der Waals exfoliation method. In addition, they also developed a gas injection method for high-yield production of 2D oxide suspensions.

All the above products either own a polycrystalline structure or contain residual surfactants/impurity atoms, which are inevitable due to the strong interaction between the products and templates/surfactant agents. Besides, considering the general lattice mismatch problem and high surface energy of 2D non-layered materials, developing a new technology which can guarantee the 2D anisotropic crystal growth of non-layered materials in a highly passivated synthesis environment is needed. One of the strategies is van der Waals epitaxy (vdWE),

which is based on relatively weak van der Waals interactions between the epitaxial layer and substrates.<sup>280–283</sup> To prepare 2D non-layered crystals by vdWE, two conditions need to be satisfied:<sup>282</sup> (1) the 2D anisotropic growth of non-layered materials can be activated through modulating growth parameters, such as temperature and pressure; (2) the substrates should have a passivated atomically flat surface without dangling-bonds, such as mica and 2DLMs like graphene. Thus, lattice matching is not strictly required during vdWE growth, which is totally different from traditional epitaxial methods. In addition, this weak interaction makes it easy to release and transfer the epilayers onto other substrates. Many 2D single-crystalline non-layered materials have been successfully synthesized by a vdWE method, including elemental semiconductors (Te), binary (PbS and CdS), and ternary semiconductors ( $\text{Pb}_{1-x}\text{Sn}_x\text{Se}$ ).<sup>281,282,284,285</sup> With a large planar structure and high crystalline quality, these epitaxial nanosheets are very suitable for fabricating optoelectronic devices like photodetectors.

Cadmium chalcogenides, CdX (X = S, Se, Te), are important visible light-absorbing materials, which have been widely used in optoelectronic devices, such as solar cells, photodetectors, and light emitting diodes. For example, Zhao *et al.* reported that single-crystalline CdTe solar cells exhibit a high open-circuit voltage of up to 1.096 V and high power conversion efficiency of 17%.<sup>288</sup> So, the synthesis of 2D cadmium chalcogenide

nanosheets is highly desired. CdX has two different crystal structures, wurtzite and zinc-blende structures, both of which are three-dimensional and covalent bonded. Taking advantage of van der Waals epitaxy, the planar anisotropic growth of CdX has been realized.

Fig. 20a displays the typical wurtzite structure of CdX using CdTe as an example. Zheng *et al.* reported 2D anisotropic growth of CdS on the surface of monolayer  $\text{MoS}_2$  and studied the optoelectronic properties of CdS/ $\text{MoS}_2$  heterostructures.<sup>285</sup> Fig. 20b shows the SEM image of the epitaxial CdS nanosheets. Their lateral size and thickness are mainly distributed in 1–3  $\mu\text{m}$  and 10–60 nm, respectively. Compared with a monolayer  $\text{MoS}_2$  nanosheet, the heterostructure shows a broader spectral response and larger photoresponsivity. To study the optoelectronic properties of an individual CdX nanosheet, Zhu *et al.* demonstrated the synthesis of 2D CdSe nanosheets, with an average lateral size of several microns and thickness of 60 nm, on insulating layered mica substrates.<sup>289</sup> On the basis of that, they also *in situ* fabricated two-terminal 2D CdSe photodetectors. The photodetector showed a high photoresponsivity of  $500 \text{ A W}^{-1}$  and high EQE of  $1.4 \times 10^3$  under 450 nm laser illumination.

Recently, Cheng and his colleagues reported the preparation of nanometer-thick 2D CdTe nanosheets.<sup>286</sup> Fig. 20c and d display typical optical and AFM images of epitaxial CdTe

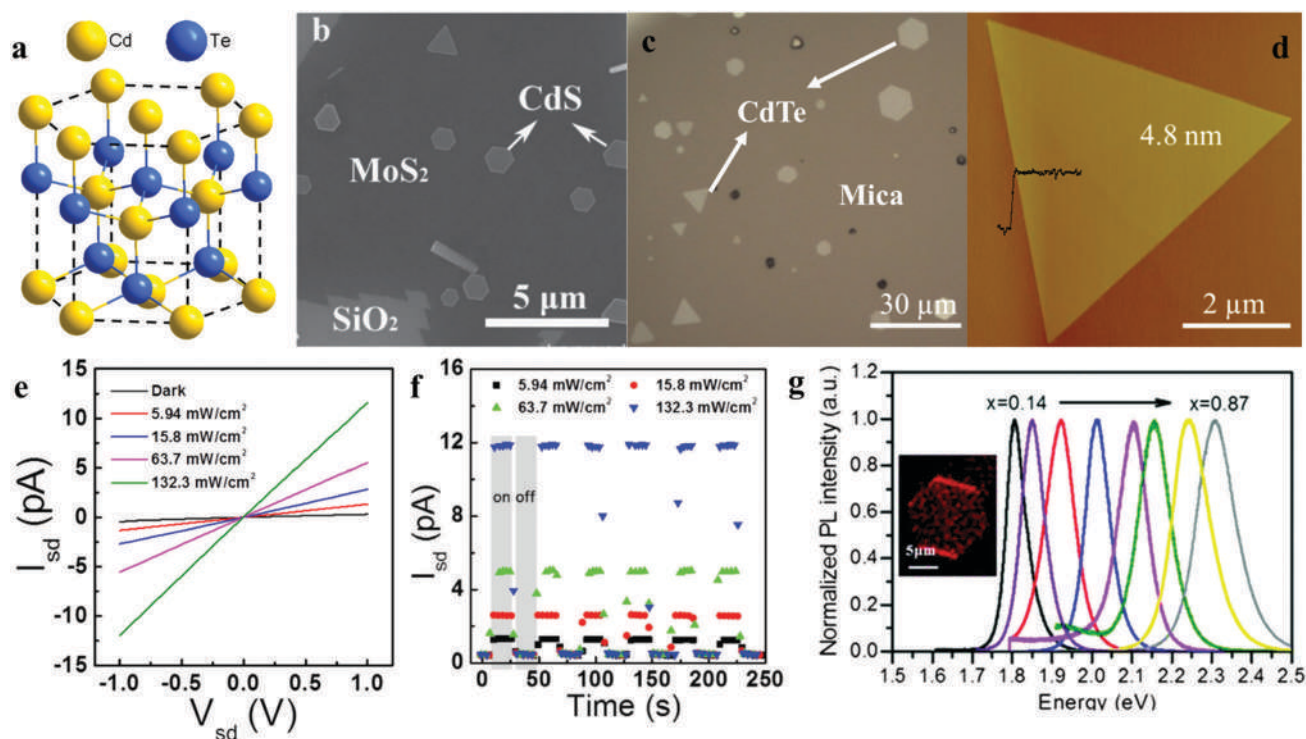


**Fig. 20** (a) Schematic illustration of CdX (X = S, Se, Te) with a wurtzite structure using CdTe as an example. (b) SEM image of epitaxial CdS nanosheets on a monolayer  $\text{MoS}_2$ . (c) Optical image of epitaxial CdTe nanosheets on a mica substrate. (d) AFM image of a typical CdTe nanosheet with thickness of 4.8 nm. (e and f)  $I_{\text{sd}}-V_{\text{sd}}$  output curves and time-dependent photoresponse of 2D CdTe photodetector under 473 nm laser illumination. (g) Normalized PL spectra of  $\text{CdS}_x\text{Se}_{1-x}$  alloy nanosheets with different compositions; (a and c–f) are reproduced from ref. 286 with permission from John Wiley & Sons, Inc., Copyright 2017, (b) is reproduced from ref. 285 with permission from John Wiley & Sons, Inc., Copyright 2016, and (g) is reproduced from ref. 287 with permission from the Royal Society of Chemistry, Copyright 2017.



nanosheets on a mica substrate, respectively. Lateral size and thickness are mainly distributed in 5–11  $\mu\text{m}$  and 5–10 nm, indicating that the planar preparation of nanometer-thick non-layered structures can be realized in a low-cost CVD system. Fig. 20e and f show the  $I_{\text{DS}}-V_{\text{DS}}$  (drain current–voltage bias) output curves and time-dependent photoresponse of a 2D CdTe photodetector under 473 nm laser illumination, which exhibited ultralow dark current ( $\sim 100$  fA under 1 V bias) and high photoswitching ratio ( $\sim 27$ ). Lower dark current (less than 10 fA under 2 V bias) and higher photoswitching ratio ( $\sim 10^4$ ) can be obtained when the temperature goes down to 80 K. Although the photodetectors based on CdSe and CdTe nanosheets exhibit distinct dark current and photoswitching ratios due to their different thicknesses, they both present a similar photoresponse time of  $\sim 20$  ms. Furthermore, FETs based on transferred CdTe nanosheets exhibit stable photoresponses and p-type conduction behavior with an on/off ratio over two orders, indicating its high compatibility with the current Si-based electronic techniques. Besides these binary materials, a band engineering based on 2D  $\text{CdS}_x\text{Se}_{1-x}$  alloys was also reported.<sup>287</sup> As shown in Fig. 20g, with increasing S content ( $x$ ), the alloy shows a tunable PL peak energy varying from 1.8 eV to 2.3 eV. This composition-dependent band gap provides large tunability for their practical applications. Moreover, having a similar crystal structure to CdX, zinc chalcogenides ( $\text{ZnX}$ , X = S, Se, Te) should also be noted.

Pb-Based semiconductors like PbS,  $\text{Pb}_{1-x}\text{Sn}_x\text{Se}$ , and  $\text{Pb}_{1-x}\text{Sn}_x\text{Te}$  have received great attention due to their direct narrow bandgaps (0.4 eV for PbS for example) which makes them promising candidates for IR detection. These materials share a cubic structure as shown in Fig. 21a, making the synthesis of their 2D nanomaterials very difficult. Stimulated by the research on 2DLMs, various strategies have been proposed to achieve the 2D morphology. The 2D anisotropic growth for ultrathin PbS sheets was first reported by Weller and coworkers.<sup>291</sup> Using oleic acid ligands to cap the facets of PbS, ultrathin single-crystal PbS with lateral size at micrometer scale and thickness of 2.2 nm were synthesized. Benefiting from missing in-plane ligands, the photon-triggered on/off ratio was over 100 with a power intensity of  $2.0 \text{ mW cm}^{-2}$ , and the rise time was about 0.032 s. However, the carrier injection was still restrained owing to ligands in the vertical direction. In total, the PbS nanosheets showed a moderate photoresponse with a responsivity of  $0.472 \text{ A W}^{-1}$ . vdWE was also used to synthesize this material family, including  $\text{Pb}_{1-x}\text{Sn}_x\text{Se}$  and PbS.<sup>282,284</sup> For instance, using graphene as a van der Waals buffer layer, PbS nanoplates with a minimum thickness of less than 10 nm were synthesized (Fig. 21b). A step further, orientation-controlled single-crystalline PbS nanoplates arrays have been realized using mica as substrates (Fig. 21c and d).<sup>284</sup> Compared with random distributed nanosheets obtained by a solution method, van der Waals epitaxial nanoplates arrays possess great superiority for integrated optoelectronic circuits. In addition, photodetectors based on as-obtained PbS arrays showed an obvious infrared photoresponse with high sensitivity to lasers with wavelengths of 800, 1064, and 1340 nm, respectively as shown in Fig. 21g.

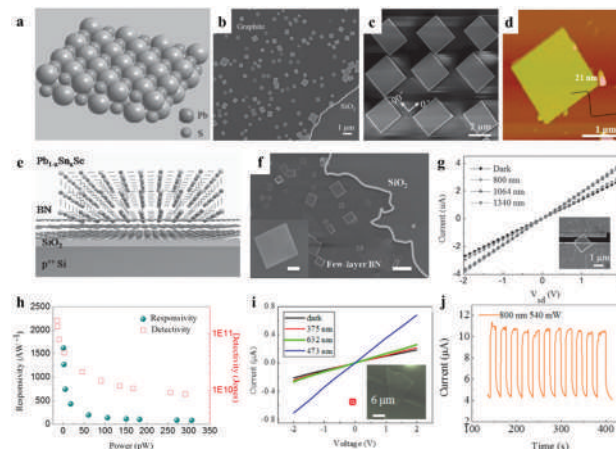


Fig. 21 (a) Schematic illustration of PbS with a cubic structure. (b) SEM image of epitaxial PbS nanosheets on graphite. (c) SEM image of a  $3 \times 3$  PbS array. (d) AFM image of a typical  $\text{Pb}_{1-x}\text{Sn}_x\text{Se}$  nanosheet with thickness of 21 nm. (e) Schematic illustration of the epitaxial growth of 2D  $\text{Pb}_{1-x}\text{Sn}_x\text{Se}$  nanosheets on a  $\text{SiO}_2/\text{Si}$  substrate by designing a BN buffer layer. (f) SEM image of epitaxial  $\text{Pb}_{1-x}\text{Sn}_x\text{Se}$  nanosheets on few-layer BN. (g) Photoresponse behavior of a single PbS nanosheet with irradiation of 800, 1064, and 1340 nm laser, respectively. (h) Plots of responsivity and detectivity of a PbS nanosheet versus laser power. (i)  $I_{\text{DS}}-V_{\text{DS}}$  curves of a single  $\text{Pb}_{1-x}\text{Sn}_x\text{Se}$  nanosheet photodetector in the dark and in the presence of 375, 473, and 632 nm laser, respectively. (j) Time-dependent photoresponse of  $\text{Pb}_{1-x}\text{Sn}_x\text{Se}$  nanosheet photodetector with laser wavelength of 800 nm; (a–c, g and h) are reproduced from ref. 284 with permission from John Wiley & Sons, Inc., Copyright 2016, (d, i and j) are reproduced from ref. 282 with permission from American Chemical Society, Copyright 2015, and (e and f) are reproduced from ref. 290 with permission from John Wiley & Sons, Inc., Copyright 2015.

The responsivity, detectivity and response time could reach  $1621 \text{ A W}^{-1}$ ,  $1.72 \times 10^{11}$  Jones and 0.3 s, respectively (Fig. 21g and h).

2D  $\text{Pb}_{1-x}\text{Sn}_x\text{Se}$  nanoplates with thickness ranging from 15 to 45 nm were also synthesized by vdWE, based on which bendable photodetectors on a flexible substrate were demonstrated.<sup>282</sup> The  $\text{Pb}_{1-x}\text{Sn}_x\text{Se}$  photodetector showed a wide-spectra response to UV-IR light with a highest responsivity and response time of  $5.95 \text{ A W}^{-1}$  and 0.90 s, respectively (Fig. 21i and j). In addition, by using BN as a van der Waals buffer layer, 2D  $\text{Pb}_{1-x}\text{Sn}_x\text{Se}$  nanosheets could be even synthesized on  $\text{SiO}_2$  substrates (Fig. 21e and f), which exhibit great potential for integration with Si-based optoelectronic circuits.<sup>290</sup> These as-obtained devices showed sensitive infrared photoresponse with a photon-triggered on/off ratio of 82.5 and responsivity of  $0.19 \text{ A W}^{-1}$ .

III–V semiconductors, including GaAs, GaN, and InP, have a variety of specialties, such as direct bandgaps covering the visible light range, tunable compositions, and high mobility, making them the heart of a wider range of modern electronic and optoelectronic devices. As a result, 2D nanostructured III–V semiconductors have been always the focus of the 2D materials research community. As research progressed, there have been a few strategies that can bring III–V semiconductors into 2D geography. For instance, Kim *et al.* demonstrated the wafer-scale vdWE growth of high-quality single-crystalline GaN films on a graphene/SiC substrate by a modified two-step growth.<sup>283</sup>

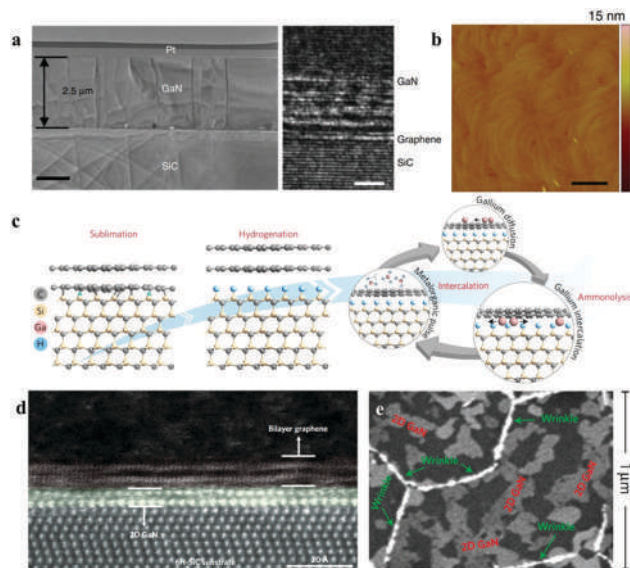


Fig. 22 (a) Low-magnification (left) and high-resolution (right) cross-sectional TEM image of GaN/G/SiC system. The scale bar of left and right are 1  $\mu\text{m}$  and 2 nm, respectively. (b) AFM image of GaN films grown by van der Waals epitaxy. Scale bar, 1  $\mu\text{m}$ . (c) Schematic illustration of the synthesis of 2D GaN via the migration-enhanced encapsulated growth (MEEG) technique. (d) STEM cross-section image of 2D GaN composed of two gallium sub-layers. (e) SEM image of 2D GaN concentrated near networks of graphene wrinkles; (a) and (b) are reproduced from ref. 283 with permission from Macmillan Publishers Ltd, Copyright 2014, and (c–e) are reproduced from ref. 292 with permission from Macmillan Publishers Ltd, Copyright 2016.

Fig. 22a shows the low-magnification (left) and high-resolution (right) cross-sectional TEM images of GaN/graphene/SiC which exhibits well aligned and ordered crystal lattices. The products have a low dislocation density of  $\sim 1 \times 10^9 \text{ cm}^{-2}$ , which is comparable with that obtained from conventional epitaxial methods. AFM was applied to investigate their surface morphologies. As shown in Fig. 22b, the epitaxial GaN film shows an atomistically smooth surface with a small root mean square (RMS) roughness of 3 Å. With the aid of a Ni stressor and thermally released tape, GaN films can be released and transferred onto arbitrary substrates. And LEDs with emission at 440 nm were fabricated on the basis of the as-fabricated GaN.

Although research on thin film single-crystalline III–V materials has achieved great success, obtaining nanometer-thick III–V nanosheets still remains a great challenge. Through a migration-enhanced encapsulated growth (MEEG) technique, Balushi *et al.* demonstrated the synthesis of atomically thin 2D GaN on the SiC substrates.<sup>292</sup> As shown in Fig. 22c, by using bilayer graphene as a capping layer, gallium atoms generated by decomposing trimethylgallium can diffuse onto the surface of graphene and intercalate into the highly passivated SiC/graphene interface facilitated by point defects and wrinkles in the graphene. As a result, the intercalated gallium atoms are stabilized and can transform into 2D GaN *via* ammonolysis. Fig. 22d displays the STEM cross-section image of a 2D GaN composed of two gallium sub-layers, indicating that the 2D planar growth of GaN was realized at the interface of graphene and SiC. It should be noted

that the products are not in 1:1 stoichiometry and exhibit covalent bonding to the SiC substrate while preserving a vdW gap with the graphene capping layer. Fig. 22e shows a SEM image of 2D GaN layers with lateral sizes of several hundred nanometers. Compared to bulk GaN ( $E_g$ : 3.42 eV), 2D GaN still retains a direct band gap but exhibits a larger gap value of  $\sim 5$  eV due to a strong quantum confinement.

Organic–inorganic hybrid perovskite, which can be described by the formula  $\text{CH}_3\text{NH}_3\text{PbX}_3$  ( $X = \text{Cl}, \text{Br}, \text{and I}$ ), is another important non-layered material system. With optimal bandgap, high optical absorption coefficient, and ultra-long carrier diffusion length, these perovskite materials are expected to exhibit superior photodetection properties in their two-dimensional scenarios. Xiong *et al.* reported the synthesis of a high-quality 2D lead halide perovskite family with lateral sizes of 5–30  $\mu\text{m}$  and thicknesses from several atomic layers to several hundred nanometers.<sup>293</sup> Briefly, layered lead halide nanosheets ( $\text{PbCl}_2$ ,  $\text{PbBr}_2$ , and  $\text{PbI}_2$ ) were first grown on a mica substrate *via* vdWE. And then, the as-grown nanosheets were converted to perovskites *via* a gas–solid hetero-phase reaction. Bao *et al.* demonstrated the preparation of 2D single-unit-cell lead halide perovskite with a thickness of  $\sim 1.3$  nm.<sup>294</sup> Under the illumination of 405 and 532 nm lasers, the fabricated ultrathin photodetector exhibits high responsivities of 22 and 12  $\text{A W}^{-1}$ , respectively. Note that, besides these non-layered perovskite materials, some naturally layered perovskite crystals, such as  $(\text{C}_4\text{H}_9\text{NH}_3)_2\text{PbX}_4$  and  $\text{CsPbX}_3$  ( $X = \text{Cl}, \text{Br}, \text{and I}$ ), are also attracting people's attention.<sup>295–298</sup> P. D. Yang, A. G. Dong, and H. B. Zeng's groups reported the synthesis of  $(\text{C}_4\text{H}_9\text{NH}_3)_2\text{PbBr}_4$  and  $\text{CsPbBr}_3$  nanosheets with a thickness down to few monolayers *via* a simple solution-phase method.<sup>295–297</sup> Solution-processed 2D  $\text{CsPbBr}_3$  photodetectors exhibit a high photoswitching ratio and fast response time. In addition, by introducing an interdigital graphene electrode, Peng *et al.* demonstrated the photodetection properties of an individual 2D  $(\text{C}_4\text{H}_9\text{NH}_3)_2\text{PbBr}_4$  nanosheet, which showed low dark current, high photoswitching ratio, and ultrahigh responsivity up to  $\sim 2100 \text{ A W}^{-1}$ .<sup>298</sup>

## 5. Photodiodes/hybrid phototransistors based on heterostructures

As discussed in previous sections, photodetectors based on 2D materials beyond G and TMDs have exhibited novel phenomena and achieved many high performances.<sup>7,299,300</sup> However, device optimizations to further enhance light absorption, decrease dark current, and increase photocurrent are still needed. As one of several promising strategies, heterostructure engineering with atomically sharp interfaces offers great opportunities to modulate optoelectronic properties. Various 2D–2D van der Waals heterostructures have been extensively investigated,<sup>13</sup> while other mixed-dimensional (2D– $n$ D, where  $n$  is 0, 1, 3) heterostructures are attracting growing attention.<sup>301</sup> Particularly, photodiodes and hybrid phototransistors based on these heterostructures have been realized with different structures and principles. Performances of some representative devices are

summarized in Table 4. In this section, we will review achievements involving photodiodes/hybrid phototransistors based on 2D materials beyond graphene and TMDs.

### 5.1 Photodiodes

Photodetectors working under a photovoltaic mechanism are generally called photodiodes.<sup>31</sup> Typically, photodiodes are composed of p–n junctions formed between two semiconductors with different major carrier types, or Schottky barrier contacts between metals and semiconductors with different work functions. Because of the built-in electric field, a photodiode generally displays a rectifying characteristic and mainly two modes can be adopted for photodetection. In the photovoltaic mode, the photodiode is usually reversely biased (the external electric field direction is same with the built-in electric field) enhancing extraction capability of photo-generated carriers, inducing a lower dark current, higher detectivity, and faster response speed. On the other hand, in the photoconductive mode, the photodiode is forwardly biased (the external electric field has the opposite direction to the built-in one), leading to a high gain. Notably, a photodiode can also work without applying any external voltage bias due to the existence of built-in potential, which has been named as the so-called self-driven mode. In this mode, the device is considerably energy-efficient because of theoretical zero power consumption. This feature is much more intriguing for photodiodes based on 2DLMs considering their ultrathin nature which brings the device a complete depletion region and the absence of lattice match requirement.<sup>322–325</sup>

As previously discussed, BP, which is featured with wide coverage of bandgaps and high mobility, has been a promising candidate for wide-spectra photodetections.<sup>34,68,71,87,88,326–328</sup> Recently, several photodiodes based on BP have been studied.<sup>80,302–304</sup> Deng *et al.* demonstrated a p–n photodiode by attaching a 11 nm thick BP on a MoS<sub>2</sub> monolayer by van der Waals interaction, as shown in Fig. 23a.<sup>302</sup> Fig. 23b shows that responsivity reaches 1.27 mA W<sup>-1</sup> and 11 mA W<sup>-1</sup> for forward and reverse bias, respectively. Its maximum responsivity could be up to 418 mA W<sup>-1</sup> at a reverse bias of -2 V, which is nearly 100 times larger than that of a pristine BP phototransistor.<sup>71</sup> In addition, the device also shows an ability for photovoltaic energy conversion with an external quantum efficiency of 0.3%, as shown in Fig. 23c. Similarly, Ye *et al.* constructed a BP–MoS<sub>2</sub> (22 nm thick/12 nm thick) p–n photodiode and investigated the photodetection properties from visible to near-infrared range.<sup>304</sup> The devices worked at a forward bias condition in a photoconductive mode, which brings up large photoresponsivity. In detail, the photoresponsivity of the device is about 22.3 A W<sup>-1</sup> and 153.4 mA W<sup>-1</sup> at  $\lambda = 532$  nm and 1.55  $\mu\text{m}$ , respectively, with a response time of  $\sim 15$   $\mu\text{s}$ . They further designed a n–p–n bipolar junction transistor formed by a multilayer n-type MoS<sub>2</sub>/p-type BP/slightly n-type WSe<sub>2</sub>.<sup>80</sup> Here, BP is the base because of its high mobility and narrow bandgap, MoS<sub>2</sub> is the emitter injecting a large number of electrons into the base region, and lightly n-doped WSe<sub>2</sub> is used as the collector. Based on the amplification function of the bipolar junction transistor, the responsivities

reach up to 6.32 A W<sup>-1</sup> at 532 nm light and 1.12 A W<sup>-1</sup> at 1.55  $\mu\text{m}$ , respectively, both of which are by tens of times higher than that of WSe<sub>2</sub>–BP.

In- and Ga-based MMCs, such as InSe, GaSe, and GaTe, have also shown great potentials for high-performance electronic and optoelectronic applications.<sup>135,139,148,299</sup> Based on them, Yan *et al.* recently fabricated a p-GaSe/n-InSe (19 nm thickness/12 nm thickness) photodiode with a type II band alignment; meanwhile, graphene was used as the contact electrode.<sup>306</sup> More importantly, the devices demonstrated self-driven ability with low energy consumption. Attributed to the type II band alignment, low contact resistance, and suitable band alignment, the photodiodes working at zero or reverse bias displayed fast response speed ( $\sim 2$   $\mu\text{s}$ ), high detectivity ( $2.2 \times 10^{12}$  Jones), and great potential for broad spectral photodetections. Similarly, Yang *et al.* realized a self-driven photodiode based on a few-layer p-type GaTe and few-layer n-type MoS<sub>2</sub>.<sup>312</sup> At zero bias, the photoresponsivity, response time, and EQE of the devices were measured to be 1.36 A W<sup>-1</sup>, <10 ms and 266%, respectively. The energy-efficient photodiode was also demonstrated in a p-type GaTe/n-type InSe heterojunction. Under 405 nm light, the device showed self-driven photodetection with *R*, EQE, and response time of 12.8 mA W<sup>-1</sup>, 4.2%, and 20  $\mu\text{s}$ , respectively.<sup>329</sup> Wang *et al.* reported a photodiode based on a p-type GaTe/n-type MoS<sub>2</sub> (14 nm/5.5 nm thickness) with strong temperature and gate-tunable optoelectronic behaviors.<sup>311</sup> By optimizing the parameters, including the temperature, gate voltages, and incident light power, a high-performance photodetector was demonstrated. The photoresponsivity, EQE, response time, and detectivity reached up to 21.83 A W<sup>-1</sup>, 61.68%, 7 ms, and  $8.4 \times 10^{13}$  Jones, respectively.

The photodiodes mentioned above<sup>306,311,312</sup> are all based on 2D materials made by a mechanically exfoliation method. Chemical vapor deposition (CVD) is a powerful tool to massively grow 2D materials and their vertical/lateral heterostructures, such as graphene/h-BN,<sup>330</sup> MoS<sub>2</sub>/MoSe<sub>2</sub>,<sup>331</sup> WS<sub>2</sub>/WSe<sub>2</sub>,<sup>331</sup> and WS<sub>2</sub>/MoS<sub>2</sub>.<sup>332</sup> However, heterostructures based on these new 2DLMs are still limited. Li *et al.* realized a vertical stacked GaSe/MoSe<sub>2</sub> (monolayer/monolayer) heterostructure with a large lattice mismatch (13%) by a two-step CVD process using a van der Waals epitaxial growth mechanism.<sup>18</sup> The device structure, rectifying behavior, and photovoltaic effect are shown in Fig. 23d–f. Photon-to-electron conversion efficiency, fill factor, and photoresponsivity of the device (at zero bias and gate voltage 60 V) were estimated to be 0.3%, 0.43, and 25.3 mA W<sup>-1</sup>, respectively.

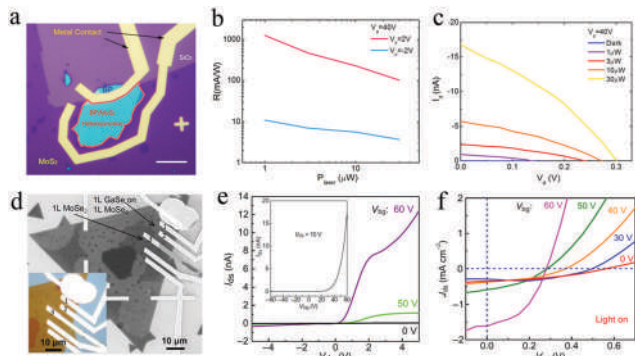
In addition to 2D–2D vdWHs, GaSe was also used to form a 2D–3D photodiode. Yuan *et al.* developed a wafer-scale few-layer GaSe/n-Si photodiode array using a molecular beam epitaxy.<sup>310</sup> Transparent indium-tin oxide arrays were deposited on the top of GaSe as anode electrodes. Under the illumination of a laser (532 nm) and at a zero bias, EQE and response speed of the photodiode achieved 23.6% and 60  $\mu\text{s}$ , respectively. Importantly, their devices show high stability *i.e.*, no performance degradation after 1 million cycles of operation. Based on the above research, researchers from the same group fabricated a 2 inch few layer GaTe<sub>x</sub>Se<sub>1-x</sub>/n-Si photodiode array by molecular



Table 4 Performance of photodetectors based on 2D heterostructures

2D materials beyond graphene and TMDs	Heterostructure	Performance					Operation voltages (V)	Ref.	
		Spectral range	Responsivity ( $A W^{-1}$ )	EQE (%)	Response time (s)	Detectivity (Jones)			
Elementals	BP	FL BP/1L MoS <sub>2</sub>	3.54	0.3%	—	—	$V_{DS} = 2; V_{GS} = 40$	302	
		FL BP/FL MoS <sub>2</sub>	0.17	—	—	—	$V_{DS} = -2; V_{GS} = 0$	303	
		FL BP/FL MoS <sub>2</sub>	22.3	—	$1.5 \times 10^{-5}$	$3.1 \times 10^{11}$	$V_{DS} = 3$	304	
		ML BP/1L Gr	$3.3 \times 10^3$	—	—	—	$V_{DS} = 1; V_{GS} = 0$	101	
		ML WSe <sub>2</sub> /ML BP/ML MoS <sub>2</sub>	6.32	—	—	$1.25 \times 10^{11}$	$V_{DS} = 3$	80	
Group III–VI MMCs	InSe	FL BP/MoS <sub>2</sub> NPs	5000	$1.2 \times 10^8$	0.02	$1.6 \times 10^{10}$	$V_{DS} = 0.1; V_{GS} = 0$	305	
		Gr/ML InSe/Gr	$\sim 10^5$	$10^7$	$10^{-3}$	$10^{13}$	$V_{DS} = 2; V_{GS} = 0$	156	
		FL InSe/FL GaSe	$2.1 \times 10^{-2}$	9.3	$2 \times 10^{-6}$	$2.2 \times 10^{12}$	$V_{DS} = 0$	306	
		ML InSe/1L Gr	940	$2.1 \times 10^5$	—	—	$V_{DS} = -0.05; V_{GS} = 0$	307	
		1L GaSe/1L MoSe <sub>2</sub>	$5.5 \times 10^{-3}$	—	—	—	$V_{DS} = 0; V_{GS} = 0$	308	
	GaSe	GaSe/Gr	$3.5 \times 10^5$	—	0.01	$1.1 \times 10^{10}$	$V_{DS} = 1; V_{GS} = 0$	309	
		FL GaSe/n-Si	—	23.6	$6 \times 10^{-5}$	—	$V_{DS} = 0$	310	
	GaTe	FL GaTe/FL MoS <sub>2</sub>	21.83	61.68	$< 7 \times 10^{-3}$	$8.4 \times 10^{13}$	$V_{DS} = 1; V_{GS} = 70$	311	
		FL GaTe/FL MoS <sub>2</sub>	1.365	266	$< 0.01$	—	$V_{DS} = 0$	312	
	Group IV–VI MMCs	SnS	FL GaTe <sub>x</sub> Se <sub>1-x</sub>	0.21	50	—	—	$V_{DS} = 0$	313
ML SnS/1L WS <sub>2</sub>			24.2	—	—	—	$V_{DS} = 5; V_{GS} = 0$	314	
FL SnS <sub>2</sub> /FL WSe <sub>2</sub>			244	—	0.013	$1.29 \times 10^{13}$	$V_{DS} = -1; V_{GS} = -20$	315	
IL SnS <sub>2</sub> /1L WSe <sub>2</sub>			0.108	—	$5 \times 10^{-4}$	$4.71 \times 10^{10}$	$V_{DS} = 5$	316	
FL SnS <sub>2</sub> /FL WSe <sub>2</sub>			—	—	$< 0.02$	—	$V_{DS} = 0$	317	
SnSe		FL SnS <sub>2</sub> /CIS QDs	630	—	$< 0.1$	—	$V_{DS} = 3; V_{GS} = 50$	318	
		FL SnSe/FL MoS <sub>2</sub>	100	$2.3 \times 10^4$	$< 0.01$	—	$V_{DS} = 0$	319	
Tetradymites		Bi <sub>2</sub> Se <sub>3</sub>	ML Bi <sub>2</sub> Se <sub>3</sub> /FL graphene	1.97	—	$4 \times 10^{-6}$	$1.7 \times 10^9$	$V_{DS} = 0.3; V_{GS} = 0.02$	214
			ML Bi <sub>2</sub> Se <sub>3</sub> /n-Si	24.28	—	$2.5 \times 10^{-6}$	$4.39 \times 10^{12}$	$V_{DS} = -1$	215
		Bi <sub>2</sub> Te <sub>3</sub>	ML Bi <sub>2</sub> Te <sub>3</sub> /1L Gr	35	—	$8.7 \times 10^{-3}$	—	$V_{DS} = 1$	213
	FL Bi <sub>2</sub> Te <sub>3</sub> /FL WS <sub>2</sub>		30.4	—	0.02	$2.3 \times 10^{11}$	$V_{DS} = 1$	320	
		ML Bi <sub>2</sub> Te <sub>3</sub> /n-Si	1	—	0.1	$2.5 \times 10^{11}$	$V_{DS} = -5$	321	

ML: multilayer; FL: few-layer; G: graphene; Vis: visible; NIR: near infrared; MIR: middle infrared; QD: quantum dot; NP: nanoparticle.



**Fig. 23** (a) Optical image of the fabricated device. The dark purple region is monolayer MoS<sub>2</sub>, while the blue flake is few-layer black phosphorus. The light purple region is SiO<sub>2</sub>. Scale bar, 10 μm. (b) Photodetection responsivity (*R*) calculated as a function of incident power. (c) *I*<sub>DS</sub> as a function of *V*<sub>DS</sub> under various laser powers. The *I*<sub>sc</sub> and *V*<sub>oc</sub> can be obtained from the intercepts of the curves on *I*<sub>DS</sub> and *V*<sub>DS</sub> axes. (d) SEM image of a device made on a 1L MoSe<sub>2</sub> partially covered by 1L GaSe domains. Electrodes 1 and 2 were made on the GaSe/MoSe<sub>2</sub> vdW heterostructure region, whereas electrode 3 was made on a bare 1L MoSe<sub>2</sub> region. Inset shows the corresponding optical micrograph. (e) *I*<sub>DS</sub>–*V*<sub>DS</sub> curves across the p(GaSe)–n(MoSe<sub>2</sub>) heterojunction (measured using electrodes 2 and 3) at different back-gate voltages (without illumination). The inset shows the *I*<sub>DS</sub>–*V*<sub>GS</sub> curve (with *V*<sub>DS</sub> fixed at 10 V) across the heterojunction. (f) *J*<sub>DS</sub>–*V*<sub>DS</sub> curves with white light illumination across the heterojunction at different back-gate voltages; (a–c) are reproduced from ref. 302 with permission from American Chemical Society, Copyright 2014 and (d–f) are reproduced from ref. 308 with permission from AAAS, Copyright 2016.

beam epitaxy.<sup>313</sup> A typical GaTe<sub>0.64</sub>Se<sub>0.36</sub>/Si photodiode has a responsivity of 0.21 A W<sup>-1</sup> and EQE of 50%. These wafer-scale Si-integration photodiode techniques may pave a new way for practical applications of 2D materials in the future.

SnS<sub>2</sub> is another important n-type 2DLM beyond graphene and TMDs.<sup>176,333–335</sup> Zhou *et al.* constructed a p-WSe<sub>2</sub>/p-SnS<sub>2</sub> (1.5 nm/4 nm thickness) photodiode on a 30 nm thick h-BN thin film by a mechanical exfoliation method combined with a dry transfer method.<sup>315</sup> The device and rectifying curves are shown in Fig. 24a and b, respectively. The WSe<sub>2</sub>/SnS<sub>2</sub> photodiode achieved both high responsivity (~244 A W<sup>-1</sup>) and high photodetectivity (1.29 × 10<sup>13</sup> Jones) at reverse bias conditions, which was attributed to a high direct tunneling current when the device was illuminated; Fig. 24c confirms this fact that the photogenerated carriers followed a direct tunneling mechanism. Very recently, Yang *et al.* reported a WSe<sub>2</sub>/SnS<sub>2</sub> (monolayer/monolayer) vertical heterostructure, with a lateral size up to millimeter scale, by a van der Waals epitaxial method.<sup>316</sup> Fig. 24d shows the optical image of a WSe<sub>2</sub>/SnS<sub>2</sub> photodiode while Fig. 24e reveals that the responsivity is up to 108 mA W<sup>-1</sup> and the detectivity reached up to 4.71 × 10<sup>10</sup> Jones at a forward bias of 5 V. Through a time-resolved photoresponse measurement (Fig. 24f), the rising time was estimated to be 500 μs. Because of the type-II band alignment and high carrier separation efficiencies based on the built-in electrical field, the WSe<sub>2</sub>/SnS<sub>2</sub> heterostructure also demonstrated self-driven photoswitching performance.<sup>317</sup> Besides, the SnS<sub>2</sub>, SnSe-based heterostructure

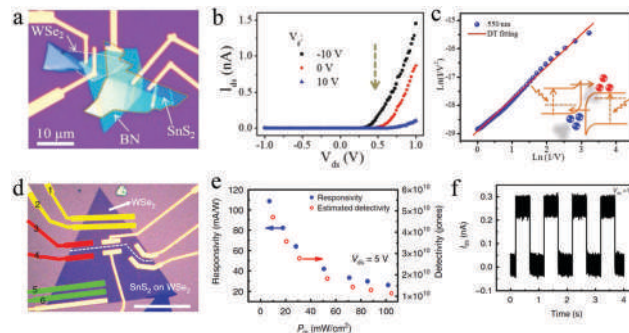


**Fig. 24** (a) Optical image of the WSe<sub>2</sub>/SnS<sub>2</sub> van der Waals heterostructure. (b) *I*<sub>DS</sub> versus *V*<sub>DS</sub> at different bottom gate bias. (c) *I*<sub>DS</sub> versus *V*<sub>DS</sub> curve in the reverse drain voltages and the energy band diagram of the WSe<sub>2</sub>/SnS<sub>2</sub> vdW heterostructure at reverse drain voltage. (d) Optical image of a fabricated WSe<sub>2</sub>/SnS<sub>2</sub> vdW heterostructure device. Scale bar, 60 μm. (e) Photoresponsivity and detectivity of the photodiode at various illumination power intensities. (f) Photocurrent response of the device; the laser light is turned on/off by a chopper worked at 1 Hz (520 nm, 101 mW cm<sup>-2</sup>, *V*<sub>DS</sub> = 1 V); (a–c) are reproduced from ref. 315 with permission from John Wiley & Sons Inc., Copyright 2018 and (d–f) are reproduced from ref. 316 with permission from Macmillan Publishers Ltd, Copyright 2017.

has also been studied. For example, Yang *et al.* realized a self-powered SnSe/MoS<sub>2</sub> (28 nm/7 nm thickness) photodiode, which exhibits <10 ms response time. When applying a forward bias of 1 V, the device exhibited a high photoresponsivity of 100 A W<sup>-1</sup> and a high EQE of 2.33 × 10<sup>4</sup>%.<sup>319</sup>

2D TIs in tetradymites, like Bi<sub>2</sub>Se<sub>3</sub> and Bi<sub>2</sub>Te<sub>3</sub>, are featured with small bandgaps and topologically protected surface states.<sup>336,337</sup> Yao *et al.* reported a vertically-constructed Bi<sub>2</sub>Te<sub>3</sub>/n-Si (100 nm thick/n-Si) photodiode fabricated by a pulse laser deposition method.<sup>321</sup> Importantly, this kind of device demonstrates a strong ability to detect ultra-broadband light ranged from the ultraviolet (370.6 nm) to terahertz (118 μm) with good reproducibility. In contrast to the high-cost molecular beam epitaxy and pulsed laser deposition used in the fabrication of GaSe/n-Si,<sup>310</sup> GaTe<sub>x</sub>Se<sub>1-x</sub>/n-Si,<sup>313</sup> and Bi<sub>2</sub>Te<sub>3</sub>/n-Si,<sup>321</sup> Zhang *et al.* employed a low-cost physical vapor deposition method to grow Bi<sub>2</sub>Se<sub>3</sub> thin films on a Si wafer by a van der Waals epitaxial mechanism.<sup>215</sup> The Bi<sub>2</sub>Se<sub>3</sub>/Si heterostructure exhibited excellent diode characteristics. At a reverse bias of –1 V and under 808 nm laser illumination, the Bi<sub>2</sub>Se<sub>3</sub>/Si photodiode has a high light responsivity of 24.28 A W<sup>-1</sup>, a high detectivity of 4.39 × 10<sup>12</sup> Jones, and a fast response speed of approximately 2.5 μs.

## 5.2 Hybrid phototransistors

A phototransistor generally operates with a photoconductive effect, photogating effect, or two effects combined, so it usually possesses a higher photogain than a photodiode. Typically, it is composed of a semiconducting channel material bridging the two ends of a source and drain, encapsulated with top and/or bottom dielectric layers.<sup>338</sup> The channel materials, including their crystal quality, crystal symmetry, doping degree, and thickness, strongly affect the performance of the phototransistors. And it also can be modified by forming hybrid structures with other chemical species, in which light is efficiently absorbed while

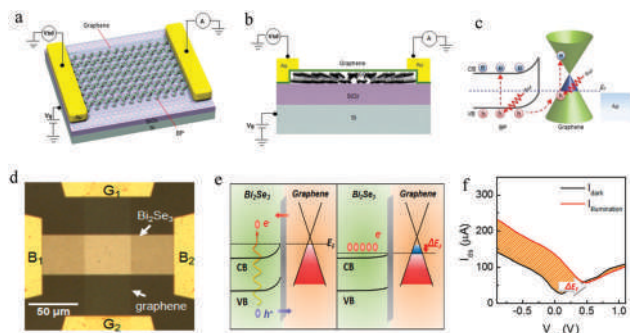


**Fig. 25** (a) Three-dimensional schematic diagram of the G/BP heterostructure photodetector, in which monolayer graphene is coated on top of a BP flake to enhance photocurrent response at 1550 nm and protect BP from the external environment. ( $V_{DS}$ : source–drain voltage,  $I_{DS}$ : source–drain current, and  $V_G$ : gate voltage.) (b) Schematic of the graphene–BP heterostructure-based photodetector and the circuit used to perform the two-terminal electrical measurements. (c) Band diagram of the G/BP heterostructure and the photoexcited hot carrier transport process under illumination corresponding to zero gate voltage ( $V_{GS}$ ); the dotted line represents the Fermi levels ( $E_F$ ). (d) Optical microscope image of the graphene– $\text{Bi}_2\text{Se}_3$  heterostructure photodetector based on an MBE-grown  $\text{Bi}_2\text{Se}_3$  topological insulator and wet-transferred CVD graphene. (e) Schematic band diagram and photoexcited hot-carrier transfer mechanism under light illumination. Electrons and holes are represented by red and blue dots, respectively. Vertical arrows represent photoexcitation, and lateral arrows represent tunneling of hot electron (red arrow) and hole (blue arrow). (f)  $I_{DS}$ – $V_{GS}$  characteristics of the measured graphene photodetector with (red,  $I_{\text{illumination}}$ ) and without (black,  $I_{\text{dark}}$ ) 50  $\mu\text{W}$  mid-IR light illumination; (a–c) are reproduced from ref. 101 with permission from American Chemical Society, Copyright 2017 and (d–f) are reproduced from ref. 214 with permission from American Chemical Society, Copyright 2017.

photogenerated electrons or holes can transfer into the conducting channel. Here, we name the devices using hybrid channel materials as “hybrid phototransistors,” and their photoresponse performances will be discussed in this section.

One typical hybrid structure is shown in Fig. 25a and b,<sup>101,307,309,320</sup> where one top layer (for example, graphene) covers the bottom layer (for instance, BP) and both layers connect with two electrodes. In this case,<sup>101</sup> the top G acts not only as an encapsulation layer but also as a high speed pathway for highly efficient charge carrier extraction because G has very good contacts with gold electrodes. As shown in Fig. 25c, under light illumination, electron–holes separate in BP with holes injected into G, thus leading to a photocurrent generation. The negative charges in a BP function as negative gates and result in a positive shift of the neutral point of graphene. So, the photogating effect plays a dominant role to on photocurrent generation. Because of these effects, a BP/G hybrid phototransistor exhibits an ultrahigh responsivity (up to  $3.3 \times 10^3 \text{ A W}^{-1}$ ), a photoconductive gain (up to  $1.13 \times 10^9$ ), and a rise time of about 4 ms at near infrared wavelength (1550 nm).<sup>101</sup> Meanwhile, due to the involvement of G, the device exhibits a long-term stability. Using a similar structure, Chen *et al.* fabricated a G/few-layer InSe heterostructure by transferring G to the top of mechanically exfoliated InSe. In comparison with pristine InSe devices, the performance of this hybrid structure achieved a four order of

magnitude improvement in responsivity and EQE. Under illumination of a 532 nm laser, the responsivity and EQE reached  $940 \text{ A W}^{-1}$  and  $2.18 \times 10^5\%$ , respectively.<sup>307</sup> A G/GaSe hybrid phototransistor has been also developed.<sup>309</sup> Attributed to the perfect interface between G and GaSe, the responsivity, detectivity, and response time reached up to  $3.5 \times 10^5 \text{ A W}^{-1}$ ,  $1.1 \times 10^{10}$  Jones, and 10 ms.

Another type of hybrid phototransistor is based on the modification of the channel materials using some special light sensitizers, including 2D, 1D, and 0D nanomaterials. Kim *et al.* reported a mid-IR photodetector based on  $\text{Bi}_2\text{Se}_3$  decorated graphene,<sup>318</sup> as shown in Fig. 25d. Similar to a G/BP hybrid phototransistor,<sup>101</sup> in this device, the  $\text{Bi}_2\text{Se}_3$  layer is the IR light absorber to supply holes to graphene and graphene functions as a high speed carrier transport pathway. Fig. 25e shows a photogenerated holes tunnel from  $\text{Bi}_2\text{Se}_3$  to graphene, leaving electrons accumulated at the bottom of the conduction band. Therefore, the so called photogating effect would be induced, as shown in Fig. 25f where a clearly positive shift of the neutral point can be observed. Attributed to the narrow band gap of  $\text{Bi}_2\text{Se}_3$  ( $\sim 0.3 \text{ eV}$ ), the device showed strong mid-IR photodetecting performance. The responsivity, detectivity, and response speed under mid-IR ( $3.5 \mu\text{m}$ ) illumination is  $1.97 \text{ A W}^{-1}$ ,  $1.7 \times 10^9$  Jones and 4  $\mu\text{s}$ , respectively.<sup>214</sup> Qiao *et al.* employed  $\text{Bi}_2\text{Te}_3$  as light absorbers to form a  $\text{Bi}_2\text{Te}_3$ –graphene heterostructure by *in situ* growth of  $\text{Bi}_2\text{Te}_3$  on the top of graphene.<sup>213</sup> The epitaxial interfaces between  $\text{Bi}_2\text{Te}_3$  and graphene enable effective transfer and separation of photoexcited carriers; thus, the photodetector has high responsivity ( $35 \text{ A W}^{-1}$ ) and high photogain (83) under 532 nm laser. The detection wavelength range can be also expanded to near-IR (1550 nm).

In addition, nanoparticles can also enhance the performance of phototransistors due to strong light absorption of the nanoparticles, effective charge separation and transfer, and additional photogating effects. For example, Jia *et al.* developed a  $\text{MoS}_2$  nanoparticle–BP hybrid phototransistor.<sup>305</sup> In comparison with pristine BP photodetectors, the responsivity showed a 40 times enhancement. Huang *et al.* constructed  $\text{SnS}_2$ –CIS quantum dots hybrid structures. Their responsivity reached  $630 \text{ A W}^{-1}$ , which is six times higher than the pristine  $\text{SnS}_2$ .<sup>318</sup>

In total, we discussed photodiodes and hybrid phototransistors based on 2D materials beyond graphene and TMDs, including BP,  $\text{SnS}_2$ , GaSe,  $\text{Bi}_2\text{Se}_3$  and  $\text{Bi}_2\text{Te}_3$ . Photodiodes based on them show photoresponsivity distributed from several  $\text{mA W}^{-1}$  to  $\sim 10^5 \text{ A W}^{-1}$ , while the response times were in a wide range from several  $\mu\text{s}$  to 0.1 s. The responsivities of most photodiodes or phototransistors based on 2D materials beyond graphene and TMDs are still smaller than those based on TMDs and graphene hybrids, such as graphene/ $\text{MoS}_2$ ,<sup>339</sup>  $\text{MoS}_2$ / $\text{PbS}$ ,<sup>340</sup>  $\text{ITO}/\text{MoS}_2/\text{Cu}_2\text{O}$ ,<sup>341</sup> and graphene/ $\text{PbS}$  heterostructures.<sup>342</sup> Especially, the responsivity of graphene/ $\text{MoS}_2$  is up to  $\sim 10^8$ .<sup>339</sup> These results should be related the high crystal quality, high carrier mobility, and relatively high light absorption of TMDs and graphene. Meanwhile, we also noted that the response times and detectivities of them are comparable and even better than those based on TMDs and graphene. Of course, this also strongly



depends on the device configuration and photodetection mechanism. In addition, some of the current results have been comparable with commercial photodetectors (such as Si and GaAs). However, large-scale, uniform fabrication processes are still an obstacle to realize practical applications. At this point, because of the high compatibility with Si, Bi<sub>2</sub>Se<sub>3</sub> and Bi<sub>2</sub>Te<sub>3</sub> may be closer to practical applications. On the other hand, hybrid phototransistors generally generate large photoresponsivity (up to 10<sup>5</sup> A W<sup>-1</sup> as seen from Table 3), but usually suffer from a relatively slow response speed. Nevertheless, graphene with extremely high carrier mobility may be helpful.

## 6. Enabling flexibility

Flexible, including bendable, twistable, and stretchable, device systems are a hot research topic in the areas of mechanics, electronics, and optoelectronics, as well as medicine, due to their potential applications like wearable health monitoring devices, diagnostic implements that can be integrated with human bodies, and flexible displays.<sup>343</sup> To enable flexibility, strategies including device configuration design (from the perspective of mechanics) and using materials with higher mechanical flexibility (from the perspective of materials science) are usually utilized. For the former, pre-designed special device structures that can release and/or offset applied stress have been widely adopted. For example, wavy and mesh shape devices based on silicon membranes (~100 nm in thickness) have been fabricated and show good flexibility.<sup>344–346</sup> As for the latter, both materials morphology and types can be parameters that modulate their flexibility.

According to the beam theory, deflection is inversely proportional to material thickness, *i.e.*, for a same material, the thinner the material the more flexible (bendable) it is. This is actually a fundamental of flexible devices based on polycrystalline Si thin films. From this point of view, 2DLMs with atomically thin thicknesses have a naturally huge advantage. In addition, well-studied flexible devices based on polycrystalline Si thin films and organic semiconductors usually suffer from low charge carrier mobility (~1 cm<sup>2</sup> V<sup>-1</sup> s<sup>-1</sup>), which further gives 2DLMs an opportunity.<sup>17</sup> Flexible FETs and photodetectors based on G and TMDs have been subsequently fabricated and studied.<sup>347–349</sup> On the other hand, considering the novel optoelectronic properties of 2DLMs other than G and TMDs that have been discussed above, they are also expected to have good photoresponse performances while integrated with flexible substrates.

Materials with high elastic limit strain ( $\epsilon_m$ ) and stress ( $\sigma_m$ ) are needed if they are expected to keep working while undergoing large transformation. Fig. 26 summarizes the values of  $\epsilon_m$  and  $\sigma_m$  of selected 2DLMs. As we can see, some of the 'new' members of 2DLMs have comparable or even higher flexibility, especially the elastic limit strain, than TMDs and/or G, making them more appealing for flexible devices like photodetectors.

A pioneering work on flexible devices was done in 2012,<sup>361</sup> which is almost the same time as the rising of TMDs and 5 years later than the first flexible TFTs achieved on graphene.<sup>347,362</sup> In this work, Peng *et al.* synthesized a topological insulator, Bi<sub>2</sub>Se<sub>3</sub> nanosheets, through van der Waals epitaxy showed their potentials as flexible transparent electrodes. These flexible devices were fabricated *in situ* by taking advantage of bendable

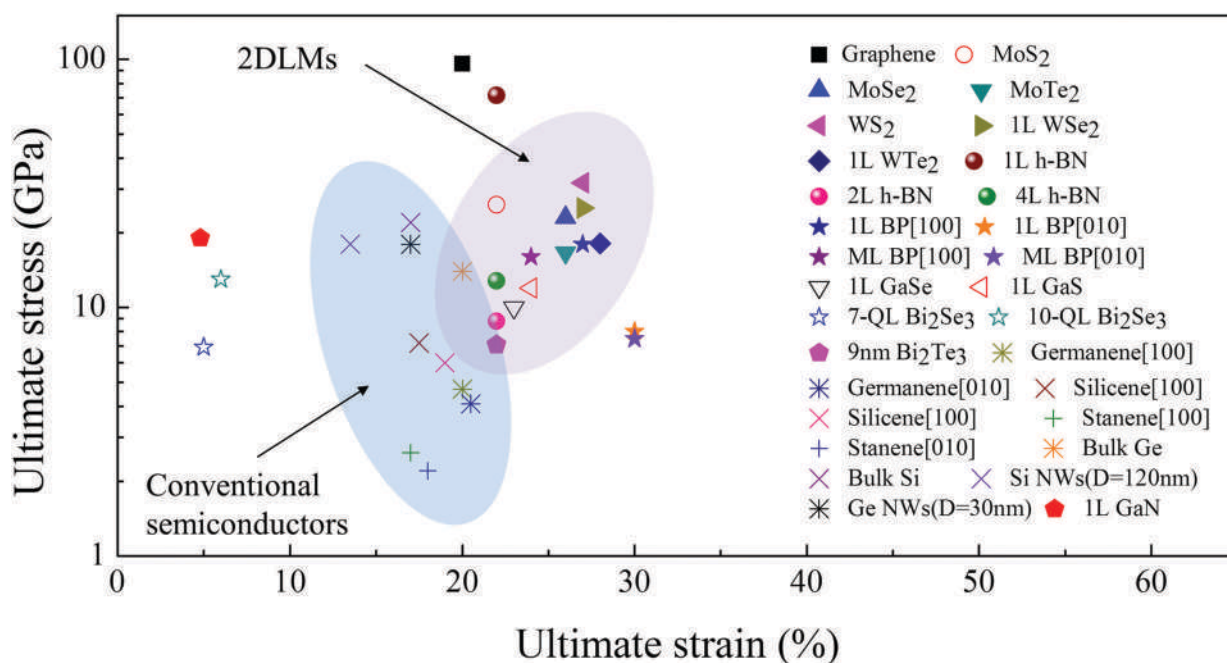
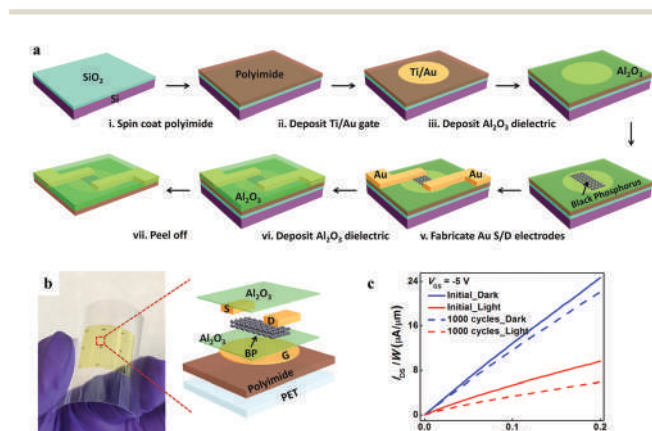


Fig. 26 Summarization of the mechanical properties at RT of selected 2DLMs. The values of conventional semiconductors like Si and Ge are also provided for reference. The values of Bi<sub>2</sub>Se<sub>3</sub>, Si nanowires, and Ge nanowires are obtained from experiments, while the others are calculated. The data are extracted from ref. 350–360.

mica substrates. Notably, a 10 nm thick device (on a 0.05 mm thick substrate) could keep the conductivity with bending radius down to 2 mm and exhibited long-term durability, which is much better than the commonly used ITO electrodes. This direct synthesis of 2DLMs on flexible substrates followed by *in situ* device fabrication has been widely adopted for preliminary demonstrations of the compatibility between 2DLMs and flexible substrates, which has been extended to many other 2D members such as GaSe, Te, and  $\text{In}_2\text{Se}_3$  (in which synthesis of arrays and flexible packaging were further studied) and  $\text{Pb}_x\text{Sn}_{1-x}\text{Se}$  (please see Sections 3.2, 3.1, and 4.1 for details).<sup>112,139,163</sup> Here, mica was chosen because of the dangling bond free nature of its surface and its stability at high temperature ( $> 900^\circ\text{C}$ ). However, compared with widely used pliable polymer substrates like PET, which have an elastic limit of 50–150%, mica exhibits relatively lower mechanical flexibility. On the other hand, a relatively higher temperature with the substrate is needed for usual synthesis methods, including not only 2DLMs but also other low-dimensional materials, such as CVD and MOCVD. To combine with these polymer substrates, an additional process like transfer is needed. Of course, some 2D materials like metal oxides (see Section 4 for details) have been synthesized through solution methods, where a relatively low temperature is required.<sup>363</sup> But these methods usually suffer from bad product quality which especially limits their application with high-performance electronic and optoelectronic devices like photodetectors.

As for 2DLMs, the capability of mechanical exfoliation makes direct positing of flakes onto flexible polymer substrates capable. This, at least, satisfies the requirements of fundamental studies and has been utilized on GaS, InSe, (see Section 3.2) and BP.<sup>79,133,158</sup> Fig. 27 uses Miao and his colleagues' work as an example.<sup>58</sup> Using rigid  $\text{SiO}_2/\text{Si}$  and PI as the initial rigid and flexible support, and PET as the final flexible substrates, respectively, they fabricated flexible IR photodetectors based on BP (Fig. 27a and b).



**Fig. 27** (a) Schematic flowchart illustrating the fabrication process of flexible BP devices. (b) Photograph of a flexible BP device attached on a transparent PET substrate in its bending state. The schematic in the right inset shows the enlarged view of the device structure. (c) Characteristics of a flexible BP photodetector measured in the dark and illumination states before and after 1000 bending cycles; (a–c) are reproduced from ref. 58 with permission from American Chemical Society, Copyright 2017.

The device could sustain mobility and on/off ratios with a bending radius down to 6 mm, and still showed obvious photoresponse to 830 nm light after bending 1000 times (Fig. 27c). Note that the photoresponse mechanism changed from photoconducting to a bolometric effect, with  $R$  as high as  $52\text{ A W}^{-1}$ , by introducing polyimide which has a low thermal conductivity.

For practical applications, mechanical exfoliation is definitely not the choice. The large-area controlled growth of 2DLMs (graphene not included of course, but the synthesis of large-size single-crystal graphene is still ongoing) has actually become one of the most serious bottlenecks that limit further progress, not only for flexible devices but also the whole area. Fortunately, it seems that the integration with flexible polymer substrates on the basis of successful massive growth of 2DLMs is not difficult. For example, the roll-to-roll transfer of graphene onto polymer substrates has been commercialized benefitting from the relative flexibility of metal foils which are utilized as substrates for graphene synthesis.<sup>364</sup> On the other hand, the synthesis of other 2DLMs (excluded hBN) is usually carried out on rigid substrates such as Si, SOI, sapphire, and silica, which disables the R-2-R process. However, the ease of chemical etching the substrates, like dipping them into corrosive solutions including KOH and HF, makes the detaching of as-grown 2DLMs and arbitrary transfer to any flexible substrates viable.<sup>365–368</sup> Additionally, the chemical etching process is sometimes unneeded because of the weak adhesion of 2DLMs on the substrates coming from weak van der Waals forces.<sup>369,370</sup> Moreover, the detaching process can be completed without any assistance from solutions which brings transferred 2DLMs with high-quality interfaces.<sup>371,372</sup> For example, through using a photoresist/thermal release tape (TRT) combination, Kang *et al.* achieved the detaching process by direct peeling.<sup>373</sup> On the basis of the successful growth of wafer-scale TMDs monolayers and developed programmed vacuum stack (PVS) method, the authors could fabricate large-scale vdWHs and transfer them onto arbitrary substrates including flexible ones.

One thing worthy of being mentioned is that 2DLMs also bring a new opportunity to flexible optoelectronic devices based on conventional semiconductors like III–V groups.<sup>375,376</sup> The above-mentioned detaching, combined with a following transfer process, is usually impractical for conventional materials because of the strong bonds between substrates and grown materials. However, it becomes feasible by introducing 2DLMs buffer layers on the top of rigid substrates before materials growth. Due to weak van der Waals forces at the substrates/2DLMs/grown materials interfaces, the as-grown materials can be easily peeled off and transferred to flexible substrates. This idea was first realized with GaN-based LEDs in 2010.<sup>375</sup> Very recently, this method was successfully extended to the epitaxy growth of the III–V semiconductors group by Kim *et al.*, which lies at the heart of a wider range of modern optoelectronics. Fig. 28a illustrates the basic idea. The authors transferred a single-layer graphene onto a GaAs substrate, and then achieved epitaxy growth of GaAs film using industrial MOCVD. The epitaxy growth mode (Fig. 28b and c) can be realized because of the transparent role of single-layer graphene on the interaction

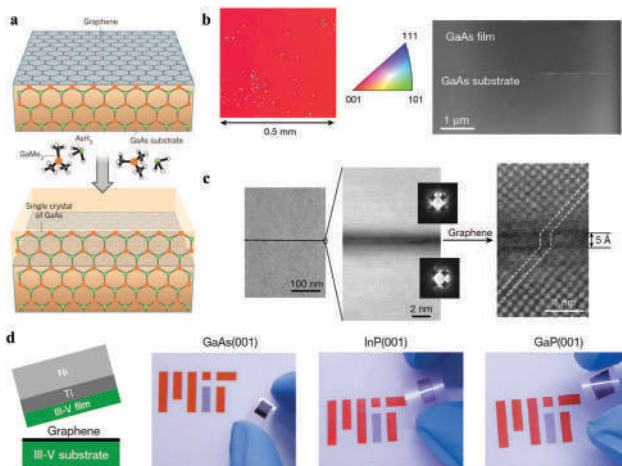


**Fig. 28** (a) Schematics of G-enabled remote epitaxy of III-V semiconductors like GaAs. (b) Left: EBSD map of GaAs grown exfoliated from G/GaAs(001) substrate. Right: Low-angle annular dark field STEM image of the GaAs/G/GaAs system showing no dislocations. (c) High-resolution STEM images of the system showing an excellent remote alignment of the GaAs(001) lattices through the graphene. (d) Schematic illustration of the exfoliation process and photographs of single-crystalline GaAs(001), InP(001), and GaP(001) films exfoliated from substrates; (a) is reproduced from ref. 374 with permission from Macmillan Publishers Ltd, Copyright 2017 and (b–d) are reproduced from ref. 22 with permission from Macmillan Publishers Ltd, Copyright 2017.

between grown GaAs and the substrate beneath graphene. Additionally, the interlayer graphene also enables peeling off and the subsequent transfer of GaAs films onto flexible substrates (Fig. 28d).<sup>22</sup>

## 7. Summary and perspective

In summary, we have reviewed the state-of-the-art research situations of photodetection based on two-dimensional materials beyond graphene and TMDs, including elementary materials (BP, Te, Si, Ge, and Sn, *etc.*), main group metal chalcogenides (Ga-based, In-based, Ge-based, and Sn-based, *etc.*), transition metal trichalcogenides (TiS<sub>3</sub>, ZrS<sub>3</sub>, and HfS<sub>3</sub>, *etc.*), tetradymites (Bi<sub>2</sub>Se<sub>3</sub>, Bi<sub>2</sub>Te<sub>3</sub>, and Sb<sub>2</sub>Te<sub>3</sub>, *etc.*), h-BN, metal halides (CrCl<sub>2</sub>, MgCl<sub>2</sub>, and PbI<sub>2</sub>, *etc.*), transition metal chalcogenophosphates (MPS<sub>3</sub>, MPSe<sub>3</sub>, *etc.*), Bi-based oxychalcogenides (Bi<sub>2</sub>O<sub>2</sub>Se, *etc.*), 2D non-layered materials (ZnO, CdTe, PbS, GaN, *etc.*), and their hybrid structures. Some of them, such as BP, Ga-/In-/Sn-based MMCs, Bi<sub>2</sub>Se<sub>3</sub> in tetradymites, and 2D PbS, have been studied for years. The basic properties, synthesis, and applications as photodetectors of these materials have been relatively well studied. Others, like Te, TMCPs, and BOCs, are recently rediscovered and only their basic properties are revealed. However, based on the finite results, we can see that these new members of 2D materials have shown comparable, or even higher photoresponse performances, than the well-known TMDs.

BP is one of most widely studied elementary 2D materials. It has displayed features of high carrier mobility and widely tunable direct bandgap, making BP a very promising candidate

for high-performance optoelectronic applications, especially for the IR detection. Until now, photodetectors based on BP have shown response to UV (310 nm)-IR (3.75 μm) and THz (~0.3 THz) ranges with responsivity up to a few orders of A W<sup>-1</sup>. Notably, NEP as low as 10<sup>-12</sup> W Hz<sup>-1/2</sup> has been demonstrated for 3.39 μm light at room temperature, which is already at the level of commercialization. However, BP still suffers from its bad stability in ambient environments. Various methods, such as encapsulation, surface passivation, ion doping, and others, have been used to improve its stability. Among them, using graphene or h-BN as a protection layer to construct van der Waals heterostructures may be the most promising choice, which is still waiting for deeper studies. Actually, considering the success of synthesizing large-scale graphene and hBN (and TMDs), controllable growth of BP has become a bottleneck that limits the further development. With narrow bandgaps and topologically protected surface states (which gives rise to higher absorption than Hg<sub>x</sub>Cd<sub>1-x</sub>Te at IR range), 2D topological insulators in tetradymites are additional promising candidates for IR detection. Remarkably, these materials including Bi<sub>2</sub>Se<sub>3</sub> and Bi<sub>2</sub>Te<sub>3</sub> have been grown on silicon substrates in wafer scale *via* PLD and MBE methods. Additionally, they show high air-stability which is strongly in contrast to BP. However, until now, they have caused limited attention and their possibility is still waiting to be fully developed.

With suitable bandgap coverage (~0.9–3.9 eV), main group metal chalcogenides, such as In-based, Ga-based, Ge-based and Sn-based, are very promising for visible light range detection. They also have other features like high composition tunability and good flexibility, which further makes them stand out in the big 2D family. Among them, Ga-based MMCs should be more interesting due to their intrinsic properties and the fact that their wafer-scale growth has been realized on silicon by MBE and PLD methods, which is beneficial for practical applications. However, there are still variations in the photodetection performances between reported values. And systematic studies are needed.

The other 2DLMs have a relatively shorter history than that mentioned above. Nevertheless, theoretical or primary experimental works have predicted their potentials. In the elementary 2DLMs, Te is recently rediscovered and few studies of its photodetection properties have been reported. However, research must be around the corner considering the promising potentials Te has. Other elementary 2D materials, such as Si, Ge, Sn, Bi, and Sb, seem to be still too far from true photodetectors due to their poor stability and dominant metallic properties. One rising star is Be<sub>2</sub>O<sub>2</sub>Se which has been featured with suitable bandgap, high charge carrier mobility, and high photoresponse performances. However, such a limited number of works has been published on them and so many of their properties, even the most basic ones, are still unclear. Clearly, more attention is needed.

Photodetection properties of a few transition metal trichalcogenides and metal halides have been studied. The former seem to have opportunity with UV detection considering their wide bandgaps. However, similar with BP, the issue of their stability



must be resolved by further exploration. On the other hand, transition metal chalcogenophosphates usually exhibit low carrier density, thus low photocurrent. For these three kinds of materials, the prospect is still unclear. Their magnetic properties and interactions between lights and 2D magnets may show something unexpected.

Non-layered 2D materials can be a very big group while current research is mainly focusing on the group III–V and group II–V semiconductors. Because of recent breakthroughs in 2D GaN, InAs, InP, GaAs, ZnO, and CdTe, this research area is attracting intensely growing attention. Unlike 2D layered materials, they own rich surface states originating from the large amounts of dangling bonds when the thickness approaches a several atoms scale. So, it is a great challenge to maintain their high carrier mobility and stability at this scale. Hence, there should be a trade-off between purchasing ultra-thin thickness and high performance.

Strategies like photodiodes and hybrid phototransistors based on constructing heterostructures can be used to further improve photodetection performance and bring unexpected properties. Photodiodes generally have fast response time, low dark current and high detectivity, but low photogain. Hybrid phototransistors generally generate large photoresponsivity. However, they suffer from a relatively slow response time. In the future, on one side, development of growth methods for high quality crystals, large area, and importantly, integration with silicon wafers, is highly desired. On the other side, combination with graphene is an effective route to enhance device performance, where 2D semiconducting materials act as a light absorber while graphene works as a high carrier transport pathway.

In total, research on photodetection based on these new 2D materials is still at its initial stage. Although some of them have been studied for a few years, there are always new members that keep joining the big family. And a number of issues/questions need to be addressed in the near future. As with the whole 2D family and any other newly developed materials, the first thing is to achieve controllable synthesis with high quality. Synthesizing bulks through chemical vapor transport (CVT) plus a mechanical exfoliation method may be a smart choice for initial property exfoliations, but definitely cannot support long-term development. On the other hand, CVD could be a promising candidate which has shown high potential. Especially, the recently-developed molten-salt-assisted method has unlocked the synthesis of a considerable number of 2DLMs flakes with thickness down to a monolayer. Nevertheless, the synthesis of 2DLMs through CVD seems still to suffer from a few problems: the random distribution of 2D flakes, poor uniformity of thickness, and relatively low quality for large-scale films. This is probably due to unsatisfied control over the reaction dynamics where solids are usually used as sources. For a better controllability, sources in liquid and/or gaseous phases could be taken into consideration, just like what have been done in the CVD growth of graphene and MOCVD growth of traditional semiconductors.

A second important area is mechanism exploration. Many 2DLMs have been found with high photoresponse performances

with, for example,  $R$  as high as hundreds and even thousands  $\text{A W}^{-1}$ , which is orders higher than conventional photodetectors. Although a great number of works have been done on related fields, the picture behind these high values is relatively rarely studied. In addition, a figure of merit with more practical meanings, like NEP and specific detectivity, should be used to evaluate the “true” performances of photodetectors based on 2DLMs studied. And these parameters, with measured rather than approximated values, are strongly recommended.

The light absorption of individual few-layer 2DLMs, even monolayer ones, is considerable, but the absolute value is still low. Even though many methods have been proposed, an effective strategy without significantly introducing fabrication complexities is still absent. The authors believe that, utilizing advantages of van der Waals heterostructures, the vertical integration of devices based on individual 2DLMs layers may be a choice. To do this, controllable synthesis and targeted transfer with high-quality interfaces are the main prerequisites. For the latter, strategies that are accomplished without involving polymer/liquid, and processes that are done in a vacuum/inert gas protected atmosphere are helpful. These can be achieved by using substrates with inert surfaces, like H-passivated SOI and van der Waals substrates (like mica), for the synthesis process.

One main specialty of 2DLMs lies on constructing van der Waals heterostructures, which has resulted in numerous novel properties and functionalities. Examples include energy-efficient photodetectors based on self-driven van der Waals heterostructures. In the conventional regime, this is due to a built-in potential coming from the interacting of p- and n-type semiconductors. However, there has been evidence showing that the conduction behaviors of 2DLMs are determined by injection/extraction of charge carriers at the contact regions. A result is the change (or combination) of the mechanism underlying the self-driven capability from the p–n junction to the band alignment. A clear picture is still absent, but, no matter which mechanism it is, the coming of new members will definitely expand the choices of materials to construct energy-efficient photodetectors with more suitable combinations.

Finally, it should be noted that, besides the materials mentioned in this manuscript, there are still a large number of materials that exist and/or can be synthesized in a 2D morphology. For a better exploration of these potential members with desired properties, first principle calculations are really needed. Considering the big successes that 2D materials have already achieved, it is worth looking forward to what they will bring to us in the near future.

## List of symbols

2DLMS	Two-dimensional layered materials
vdWHS	van der Waals heterostructures
G	Graphene
BP	Black phosphorous
TMDs	Transition metal dichalcogenides
MMCS	Main group metal chalcogenides
TMTs	Transition metal trichalcogenides

MHs	Metal halides
TMCPs	Transition metal chalcogenophosphates
Tis	Topological insulators
UV	Ultraviolet
IR	Infrared
$E_g$	Band gap
$V_{oc}$	Open-circuit voltage
$I_{sc}$	Short-circuit current
$V_{DS}$	Source–drain voltage
$I_{DS}$	Source–drain current
$V_{GS}$	Gate voltage
PVE	Photovoltaic effect
PCE	Photoconductive effect
PGE	photogating effect
PTE	photo-thermoelectric effect
BE	bolometric effect
$S$	Seebeck coefficient
$h$	Planck constant
$\nu$	Frequency of incident light
$\lambda$	Wavelength of incident light
$k_B$	Boltzmann constant
$q$	Elementary electron charge
$E$	Electric field
$\varepsilon$	Strain
$E_F$	Fermi energy
$\sigma$	Conductivity
$T$	Temperature
$t$	Time
$R$	Responsivity
$I_{ph}$	Photocurrent
$I_d$	Dark current
$P_{in}$	Incident light power
$\eta$	Quantum efficiency
$L$	Separation distance of source–drain electrodes
$G$	Gain
EQE	External quantum efficiency
IQE	Internal quantum efficiency
SNR	Signal to noise ratio
NEP	Noise equivalent power
$D^*$	Specific detectivity
$\tau_r$	Rise time
$\tau_d$	Decay time

## Author contributions

J. H., F. W. and Z. W. discussed the outline of the manuscript. F. W., Z. W., L. Y., R. C., and Y. W. wrote the manuscript. J. W., F. W, Y. Z, and X. Z. helped with the literature research. T. A. S. helped revising the manuscript. J. He supervised the work. All the authors gave discussions about the manuscript.

## Conflicts of interest

There are no conflicts to declare.

## Acknowledgements

This work was supported by National Natural Science Foundation of China (No. 61625401, 61474033, 61574050, 11674072 and 21703047), Ministry of Science and Technology of China (No. 2016YFA0200700), Strategic Priority Research Program of the Chinese Academy of Sciences (Grant No. XDA09040201), and CAS Key Laboratory of Nanosystem and Hierarchical Fabrication. The authors also gratefully acknowledge the support of Youth Innovation Promotion Association CAS.

## References

- G. Konstantatos and E. H. Sargent, *Nat. Nanotechnol.*, 2010, **5**, 391–400.
- A. Rogalski, J. Antoszewski and L. Faraone, *J. Appl. Phys.*, 2009, **105**, 091101.
- B. Nabet, *Photodetectors: Materials, Devices and Applications*, Woodhead Publishing, 2016.
- C. M. Herzinger, B. Johs, W. A. McGahan, J. A. Woollam and W. Paulson, *J. Appl. Phys.*, 1998, **83**, 3323–3336.
- A. Rogalski, *Rep. Prog. Phys.*, 2005, **68**, 2267–2336.
- J. X. Wu, H. T. Yuan, M. M. Meng, C. Chen, Y. Sun, Z. Y. Chen, W. H. Dang, C. W. Tan, Y. J. Liu, J. B. Yin, Y. B. Zhou, S. Y. Huang, H. Q. Xu, Y. Cui, H. Y. Hwang, Z. F. Liu, Y. L. Chen, B. H. Yan and H. L. Peng, *Nat. Nanotechnol.*, 2017, **12**, 530–534.
- M. Buscema, J. O. Island, D. J. Groenendijk, S. I. Blanter, G. A. Steele, H. S. J. van der Zant and A. Castellanos-Gomez, *Chem. Soc. Rev.*, 2015, **44**, 3691–3718.
- F. H. L. Koppens, T. Mueller, P. Avouris, A. C. Ferrari, M. S. Vitiello and M. Polini, *Nat. Nanotechnol.*, 2014, **9**, 780–793.
- Z. H. Sun and H. X. Chang, *ACS Nano*, 2014, **8**, 4133–4156.
- K. F. Mak and J. Shan, *Nat. Photonics*, 2016, **10**, 216–226.
- G. Fiori, F. Bonaccorso, G. Iannaccone, T. Palacios, D. Neumaier, A. Seabaugh, S. K. Banerjee and L. Colombo, *Nat. Nanotechnol.*, 2014, **9**, 768–779.
- Y. Liu, N. O. Weiss, X. D. Duan, H. C. Cheng, Y. Huang and X. F. Duan, *Nat. Rev. Mater.*, 2016, **1**, 16042.
- K. S. Novoselov, A. Mishchenko, A. Carvalho and A. H. C. Neto, *Science*, 2016, **353**, aac9439.
- A. K. Geim and I. V. Grigorieva, *Nature*, 2013, **499**, 419–425.
- R. R. Nair, P. Blake, A. N. Grigorenko, K. S. Novoselov, T. J. Booth, T. Stauber, N. M. R. Peres and A. K. Geim, *Science*, 2008, **320**, 1308.
- L. Britnell, R. M. Ribeiro, A. Eckmann, R. Jalil, B. D. Belle, A. Mishchenko, Y. J. Kim, R. V. Gorbachev, T. Georgiou, S. V. Morozov, A. N. Grigorenko, A. K. Geim, C. Casiraghi, A. H. Castro Neto and K. S. Novoselov, *Science*, 2013, **340**, 1311–1314.
- D. Akinwande, N. Petrone and J. Hone, *Nat. Commun.*, 2014, **5**, 5678.
- Q. S. Guo, A. Pospischil, M. Bhuiyan, H. Jiang, H. Tian, D. Farmer, B. C. Deng, C. Li, S. J. Han, H. Wang, Q. F. Xia, T. P. Ma, T. Mueller and F. N. Xia, *Nano Lett.*, 2016, **16**, 4648–4655.

- 19 H. T. Yuan, X. G. Liu, F. Afshinmanesh, W. Li, G. Xu, J. Sun, B. Lian, A. G. Curto, G. J. Ye, Y. Hikita, Z. X. Shen, S. C. Zhang, X. H. Chen, M. Brongersma, H. Y. Hwang and Y. Cui, *Nat. Nanotechnol.*, 2015, **10**, 707–713.
- 20 S. Dai, Z. Fei, Q. Ma, A. S. Rodin, M. Wagner, A. S. McLeod, M. K. Liu, W. Gannett, W. Regan, K. Watanabe, T. Taniguchi, M. Thiemens, G. Dominguez, A. H. C. Neto, A. Zettl, F. Keilmann, P. Jarillo-Herrero, M. M. Fogler and D. N. Basov, *Science*, 2014, **343**, 1125–1129.
- 21 F. Wang, Z. X. Wang, T. A. Shifa, Y. Wen, F. M. Wang, X. Y. Zhan, Q. S. Wang, K. Xu, Y. Huang, L. Yin, C. Jiang and J. He, *Adv. Funct. Mater.*, 2017, **27**, 1603254.
- 22 Y. Kim, S. S. Cruz, K. Lee, B. O. Alawode, C. Choi, Y. Song, J. M. Johnson, C. Heidelberger, W. Kong, S. Choi, K. Qiao, I. Almansouri, E. A. Fitzgerald, J. Kong, A. M. Kolpak, J. Hwang and J. Kim, *Nature*, 2017, **544**, 340–343.
- 23 G. R. Bhimanapati, Z. Lin, V. Meunier, Y. Jung, J. Cha, S. Das, D. Xiao, Y. Son, M. S. Strano, V. R. Cooper, L. B. Liang, S. G. Louie, E. Ringe, W. Zhou, S. S. Kim, R. R. Naik, B. G. Sumpter, H. Terrones, F. N. Xia, Y. L. Wang, J. Zhu, D. Akinwande, N. Alem, J. A. Schuller, R. E. Schaak, M. Terrones and J. A. Robinson, *ACS Nano*, 2015, **9**, 11509–11539.
- 24 X. Zhou, Q. Zhang, L. Gan, H. Q. Li, J. Xiong and T. Y. Zhai, *Adv. Sci.*, 2016, **3**, 1600177.
- 25 S. Das, J. A. Robinson, M. Dubey, H. Terrones and M. Terrones, *Annu. Rev. Mater. Res.*, 2015, **45**, 1–27.
- 26 F. N. Xia, H. Wang, D. Xiao, M. Dubey and A. Ramasubramaniam, *Nat. Photonics*, 2014, **8**, 899–907.
- 27 S. Z. Butler, S. M. Hollen, L. Y. Cao, Y. Cui, J. A. Gupta, H. R. Gutierrez, T. F. Heinz, S. S. Hong, J. X. Huang, A. F. Ismach, E. Johnston-Halperin, M. Kuno, V. V. Plashnitsa, R. D. Robinson, R. S. Ruoff, S. Salahuddin, J. Shan, L. Shi, M. G. Spencer, M. Terrones, W. Windl and J. E. Goldberger, *ACS Nano*, 2013, **7**, 2898–2926.
- 28 W. Lee, Y. Liu, Y. Lee, B. K. Sharma, S. M. Shinde, S. D. Kim, K. Nan, Z. Yan, M. D. Han, Y. G. Huang, Y. H. Zhang, J. H. Ahn and J. A. Rogers, *Nat. Commun.*, 2018, **9**, 1417.
- 29 Z. Lou, Z. Liang and G. Shen, *J. Semicond.*, 2016, **37**, 9.
- 30 M. J. Bojdys, *Macromol. Chem. Phys.*, 2016, **217**, 232–241.
- 31 C. Xie, C. Mak, X. M. Tao and F. Yan, *Adv. Funct. Mater.*, 2017, **27**, 1603886.
- 32 N. Mounet, M. Gibertini, P. Schwaller, D. Campi, A. Merkys, A. Marrazzo, T. Sohier, I. E. Castelli, A. Cepellotti, G. Pizzi and N. Marzari, *Nat. Nanotechnol.*, 2018, **13**, 246–252.
- 33 F. C. Liu, H. Shimotani, H. Shang, T. Kanagasekaran, V. Zolyomi, N. Drummond, V. I. Fal'ko and K. Tanigaki, *ACS Nano*, 2014, **8**, 752–760.
- 34 H. Liu, A. T. Neal, Z. Zhu, Z. Luo, X. F. Xu, D. Tomanek and P. D. Ye, *ACS Nano*, 2014, **8**, 4033–4041.
- 35 X. A. Zhang, J. Wang and S. C. Zhang, *Phys. Rev. B: Condens. Matter Mater. Phys.*, 2010, **82**, 245107.
- 36 S. Lei, F. Wen, L. Ge, S. Najmaei, A. George, Y. Gong, W. Gao, Z. Jin, B. Li, J. Lou, J. Kono, R. Vajtai, P. Ajayan and N. J. Halas, *Nano Lett.*, 2015, **15**, 3048–3055.
- 37 P. Agnihotri, P. Dhakras and J. U. Lee, *Nano Lett.*, 2016, **16**, 4355–4360.
- 38 M. Buscema, J. O. Island, D. J. Groenendijk, S. I. Blanter, G. A. Steele, H. S. van der Zant and A. Castellanos-Gomez, *Chem. Soc. Rev.*, 2015, **44**, 3691–3718.
- 39 C. H. Liu, Y. C. Chang, T. B. Norris and Z. H. Zhong, *Nat. Nanotechnol.*, 2014, **9**, 273–278.
- 40 L. Yin, X. Zhan, K. Xu, F. Wang, Z. Wang, Y. Huang, Q. Wang, C. Jiang and J. He, *Appl. Phys. Lett.*, 2016, **108**, 043503.
- 41 H. Fang and W. Hu, *Adv. Sci.*, 2017, **4**, 1700323.
- 42 Y. Liu, Q. Xia, J. He and Z. Liu, *Nanoscale Res. Lett.*, 2017, **12**, 93.
- 43 X. Guo, W. Wang, H. Nan, Y. Yu, J. Jiang, W. Zhao, J. Li, Z. Zafar, N. Xiang, Z. Ni, W. Hu, Y. You and Z. Ni, *Optica*, 2016, **3**, 1066–1070.
- 44 X. Xu, N. M. Gabor, J. S. Alden, A. M. van der Zande and P. L. McEuen, *Nano Lett.*, 2010, **10**, 562–566.
- 45 M. Freitag, T. Low, F. N. Xia and P. Avouris, *Nat. Photonics*, 2013, **7**, 53–59.
- 46 M. Engel, M. Steiner and P. Avouris, *Nano Lett.*, 2014, **14**, 6414–6417.
- 47 Y. Dai, X. Wang, W. Peng, C. Xu, C. Wu, K. Dong, R. Liu and Z. L. Wang, *Adv. Mater.*, 2018, **30**, 1705893.
- 48 M. Kumar, M. Patel, T. T. Nguyen, J. Kim and J. Yi, *Nanoscale*, 2018, **10**, 6928–6935.
- 49 M. Kumar, M. Patel, J. Kim and D. Lim, *Nanoscale*, 2017, **9**, 19201–19208.
- 50 W. Peng, X. Wang, R. Yu, Y. Dai, H. Zou, A. C. Wang, Y. He and Z. L. Wang, *Adv. Mater.*, 2017, **29**, 1606698.
- 51 D. Saeedkia, *Handbook of terahertz technology for imaging, sensing and communications*, Woodhead Publishing, 2013.
- 52 L. Viti, J. Hu, D. Coquillat, W. Knap, A. Tredicucci, A. Politano and M. S. Vitiello, *Adv. Mater.*, 2015, **27**, 5567–5572.
- 53 L. Viti, J. Hu, D. Coquillat, A. Politano, C. Consejo, W. Knap and M. S. Vitiello, *Adv. Mater.*, 2016, **28**, 7390–7396.
- 54 L. Viti, J. Hu, D. Coquillat, A. Politano, W. Knap and M. S. Vitiello, *Sci. Rep.*, 2016, **6**, 20474.
- 55 M. Dyakonov and M. Shur, *Phys. Rev. Lett.*, 1993, **71**, 2465–2468.
- 56 M. Dyakonov and M. Shur, *IEEE Trans. Electron Devices*, 1996, **43**, 380–387.
- 57 M. Sakowicz, M. B. Lifshits, O. A. Klimenko, F. Schuster, D. Coquillat, F. Teppe and W. Knap, *J. Appl. Phys.*, 2011, **110**, 054512.
- 58 J. S. Miao, B. Song, Q. Li, L. Cai, S. M. Zhang, W. D. Hu, L. X. Dong and C. Wang, *ACS Nano*, 2017, **11**, 6048–6056.
- 59 S. R. Tamalampudi, Y. Y. Lu, U. R. Kumar, R. Sankar, C. D. Liao, B. K. Moorthy, C. H. Cheng, F. C. Chou and Y. T. Chen, *Nano Lett.*, 2014, **14**, 2800–2806.
- 60 C. Casiraghi, A. Hartschuh, E. Lidorikis, H. Qian, H. Harutyunyan, T. Gokus, K. S. Novoselov and A. C. Ferrari, *Nano Lett.*, 2007, **7**, 2711–2717.
- 61 M. M. Furchi, A. Pospischil, F. Libisch, J. Burgdorfer and T. Mueller, *Nano Lett.*, 2014, **14**, 4785–4791.
- 62 D. Kufer and G. Konstantatos, *Nano Lett.*, 2015, **15**, 7307–7313.



- 63 W. Zhang, J. K. Huang, C. H. Chen, Y. H. Chang, Y. J. Cheng and L. J. Li, *Adv. Mater.*, 2013, **25**, 3456–3461.
- 64 M. M. Furchi, D. K. Polyushkin, A. Pospischil and T. Mueller, *Nano Lett.*, 2014, **14**, 6165–6170.
- 65 K. Xu, Z. Wang, F. Wang, Y. Huang, F. Wang, L. Yin, C. Jiang and J. He, *Adv. Mater.*, 2015, **27**, 7881–7887.
- 66 Y. Q. Bie, G. Grosso, M. Heuck, M. M. Furchi, Y. Cao, J. Zheng, D. Bunandar, E. Navarro-Moratalla, L. Zhou, D. K. Efetov, T. Taniguchi, K. Watanabe, J. Kong, D. Englund and P. Jarillo-Herrero, *Nat. Nanotechnol.*, 2017, **12**, 1124–1129.
- 67 S. Balendhran, S. Walia, H. Nili, S. Sriram and M. Bhaskaran, *Small*, 2015, **11**, 640–652.
- 68 L. K. Li, Y. J. Yu, G. J. Ye, Q. Q. Ge, X. D. Ou, H. Wu, D. L. Feng, X. H. Chen and Y. B. Zhang, *Nat. Nanotechnol.*, 2014, **9**, 372–377.
- 69 F. N. Xia, H. Wang and Y. C. Jia, *Nat. Commun.*, 2014, **5**, 4458.
- 70 X. M. Wang, A. M. Jones, K. L. Seyler, V. Tran, Y. C. Jia, H. Zhao, H. Wang, L. Yang, X. D. Xu and F. N. Xia, *Nat. Nanotechnol.*, 2015, **10**, 517–521.
- 71 M. Buscema, D. J. Groenendijk, S. I. Blanter, G. A. Steele, H. S. J. van der Zant and A. Castellanos-Gomez, *Nano Lett.*, 2014, **14**, 3347–3352.
- 72 M. Engel, M. Steiner and P. Avouris, *Nano Lett.*, 2014, **14**, 6414–6417.
- 73 T. Low, M. Engel, M. Steiner and P. Avouris, *Phys. Rev. B: Condens. Matter Mater. Phys.*, 2014, **90**, 081408.
- 74 V. Tran, R. Soklaski, Y. F. Liang and L. Yang, *Phys. Rev. B: Condens. Matter Mater. Phys.*, 2014, **89**, 235319.
- 75 A. Castellanos-Gomez, L. Vicarelli, E. Prada, J. O. Island, K. L. Narasimha-Acharya, S. I. Blanter, D. J. Groenendijk, M. Buscema, G. A. Steele, J. V. Alvarez, H. W. Zandbergen, J. J. Palacios and H. S. J. van der Zant, *2D Mater.*, 2014, **1**, 025001.
- 76 J. Yang, R. J. Xu, J. J. Pei, Y. W. Myint, F. Wang, Z. Wang, S. Zhang, Z. F. Yu and Y. R. Lu, *Light: Sci. Appl.*, 2015, **4**, e312.
- 77 J. S. Qiao, X. H. Kong, Z. X. Hu, F. Yang and W. Ji, *Nat. Commun.*, 2014, **5**, 4475.
- 78 B. L. Liu, M. Kopf, A. N. Abbas, X. M. Wang, Q. S. Guo, Y. C. Jia, F. N. Xia, R. Weihrich, F. Bachhuber, F. Pielnhofer, H. Wang, R. Dhall, S. B. Cronin, M. Y. Ge, X. Fang, T. Nilges and C. W. Zhou, *Adv. Mater.*, 2015, **27**, 4423–4429.
- 79 Z. C. Zhang, L. K. Li, J. Horng, N. Z. Wang, F. Y. Yang, Y. J. Yu, Y. Zhang, G. R. Chen, K. Watanabe, T. Taniguchi, X. H. Chen, F. Wang and Y. B. Zhang, *Nano Lett.*, 2017, **17**, 6097–6103.
- 80 Y. P. Liu, Z. Z. Qiu, A. Carvalho, Y. Bao, H. Xu, S. J. R. Tan, W. Liu, A. H. C. Neto, K. P. Loh and J. Lu, *Nano Lett.*, 2017, **17**, 1970–1977.
- 81 A. S. Rodin, A. Carvalho and A. H. Castro Neto, *Phys. Rev. Lett.*, 2014, **112**, 176801.
- 82 Z. J. Xiang, G. J. Ye, C. Shang, B. Lei, N. Z. Wang, K. S. Yang, D. Y. Liu, F. B. Meng, X. G. Luo, L. J. Zou, Z. Sun, Y. Zhang and X. H. Chen, *Phys. Rev. Lett.*, 2015, **115**, 186403.
- 83 J. Quereda, P. San-Jose, V. Parente, L. Vaquero-Garzon, A. J. Molina-Mendoza, N. Agrait, G. Rubio-Bollinger, F. Guinea, R. Roldan and A. Castellanos-Gomez, *Nano Lett.*, 2016, **16**, 2931–2937.
- 84 Y. Li, S. X. Yang and J. B. Li, *J. Phys. Chem. C*, 2014, **118**, 23970–23976.
- 85 K. Dolui and S. Y. Quek, *Sci. Rep.*, 2015, **5**, 11699.
- 86 Q. H. Liu, X. W. Zhang, L. B. Abdalla, A. Fazio and A. Zunger, *Nano Lett.*, 2015, **15**, 1222–1228.
- 87 M. Q. Huang, M. L. Wang, C. Chen, Z. W. Ma, X. F. Li, J. B. Han and Y. Q. Wu, *Adv. Mater.*, 2016, **28**, 3481–3485.
- 88 J. Wu, G. K. W. Koon, D. Xiang, C. Han, C. T. Toh, E. S. Kulkarni, I. Verzhbitskiy, A. Carvalho, A. S. Rodin, S. P. Koenig, G. Eda, W. Chen, A. H. C. Neto and B. Ozyilmaz, *ACS Nano*, 2015, **9**, 8070–8077.
- 89 J. D. Wood, S. A. Wells, D. Jariwala, K. S. Chen, E. Cho, V. K. Sangwan, X. L. Liu, L. J. Lauhon, T. J. Marks and M. C. Hersam, *Nano Lett.*, 2014, **14**, 6964–6970.
- 90 D. Hanlon, C. Backes, E. Doherty, C. S. Cucinotta, N. C. Berner, C. Boland, K. Lee, A. Harvey, P. Lynch, Z. Gholamvand, S. F. Zhang, K. P. Wang, G. Moynihan, A. Pokle, Q. M. Ramasse, N. McEvoy, W. J. Blau, J. Wang, G. Abellan, F. Hauke, A. Hirsch, S. Sanvito, D. D. O'Regan, G. S. Duesberg, V. Nicolosi and J. N. Coleman, *Nat. Commun.*, 2015, **6**, 8563.
- 91 B. C. Yang, B. S. Wan, Q. H. Zhou, Y. Wang, W. T. Hu, W. M. Lv, Q. Chen, Z. M. Zeng, F. S. Wen, J. Y. Xiang, S. J. Yuan, J. L. Wang, B. S. Zhang, W. H. Wang, J. Y. Zhang, B. Xu, Z. S. Zhao, Y. J. Tian and Z. Y. Liu, *Adv. Mater.*, 2016, **28**, 9408–9415.
- 92 J. Jia, S. K. Jang, S. Lai, J. Xu, Y. J. Choi, J. H. Park and S. Lee, *ACS Nano*, 2015, **9**, 8729–8736.
- 93 A. Favron, E. Gaufres, F. Fossard, A. L. Phaneuf-L'Heureux, N. Y. W. Tang, P. L. Levesque, A. Loiseau, R. Leonelli, S. Francoeur and R. Martel, *Nat. Mater.*, 2015, **14**, 826–832.
- 94 J. S. Miao, B. Song, Z. H. Xu, L. Cai, S. M. Zhang, L. X. Dong and C. Wang, *Small*, 2018, **14**, 1702082.
- 95 X. L. Chen, X. B. Lu, B. C. Deng, O. Sinai, Y. C. Shao, C. Li, S. F. Yuan, V. Tran, K. Watanabe, T. Taniguchi, D. Naveh, L. Yang and F. N. Xia, *Nat. Commun.*, 2017, **8**, 1672.
- 96 C. R. Ryder, J. D. Wood, S. A. Wells, Y. Yang, D. Jariwala, T. J. Marks, G. C. Schatz and M. C. Hersam, *Nat. Chem.*, 2016, **8**, 597–602.
- 97 J. J. Pei, X. Gai, J. Yang, X. B. Wang, Z. F. Yu, D. Y. Choi, B. Luther-Davies and Y. R. Lu, *Nat. Commun.*, 2016, **7**, 10450.
- 98 S. Walia, Y. Sabri, T. Ahmed, M. R. Field, R. Ramanathan, A. Arash, S. K. Bhargava, S. Sriram, M. Bhaskaran, V. Bansal and S. Balendhran, *2D Mater.*, 2017, **4**, 015025.
- 99 Y. Y. Illarionov, M. Walzl, G. Rzepa, J. S. Kim, S. Kim, A. Dodabalapur, D. Akinwande and T. Grasser, *ACS Nano*, 2016, **10**, 9543–9549.
- 100 P. H. Ho, M. K. Li, R. Sankar, F. Y. Shih, S. S. Li, Y. R. Chang, W. H. Wang, F. C. Chou and C. W. Chen, *ACS Photonics*, 2016, **3**, 1102–1108.
- 101 Y. Liu, B. N. Shivananju, Y. S. Wang, Y. P. Zhang, W. Z. Yu, S. Xiao, T. Sun, W. L. Ma, H. R. Mu, S. H. Lin, H. Zhang,

- Y. R. Lu, C. W. Qiu, S. J. Li and Q. L. Bao, *ACS Appl. Mater. Interfaces*, 2017, **9**, 36137–36145.
- 102 Y. Son, D. Kozawa, A. T. Liu, V. B. Koman, Q. H. Wang and M. S. Strano, *2D Mater.*, 2017, **4**, 025091.
- 103 V. V. Korolkov, I. G. Timokhin, R. Haubrichs, E. F. Smith, L. X. Yang, S. H. Yang, N. R. Champness, M. Schroder and P. H. Beton, *Nat. Commun.*, 2017, **8**, 1385.
- 104 S. Walia, S. Balendhran, T. Ahmed, M. Singh, C. El-Badawi, M. D. Brennan, P. Weerathunge, M. N. Karim, F. Rahman, A. Russell, J. Duckworth, R. Ramanathan, G. E. Collis, C. J. Lobo, M. Toth, J. C. Kotsakidis, B. Weber, M. Fuhrer, J. M. Dominguez-Vera, M. J. S. Spencer, I. Aharonovich, S. Sriram, M. Bhaskaran and V. Bansal, *Adv. Mater.*, 2017, **29**, 1700152.
- 105 Q. K. Zhang, Y. A. Liu, J. W. Lai, S. M. Qi, C. H. An, Y. Lu, X. X. Duan, W. Pang, D. H. Zhang, D. Sun, J. H. Chen and J. Liu, *2D Mater.*, 2018, **5**, 025012.
- 106 Z. N. Guo, S. Chen, Z. Z. Wang, Z. Y. Yang, F. Liu, Y. H. Xu, J. H. Wang, Y. Yi, H. Zhang, L. Liao, P. K. Chu and X. F. Yu, *Adv. Mater.*, 2017, **29**, 1703811.
- 107 C. Wang, Q. Y. He, U. Halim, Y. Y. Liu, E. B. Zhu, Z. Y. Lin, H. Xiao, X. D. Duan, Z. Y. Feng, R. Cheng, N. O. Weiss, G. J. Ye, Y. C. Huang, H. Wu, H. C. Cheng, I. Shakir, L. Liao, X. H. Chen, W. A. Goddard, Y. Huang and X. F. Duan, *Nature*, 2018, **555**, 231–236.
- 108 J. S. Qiao, Y. Pan, F. Yang, C. Wang, Y. Chai and W. Ji, *Sci. Bull.*, 2018, **63**, 159–168.
- 109 Z. L. Zhu, X. L. Cai, S. H. Yi, J. L. Chen, Y. W. Dai, C. Y. Niu, Z. X. Guo, M. H. Xie, F. Liu, J. H. Cho, Y. Jia and Z. Y. Zhang, *Phys. Rev. Lett.*, 2017, **119**, 106101.
- 110 Z. Zhu, C. Cai, C. Niu, C. Wang, Q. Sun, X. Han, Z. Guo and Y. Jia, 2017, arXiv:1605.03253.
- 111 Y. Wang, G. Qiu, Q. Wang, Y. Liu, Y. Du, R. Wang, W. A. Goddard, M. J. Kim, P. D. Ye and W. Wu, *Nat. Electron.*, 2018, **1**, 228–236.
- 112 Q. S. Wang, M. Safdar, K. Xu, M. Mirza, Z. X. Wang and J. He, *ACS Nano*, 2014, **8**, 7497–7505.
- 113 J. L. Chen, Y. W. Dai, Y. Q. Ma, X. Q. Dai, W. K. Ho and M. H. Xie, *Nanoscale*, 2017, **9**, 15945–15948.
- 114 Y. C. Du, G. Qiu, Y. X. Wang, M. W. Si, X. F. Xu, W. Z. Wu and P. D. D. Ye, *Nano Lett.*, 2017, **17**, 3965–3973.
- 115 K. Takeda and K. Shiraiishi, *Phys. Rev. B: Condens. Matter Mater. Phys.*, 1994, **50**, 14916–14922.
- 116 S. Cahangirov, M. Topsakal, E. Akturk, H. Sahin and S. Ciraci, *Phys. Rev. Lett.*, 2009, **102**, 236804.
- 117 Y. Xu, B. H. Yan, H. J. Zhang, J. Wang, G. Xu, P. Z. Tang, W. H. Duan and S. C. Zhang, *Phys. Rev. Lett.*, 2013, **111**, 136804.
- 118 C. Kamal and M. Ezawa, *Phys. Rev. B: Condens. Matter Mater. Phys.*, 2015, **91**, 085423.
- 119 J. P. Ji, X. F. Song, J. Z. Liu, Z. Yan, C. X. Huo, S. L. Zhang, M. Su, L. Liao, W. H. Wang, Z. H. Ni, Y. F. Hao and H. B. Zeng, *Nat. Commun.*, 2016, **7**, 13352.
- 120 X. Wu, Y. Shao, H. Liu, Z. Feng, Y. L. Wang, J. T. Sun, C. Liu, J. O. Wang, Z. L. Liu, S. Y. Zhu, Y. Q. Wang, S. X. Du, Y. G. Shi, K. Ibrahim and H. J. Gao, *Adv. Mater.*, 2017, **29**, 1605407.
- 121 F. Reis, G. Li, L. Dudy, M. Bauernfeind, S. Glass, W. Hanke, R. Thomale, J. Schafer and R. Claessen, *Science*, 2017, **357**, 287–290.
- 122 H. H. Sun, M. X. Wang, F. F. Zhu, G. Y. Wang, H. Y. Ma, Z. A. Xu, Q. Liao, Y. H. Lu, C. L. Gao, Y. Y. Li, C. H. Liu, D. Qian, D. D. Guan and J. F. Jia, *Nano Lett.*, 2017, **17**, 3035–3039.
- 123 E. Akturk, O. U. Akturk and S. Ciraci, *Phys. Rev. B: Condens. Matter Mater. Phys.*, 2016, **94**, 014115.
- 124 G. Wang, R. Pandey and S. P. Karna, *ACS Appl. Mater. Interfaces*, 2015, **7**, 11490–11496.
- 125 F. Ersan, E. Akturk and S. Ciraci, *Phys. Rev. B: Condens. Matter Mater. Phys.*, 2016, **94**, 245417.
- 126 P. Vogt, P. De Padova, C. Quaresima, J. Avila, E. Frantzeskakis, M. C. Asensio, A. Resta, B. Ealet and G. Le Lay, *Phys. Rev. Lett.*, 2012, **108**, 155501.
- 127 F. F. Zhu, W. J. Chen, Y. Xu, C. L. Gao, D. D. Guan, C. H. Liu, D. Qian, S. C. Zhang and J. F. Jia, *Nat. Mater.*, 2015, **14**, 1020–1025.
- 128 L. Tao, E. Cinquanta, D. Chiappe, C. Grazianetti, M. Fanciulli, M. Dubey, A. Molle and D. Akinwande, *Nat. Nanotechnol.*, 2015, **10**, 227–231.
- 129 S. L. Zhang, S. Y. Guo, Z. F. Chen, Y. L. Wang, H. J. Gao, J. Gomez-Herrero, P. Ares, F. Zamora, Z. Zhu and H. B. Zeng, *Chem. Soc. Rev.*, 2018, **47**, 982–1021.
- 130 S. L. Zhang, M. Q. Xie, F. Y. Li, Z. Yan, Y. F. Li, E. J. Kan, W. Liu, Z. F. Chen and H. B. Zeng, *Angew. Chem., Int. Ed.*, 2016, **55**, 1666–1669.
- 131 Y. B. Zhang, A. Rubio and G. Le Lay, *J. Phys. D: Appl. Phys.*, 2017, **50**, 053004.
- 132 L. Lu, X. Tang, R. Cao, L. M. Wu, Z. J. Li, G. H. Jing, B. Q. Dong, S. B. Lu, Y. Li, Y. J. Xiang, J. Q. Li, D. Y. Fan and H. Zhang, *Adv. Opt. Mater.*, 2017, **5**, 1700301.
- 133 P. A. Hu, L. F. Wang, M. Yoon, J. Zhang, W. Feng, X. N. Wang, Z. Z. Wen, J. C. Idrobo, Y. Miyamoto, D. B. Geohegan and K. Xiao, *Nano Lett.*, 2013, **13**, 1649–1654.
- 134 D. V. Rybkovskiy, N. R. Arutyunyan, A. S. Orekhov, I. A. Gromchenko, I. V. Vorobiev, A. V. Osadchy, E. Y. Salaev, T. K. Baykara, K. R. Allakhverdiev and E. D. Obraztsova, *Phys. Rev. B: Condens. Matter Mater. Phys.*, 2011, **84**, 085314.
- 135 Z. X. Wang, K. Xu, Y. C. Li, X. Y. Zhan, M. Safdar, Q. S. Wang, F. M. Wang and J. He, *ACS Nano*, 2014, **8**, 4859–4865.
- 136 B. J. Carey, J. Z. Ou, R. M. Clark, K. J. Berean, A. Zavabeti, A. S. R. Chesman, S. P. Russo, D. W. M. Lau, Z. Q. Xu, Q. L. Bao, O. Kevehei, B. C. Gibson, M. D. Dickey, R. B. Kaner, T. Daeneke and K. Kalantar-Zadeh, *Nat. Commun.*, 2017, **8**, 14482.
- 137 S. X. Yang, Y. Li, X. Z. Wang, N. J. Huo, J. B. Xia, S. S. Li and J. B. Li, *Nanoscale*, 2014, **6**, 2582–2587.
- 138 P. A. Hu, Z. Z. Wen, L. F. Wang, P. H. Tan and K. Xiao, *ACS Nano*, 2012, **6**, 5988–5994.
- 139 Y. B. Zhou, Y. F. Nie, Y. J. Liu, K. Yan, J. H. Hong, C. H. Jin, Y. Zhou, J. B. Yin, Z. F. Liu and H. L. Peng, *ACS Nano*, 2014, **8**, 1485–1490.
- 140 H. Huang, P. Wang, Y. Q. Gao, X. D. Wang, T. Lin, J. L. Wang, L. Liao, J. L. Sun, X. J. Meng, Z. M. Huang,

- X. S. Chen and J. H. Chu, *Appl. Phys. Lett.*, 2015, **107**, 143112.
- 141 Y. F. Cao, K. M. Cai, P. G. Hu, L. X. Zhao, T. F. Yan, W. G. Luo, X. H. Zhang, X. G. Wu, K. Y. Wang and H. Z. Zheng, *Sci. Rep.*, 2015, **5**, 8130.
- 142 P. G. Hu, J. Zhang, M. N. Yoon, X. F. Qiao, X. Zhang, W. Feng, P. H. Tan, W. Zheng, J. J. Liu, X. N. Wang, J. C. Idrobo, D. B. Geohegan and K. Xiao, *Nano Res.*, 2014, **7**, 694–703.
- 143 Z. X. Wang, M. Safdar, M. Mirza, K. Xu, Q. S. Wang, Y. Huang, F. M. Wang, X. Y. Zhan and J. He, *Nanoscale*, 2015, **7**, 7252–7258.
- 144 S. J. Magorrian, V. Zolomi and V. I. Fal'ko, *Phys. Rev. B: Condens. Matter Mater. Phys.*, 2017, **96**, 079905.
- 145 J. Quereda, R. Biele, G. Rubio-Bollinger, N. Agrait, R. D'Agosta and A. Castellanos-Gomez, *Adv. Opt. Mater.*, 2016, **4**, 1939–1943.
- 146 J. D. Zhou, Q. S. Zeng, D. H. Lv, L. F. Sun, L. Niu, W. Fu, F. C. Liu, Z. X. Shen, C. H. Jin and Z. Liu, *Nano Lett.*, 2015, **15**, 6400–6405.
- 147 W. J. Ding, J. B. Zhu, Z. Wang, Y. F. Gao, D. Xiao, Y. Gu, Z. Y. Zhang and W. G. Zhu, *Nat. Commun.*, 2017, **8**, 14956.
- 148 D. A. Bandurina, A. V. Tyurnina, G. L. Yu, A. Mishchenko, V. Zolyomi, S. V. Morozov, R. K. Kumar, R. V. Gorbachev, Z. R. Kudrynskiy, S. Pezzini, Z. D. Kovalyuk, U. Zeitler, K. S. Novoselov, A. Patane, L. Eaves, I. V. Grigorieva, V. I. Fal'ko, A. K. Geim and Y. Cao, *Nat. Nanotechnol.*, 2017, **12**, 223–227.
- 149 N. Balakrishnan, C. R. Staddon, E. F. Smith, J. Stec, D. Gay, G. W. Mudd, O. Makarovskiy, Z. R. Kudrynskiy, Z. D. Kovalyuk, L. Eaves, A. Patane and P. H. Beton, *2D Mater.*, 2016, **3**, 025030.
- 150 C. H. Ho and Y. C. Chen, *RSC Adv.*, 2013, **3**, 24896–24899.
- 151 V. Zolyomi, N. D. Drummond and V. I. Fal'ko, *Phys. Rev. B: Condens. Matter Mater. Phys.*, 2014, **89**, 205416.
- 152 L. Debbichi, O. Eriksson and S. Lebegue, *J. Phys. Chem. Lett.*, 2015, **6**, 3098–3103.
- 153 G. Almeida, S. Dogan, G. Bertoni, C. Giannini, R. Gaspari, S. Perissinotto, R. Krahne, S. Ghosh and L. Manna, *J. Am. Chem. Soc.*, 2017, **139**, 3005–3011.
- 154 G. W. Mudd, S. A. Svatek, T. Ren, A. Patane, O. Makarovskiy, L. Eaves, P. H. Beton, Z. D. Kovalyuk, G. V. Lashkarev, Z. R. Kudrynskiy and A. I. Dmitriev, *Adv. Mater.*, 2013, **25**, 5714–5718.
- 155 Y. Li, T. M. Wang, M. Wu, T. Cao, Y. W. Chen, R. Sankar, R. K. Ulaganathan, F. C. Chou, C. Wetzel, C. Y. Xu, S. G. Louie and S. F. Shi, *2D Mater.*, 2018, **5**, 021002.
- 156 G. W. Mudd, S. A. Svatek, L. Hague, O. Makarovskiy, Z. R. Kudrynskiy, C. J. Mellor, P. H. Beton, L. Eaves, K. S. Novoselov, Z. D. Kovalyuk, E. E. Vdovin, A. J. Marsden, N. R. Wilson and A. Patane, *Adv. Mater.*, 2015, **27**, 3760–3766.
- 157 S. D. Lei, L. H. Ge, S. Najmaei, A. George, R. Koppera, J. Lou, M. Chhowalla, H. Yamaguchi, G. Gupta, R. Vajtai, A. D. Mohite and P. M. Ajayan, *ACS Nano*, 2014, **8**, 1263–1272.
- 158 S. R. Tamalampudi, Y. Y. Lu, U. R. Kumar, R. Sankar, C. D. Liao, B. K. Moorthy, C. H. Cheng, F. C. Chou and Y. T. Chen, *Nano Lett.*, 2014, **14**, 2800–2806.
- 159 W. G. Luo, Y. F. Cao, P. G. Hu, K. M. Cai, Q. Feng, F. G. Yan, T. F. Yan, X. H. Zhang and K. Y. Wang, *Adv. Opt. Mater.*, 2015, **3**, 1418–1423.
- 160 S. D. Lei, F. F. Wen, L. H. Ge, S. Najmaei, A. George, Y. J. Gong, W. L. Gao, Z. H. Jin, B. Li, J. Lou, J. Kono, R. Vajtai, P. Ajayan and N. J. Halas, *Nano Lett.*, 2015, **15**, 3048–3055.
- 161 Z. B. Yang, W. J. Jie, C. H. Mak, S. H. Lin, H. H. Lin, X. F. Yang, F. Yan, S. P. Lau and J. H. Hao, *ACS Nano*, 2017, **11**, 4225–4236.
- 162 S. D. Lei, X. F. Wang, B. Li, J. H. Kang, Y. M. He, A. George, L. H. Ge, Y. J. Gong, P. Dong, Z. H. Jin, G. Brunetto, W. B. Chen, Z. T. Lin, R. Baines, D. S. Galvao, J. Lou, E. Barrera, K. Banerjee, R. Vajtai and P. Ajayan, *Nat. Nanotechnol.*, 2016, **11**, 465–471.
- 163 W. S. Zheng, T. Xie, Y. Zhou, Y. L. Chen, W. Jiang, S. L. Zhao, J. X. Wu, Y. M. Jing, Y. Wu, G. C. Chen, Y. F. Guo, J. B. Yin, S. Y. Huang, H. Q. Xu, Z. F. Liu and H. L. Peng, *Nat. Commun.*, 2015, **6**, 6972.
- 164 R. B. Jacobs-Gedrim, M. Shanmugam, N. Jain, C. A. Durcan, M. T. Murphy, T. M. Murray, R. J. Matyi, R. L. Moore and B. Yu, *ACS Nano*, 2014, **8**, 514–521.
- 165 M. Lin, D. Wu, Y. Zhou, W. Huang, W. Jiang, W. S. Zheng, S. L. Zhao, C. H. Jin, Y. F. Guo, H. L. Peng and Z. F. Liu, *J. Am. Chem. Soc.*, 2013, **135**, 13274–13277.
- 166 J. D. Yao, Z. X. Deng, Z. Q. Zheng and G. W. Yang, *ACS Appl. Mater. Interfaces*, 2016, **8**, 20872–20879.
- 167 J. O. Island, S. I. Blanter, M. Buscema, H. S. J. van der Zant and A. Castellanos-Gomez, *Nano Lett.*, 2015, **15**, 7853–7858.
- 168 H. C. Hsueh, J. X. Li and C. H. Ho, *Adv. Opt. Mater.*, 2018, **6**, 1701194.
- 169 R. K. Ulaganathan, Y. Y. Lu, C. J. Kuo, S. R. Tamalampudi, R. Sankar, K. M. Boopathi, A. Anand, K. Yadav, R. J. Mathew, C. R. Liu, F. C. Chou and Y. T. Chen, *Nanoscale*, 2016, **8**, 2284–2292.
- 170 G. S. Shi and E. Kioupakis, *Nano Lett.*, 2015, **15**, 6926–6931.
- 171 C. Li, L. Huang, G. P. Snigdha, Y. F. Yu and L. Y. Cao, *ACS Nano*, 2012, **6**, 8868–8877.
- 172 L. Shi and Y. M. Dai, *J. Appl. Crystallogr.*, 2014, **47**, 527.
- 173 B. Mukherjee, Y. Q. Cai, H. R. Tan, Y. P. Feng, E. S. Tok and C. H. Sow, *ACS Appl. Mater. Interfaces*, 2013, **5**, 9594–9604.
- 174 D. Z. Tan, W. J. Zhang, X. F. Wang, S. Koirala, Y. Miyauchi and K. Matsuda, *Nanoscale*, 2017, **9**, 12425–12431.
- 175 P. Ramasamy, D. Kwak, D. H. Lim, H. S. Ra and J. S. Lee, *J. Mater. Chem. C*, 2016, **4**, 479–485.
- 176 J. H. Ahn, M. J. Lee, H. Heo, J. H. Sung, K. Kim, H. Hwang and M. H. Jo, *Nano Lett.*, 2015, **15**, 3703–3708.
- 177 X. Zhou, L. Gan, W. M. Tian, Q. Zhang, S. Y. Jin, H. Q. Li, Y. Bando, D. Golberg and T. Y. Zhai, *Adv. Mater.*, 2015, **27**, 8035–8041.
- 178 Y. Huang, K. Xu, Z. X. Wang, T. A. Shifa, Q. S. Wang, F. Wang, C. Jiang and J. He, *Nanoscale*, 2015, **7**, 17375–17380.
- 179 J. M. Gonzalez and I. I. Oleynik, *Phys. Rev. B: Condens. Matter Mater. Phys.*, 2016, **94**, 125443.
- 180 L. Li, Z. Chen, Y. Hu, X. W. Wang, T. Zhang, W. Chen and Q. B. Wang, *J. Am. Chem. Soc.*, 2013, **135**, 1213–1216.



- 181 T. Lorenz, J. O. Joswig and G. Seifert, *Semicond. Sci. Technol.*, 2014, **29**, 064006.
- 182 J. J. Wu, Z. L. Hu, Z. H. Jin, S. D. Lei, H. Guo, K. Chatterjee, J. Zhang, Y. C. Yang, B. Li, Y. Liu, J. W. Lai, R. Vajtai, B. Yakobson, M. Tang, J. Lou and P. M. Ajayan, *Adv. Mater. Interfaces*, 2016, **3**, 1600383.
- 183 P. Yu, X. C. Yu, W. L. Lu, H. Lin, L. F. Sun, K. Z. Du, F. C. Liu, W. Fu, Q. S. Zeng, Z. X. Shen, C. H. Jin, Q. J. Wang and Z. Liu, *Adv. Funct. Mater.*, 2016, **26**, 137–145.
- 184 M. Krishna, S. Kallatt and K. Majumdar, *Nanotechnology*, 2018, **29**, 035205.
- 185 Y. Huang, H. X. Deng, K. Xu, Z. X. Wang, Q. S. Wang, F. M. Wang, F. Wang, X. Y. Zhan, S. S. Li, J. W. Luo and J. He, *Nanoscale*, 2015, **7**, 14093–14099.
- 186 X. Zhou, Q. Zhang, L. Gan, H. Q. Li and T. Y. Zhai, *Adv. Funct. Mater.*, 2016, **26**, 4405–4413.
- 187 B. Peng, P. K. Ang and K. P. Loh, *Nano Today*, 2015, **10**, 128–137.
- 188 G. B. Liu, Z. H. Li, X. S. Chen, W. Zheng, W. Feng, M. J. Dai, D. C. Jia, Y. Zhou and P. A. Hu, *Nanoscale*, 2017, **9**, 9167–9174.
- 189 M. Patel, H. S. Kim and J. Kim, *Nanoscale*, 2017, **9**, 15804–15812.
- 190 G. Liu, Z. Li, T. Hasan, X. Chen, W. Zheng, W. Feng, D. Jia, Y. Zhou and P. A. Hu, *J. Mater. Chem. A*, 2017, **5**, 1989–1995.
- 191 J. L. Cao, Z. X. Wang, X. Y. Zhan, Q. S. Wang, M. Safdar, Y. J. Wang and J. He, *Nanotechnology*, 2014, **25**, 105705.
- 192 Y. D. Jin, X. X. Li and J. L. Yang, *Phys. Chem. Chem. Phys.*, 2015, **17**, 18665–18669.
- 193 M. Li, J. Dai and X. C. Zeng, *Nanoscale*, 2015, **7**, 15385–15391.
- 194 J. Dai, M. Li and X. C. Zeng, *WIREs Comput. Mol. Sci.*, 2016, **6**, 211–222.
- 195 J. O. Island, R. Biele, M. Barawi, J. M. Clamagirand, J. R. Ares, C. Sanchez, H. S. J. van der Zant, I. J. Ferrer, R. D'Agosta and A. Castellanos-Gomez, *Sci. Rep.*, 2016, **6**, 22214.
- 196 J. Dai and X. C. Zeng, *Angew. Chem., Int. Ed.*, 2015, **54**, 7572–7576.
- 197 K. Wu, E. Torun, H. Sahin, B. Chen, X. Fan, A. Pant, D. P. Wright, T. Aoki, F. M. Peeters, E. Soignard and S. Tongay, *Nat. Commun.*, 2016, **7**, 12952.
- 198 J. O. Island, M. Buscema, M. Barawi, J. M. Clamagirand, J. R. Ares, C. Sanchez, I. J. Ferrer, G. A. Steele, H. S. J. van der Zant and A. Castellanos-Gomez, *Adv. Opt. Mater.*, 2014, **2**, 641–645.
- 199 R. Biele, E. Flores, J. R. Ares, C. Sanchez, I. Ferrer, G. Rubio-Bollinger, A. Castellanos-Gomez and R. D'Agosta, *Nano Res.*, 2018, **11**, 225–232.
- 200 S. Liu, W. Xiao, M. Zhong, L. Pan, X. Wang, H. X. Deng, J. Liu, J. Li and Z. Wei, *Nanotechnology*, 2018, **29**, 184002.
- 201 Y. R. Tao, X. C. Wu and W. W. Xiong, *Small*, 2014, **10**, 4905–4911.
- 202 W. W. Xiong, J. Q. Chen, X. C. Wu and J. J. Zhu, *J. Mater. Chem. C*, 2015, **3**, 1929–1934.
- 203 Y. R. Tao, J. J. Wu and X. C. Wu, *Nanoscale*, 2015, **7**, 14292–14298.
- 204 J. P. Heremans, R. J. Cava and N. Samarth, *Nat. Rev. Mater.*, 2017, **2**, 17049.
- 205 S. M. Elahi, A. Taghizadeh, A. Hadizadeh and L. Dejam, *Int. J. Thin Film Sci. Technol.*, 2014, **3**, 13–18.
- 206 Y. Zhang, K. He, C. Z. Chang, C. L. Song, L. L. Wang, X. Chen, J. F. Jia, Z. Fang, X. Dai, W. Y. Shan, S. Q. Shen, Q. A. Niu, X. L. Qi, S. C. Zhang, X. C. Ma and Q. K. Xue, *Nat. Phys.*, 2010, **6**, 584–588.
- 207 R. Vogel, P. Hoyer and H. Weller, *J. Phys. Chem.*, 1994, **98**, 3183–3188.
- 208 M. Nair and P. Nair, *Semicond. Sci. Technol.*, 1990, **5**, 1225–1230.
- 209 H. J. Zhang, C. X. Liu, X. L. Qi, X. Dai, Z. Fang and S. C. Zhang, *Nat. Phys.*, 2009, **5**, 438–442.
- 210 Y. Xia, D. Qian, D. Hsieh, L. Wray, A. Pal, H. Lin, A. Bansil, D. Grauer, Y. S. Hor, R. J. Cava and M. Z. Hasan, *Nat. Phys.*, 2009, **5**, 398–402.
- 211 Y. L. Chen, J. G. Analytis, J. H. Chu, Z. K. Liu, S. K. Mo, X. L. Qi, H. J. Zhang, D. H. Lu, X. Dai, Z. Fang, S. C. Zhang, I. R. Fisher, Z. Hussain and Z. X. Shen, *Science*, 2009, **325**, 178–181.
- 212 X. L. Qi and S. C. Zhang, *Phys. Today*, 2010, **63**, 33–38.
- 213 H. Qiao, J. Yuan, Z. Q. Xu, C. Y. Chen, S. H. Lin, Y. S. Wang, J. C. Song, Y. Liu, Q. Khan, H. Y. Hoh, C. X. Pan, S. J. Li and Q. L. Bao, *ACS Nano*, 2015, **9**, 1886–1894.
- 214 J. Kim, V. Park, H. Jang, N. Koirala, J. B. Lee, U. J. Kim, H. S. Lee, Y. G. Roh, H. Lee, S. Sim, S. Cha, C. In, J. Park, J. Lee, M. Noh, J. Moon, M. Salehi, J. Sung, S. S. Chee, M. H. Ham, M. H. Jo, S. Oh, J. H. Ahn, S. W. Hwang, D. Kim and H. Choi, *ACS Photonics*, 2017, **4**, 482–488.
- 215 H. B. Zhang, X. J. Zhang, C. Liu, S. T. Lee and J. S. Jie, *ACS Nano*, 2016, **10**, 5113–5122.
- 216 J. J. Liu, Y. Y. Li, Y. X. Song, Y. J. Ma, Q. M. Chen, Z. Y. S. Zhu, P. F. Lu and S. M. Wang, *Appl. Phys. Lett.*, 2017, **110**, 141109.
- 217 K. W. Mauser, S. Kim, S. Mitrovic, D. Fleischman, R. Pala, K. C. Schwab and H. A. Atwater, *Nat. Nanotechnol.*, 2017, **12**, 770–775.
- 218 L. Viti, D. Coquillat, A. Politano, K. A. Kokh, Z. S. Aliev, M. B. Babanly, O. E. Tereshchenko, W. Knap, E. V. Chulkov and M. S. Vitiello, *Nano Lett.*, 2016, **16**, 80–87.
- 219 C. H. Park and S. G. Louie, *Phys. Rev. Lett.*, 2012, **109**, 097601.
- 220 A. A. Reijnders, Y. Tian, L. J. Sandilands, G. Pohl, I. D. Kivlichan, S. Y. F. Zhao, S. Jia, M. E. Charles, R. J. Cava, N. Alidoust, S. Y. Xu, M. Neupane, M. Z. Hasan, X. Wang, S. W. Cheong and K. S. Burch, *Phys. Rev. B: Condens. Matter Mater. Phys.*, 2014, **89**, 075138.
- 221 K. W. Post, B. C. Chapler, M. K. Liu, J. S. Wu, H. T. Stinson, M. D. Goldflam, A. R. Richardella, J. S. Lee, A. A. Reijnders, K. S. Burch, M. M. Fogler, N. Samarth and D. N. Basov, *Phys. Rev. Lett.*, 2015, **115**, 116804.
- 222 R. V. Aguilar, A. V. Stier, W. Liu, L. S. Bilbro, D. K. George, N. Bansal, L. Wu, J. Cerne, A. G. Markelz, S. Oh and N. P. Armitage, *Phys. Rev. Lett.*, 2012, **108**, 087403.
- 223 W. S. Whitney, V. W. Brar, Y. B. Ou, Y. M. Shao, A. R. Davoyan, D. N. Basov, K. He, Q. K. Xue and H. A. Atwater, *Nano Lett.*, 2017, **17**, 255–260.

- 224 X. D. Li, Y. G. Semenov and K. W. Kim, *Appl. Phys. Lett.*, 2014, **104**, 061116.
- 225 N. H. Lindner, A. Farrell, E. Lustig, F. v. Oppen and G. Refael, 2014, arXiv:1403.0010.
- 226 J. W. McIver, D. Hsieh, H. Steinberg, P. Jarillo-Herrero and N. Gedik, *Nat. Nanotechnol.*, 2012, **7**, 96–100.
- 227 P. Hosur, *Phys. Rev. B: Condens. Matter Mater. Phys.*, 2011, **83**, 035309.
- 228 H. T. Yuan, X. Q. Wang, B. Lian, H. J. Zhang, X. F. Fang, B. Shen, G. Xu, Y. Xu, S. C. Zhang, H. Y. Hwang and Y. Cui, *Nat. Nanotechnol.*, 2014, **9**, 851–857.
- 229 Y. N. Xu and W. Y. Ching, *Phys. Rev. B: Condens. Matter Mater. Phys.*, 1991, **44**, 7787–7798.
- 230 X. Blase and A. Rubio, *Phys. Rev. B: Condens. Matter Mater. Phys.*, 1995, **51**, 6868–6875.
- 231 B. Arnaud, S. Lebegue, P. Rabiller and M. Alouani, *Phys. Rev. Lett.*, 2006, **96**, 026402.
- 232 K. Watanabe, T. Taniguchi and H. Kanda, *Nat. Mater.*, 2004, **3**, 404–409.
- 233 G. Cassabois, P. Valvin and B. Gil, *Nat. Photonics*, 2016, **10**, 262–266.
- 234 Y. Kubota, K. Watanabe, O. Tsuda and T. Taniguchi, *Science*, 2007, **317**, 932–934.
- 235 K. Watanabe, T. Taniguchi, T. Niiyama, K. Miya and M. Taniguchi, *Nat. Photonics*, 2009, **3**, 591–594.
- 236 R. Dahal, J. Li, S. Majety, B. N. Pantha, X. K. Cao, J. Y. Lin and H. X. Jiang, *Appl. Phys. Lett.*, 2011, **98**, 211110.
- 237 J. Li, S. Majety, R. Dahal, W. P. Zhao, J. Y. Lin and H. X. Jiang, *Appl. Phys. Lett.*, 2012, **101**, 171112.
- 238 A. Aldalbahi and P. Feng, *IEEE Trans. Electron Devices*, 2015, **62**, 1885–1890.
- 239 M. Sajjad, W. M. Jadwisieniczak and P. Feng, *Nanoscale*, 2014, **6**, 15346.
- 240 A. F. Zhou, A. Aldalbahi and P. Feng, *Opt. Mater. Express*, 2016, **6**, 3286–3292.
- 241 M. Rivera, R. Velazquez, A. Aldalbahi, A. F. Zhou and P. Feng, *Sci. Rep.*, 2017, **7**, 42973.
- 242 H. Y. Cun, A. Hemmi, E. Miniussi, C. Bernard, B. Probst, K. Liu, D. T. L. Alexander, A. Kleibert, G. Mette, M. Weini, M. Schreck, J. Osterwalder, A. Radenovic and T. Greber, *Nano Lett.*, 2018, **18**, 1205–1212.
- 243 K. L. Zhang, Y. L. Feng, F. Wang, Z. C. Yang and J. Wang, *J. Mater. Chem. C*, 2017, **5**, 11992–12022.
- 244 H. L. Wang, X. W. Zhang, H. Liu, Z. G. Yin, J. H. Meng, J. Xia, X. M. Meng, J. L. Wu and J. B. You, *Adv. Mater.*, 2015, **27**, 8109–8115.
- 245 T. Low, A. Chaves, J. D. Caldwell, A. Kumar, N. X. Fang, P. Avouris, T. F. Heinz, F. Guinea, L. Martin-Moreno and F. Koppens, *Nat. Mater.*, 2017, **16**, 182–194.
- 246 J. D. Caldwell, A. V. Kretinin, Y. G. Chen, V. Giannini, M. M. Fogler, Y. Francescato, C. T. Ellis, J. G. Tischler, C. R. Woods, A. J. Giles, M. Hong, K. Watanabe, T. Taniguchi, S. A. Maier and K. S. Novoselov, *Nat. Commun.*, 2014, **5**, 5221.
- 247 A. J. Giles, S. Y. Dai, I. Vurgaftman, T. H. Man, S. Liu, L. Lindsay, C. T. Ellis, N. Assefa, I. Chatzakis, T. L. Reinecke, J. G. Tischler, M. M. Fogler, J. H. Edgar, D. N. Basov and J. D. Caldwell, *Nat. Mater.*, 2018, **17**, 134–139.
- 248 S. Dai, Q. Ma, T. Andersen, A. S. Mcleod, Z. Fei, M. K. Liu, M. Wagner, K. Watanabe, T. Taniguchi, M. Thiemens, F. Keilmann, P. Jarillo-Herrero, M. M. Fogler and D. N. Basov, *Nat. Commun.*, 2015, **6**, 6963.
- 249 P. N. Li, M. Lewin, A. V. Kretinin, J. D. Caldwell, K. S. Novoselov, T. Taniguchi, K. Watanabe, F. Gaussmann and T. Taubner, *Nat. Commun.*, 2015, **6**, 7507.
- 250 S. T. Ha, X. F. Liu, Q. Zhang, D. Giovanni, T. C. Sum and Q. H. Xiong, *Adv. Opt. Mater.*, 2014, **2**, 838–844.
- 251 H. C. Cheng, G. M. Wang, D. H. Li, Q. Y. He, A. X. Yin, Y. Liu, H. Wu, M. N. Ding, Y. Huang and X. F. Duan, *Nano Lett.*, 2016, **16**, 367–373.
- 252 G. M. Wang, D. H. Li, H. C. Cheng, Y. J. Li, C. Y. Chen, A. X. Yin, Z. P. Zhao, Z. Y. Lin, H. Wu, Q. Y. He, M. N. Ding, Y. Liu, Y. Huang and X. F. Duan, *Sci. Adv.*, 2015, **1**, e1500613.
- 253 F. Lu, W. C. Wang, X. G. Luo, X. J. Xie, Y. H. Cheng, H. Dong, H. Liu and W. H. Wang, *Appl. Phys. Lett.*, 2016, **108**, 132104.
- 254 W. Zheng, Z. J. Zhang, R. C. Lin, K. Xu, J. He and F. Huang, *Adv. Electron. Mater.*, 2016, **2**, 1600291.
- 255 Y. G. Wang, L. Gan, J. N. Chen, R. Yang and T. Y. Zhai, *Sci. Bull.*, 2017, **62**, 1654–1662.
- 256 C. Lan, R. Dong, Z. Zhou, L. Shu, D. Li, S. Yip and J. C. Ho, *Adv. Mater.*, 2017, **29**, 1702759.
- 257 M. A. Susner, M. Chyasnachichyus, M. A. McGuire, P. Ganesh and P. Maksymovych, *Adv. Mater.*, 2017, **29**.
- 258 X. Zhang, X. D. Zhao, D. H. Wu, Y. Jing and Z. Zhou, *Adv. Sci.*, 2016, **3**, 1600062.
- 259 X. X. Li, X. J. Wu and J. L. Yang, *J. Am. Chem. Soc.*, 2014, **136**, 11065–11069.
- 260 K. Z. Du, X. Z. Wang, Y. Liu, P. Hu, M. I. B. Utama, C. K. Gan, Q. H. Xiong and C. Kloc, *ACS Nano*, 2016, **10**, 1738–1743.
- 261 F. M. Wang, T. A. Shifa, P. He, Z. Z. Cheng, J. W. Chu, Y. Liu, Z. X. Wang, F. Wang, Y. Wen, L. R. Liang and J. He, *Nano Energy*, 2017, **40**, 673–680.
- 262 J. W. Chu, F. M. Wang, L. Yin, L. Lei, C. Y. Yan, F. Wang, Y. Wen, Z. X. Wang, C. Jiang, L. P. Feng, J. Xiong, Y. R. Li and J. He, *Adv. Funct. Mater.*, 2017, **27**, 1701342.
- 263 B. L. Chittari, Y. Park, D. Lee, M. Han, A. H. MacDonald, E. Hwang and J. Jung, *Phys. Rev. B: Condens. Matter Mater. Phys.*, 2016, **94**, 184428.
- 264 J. U. Lee, S. Lee, J. H. Ryoo, S. Kang, T. Y. Kim, P. Kim, C. H. Park, J. G. Park and H. Cheong, *Nano Lett.*, 2016, **16**, 7433–7438.
- 265 T. R. Waters, V. Putzanderson, A. Garg and L. J. Fine, *J. Solid State Chem.*, 2015, **226**, 219–223.
- 266 X. Zhang, Y. F. Liu, G. H. Zhang, Y. Q. Wang, H. Zhang and F. Q. Huang, *ACS Appl. Mater. Interfaces*, 2015, **7**, 4442–4448.
- 267 J. X. Wu, Y. J. Liu, Z. J. Tan, C. W. Tan, J. B. Yin, T. R. Li, T. Tu and H. L. Peng, *Adv. Mater.*, 2017, **29**, 1704060.
- 268 J. X. Wu, C. W. Tan, Z. J. Tan, Y. J. Liu, J. B. Yin, W. H. Dang, M. Z. Wang and H. L. Peng, *Nano Lett.*, 2017, **17**, 3021–3026.

- 269 J. Li, Z. X. Wang, Y. Wen, J. W. Chu, L. Yin, R. Q. Cheng, L. Lei, P. He, C. Jiang, L. P. Feng and J. He, *Adv. Funct. Mater.*, 2018, **28**, 1706437.
- 270 J. Yin, Z. Tan, H. Hong, J. Wu, H. Yuan, Y. Liu, C. Chen, C. Tan, F. Yao and Y. Chen, 2017, arXiv:1712.05942.
- 271 S. Ithurria, M. D. Tessier, B. Mahler, R. P. S. M. Lobo, B. Dubertret and A. Efros, *Nat. Mater.*, 2011, **10**, 936–941.
- 272 Z. Xie, C. Xing, W. Huang, T. Fan, Z. Li, J. Zhao, Y. Xiang, Z. Guo, J. Li, Z. Yang, B. Dong, J. Qu, D. Fan and H. Zhang, *Adv. Funct. Mater.*, 2018, 1705833.
- 273 C. Xing, Z. Xie, Z. Liang, W. Liang, T. Fan, J. S. Ponraj, S. C. Dhanabalan, D. Fan and H. Zhang, *Adv. Opt. Mater.*, 2017, **5**, 1700884.
- 274 C. Tan and H. Zhang, *Nat. Commun.*, 2015, **6**, 7873.
- 275 Z. Sun, T. Liao, Y. Dou, S. M. Hwang, M. S. Park, L. Jiang, J. H. Kim and S. X. Dou, *Nat. Commun.*, 2014, **5**, 3813.
- 276 F. Wang, J. H. Seo, G. Luo, M. B. Starr, Z. Li, D. Geng, X. Yin, S. Wang, D. G. Fraser, D. Morgan, Z. Ma and X. Wang, *Nat. Commun.*, 2016, **7**, 10444.
- 277 A. Zavabeti, J. Z. Ou, B. J. Carey, N. Syed, R. Orrell-Trigg, E. L. H. Mayes, C. Xu, O. Kavehei, A. P. O'Mullane, R. B. Kaner, K. Kalantar-Zadeh and T. Daeneke, *Science*, 2017, **358**, 332–335.
- 278 W. Feng, W. Zheng and P. Hu, *Phys. Chem. Chem. Phys.*, 2014, **16**, 19340–19344.
- 279 W. Feng, X. Wang, J. Zhang, L. Wang, W. Zheng, P. Hu, W. Cao and B. Yang, *J. Mater. Chem. C*, 2014, **2**, 3254–3259.
- 280 M. I. Utama, Q. Zhang, J. Zhang, Y. Yuan, F. J. Belarre, J. Arbiol and Q. Xiong, *Nanoscale*, 2013, **5**, 3570–3588.
- 281 Q. Wang, M. Safdar, K. Xu, M. Mirza, Z. Wang and J. He, *ACS Nano*, 2014, **8**, 7497–7505.
- 282 Q. Wang, K. Xu, Z. Wang, F. Wang, Y. Huang, M. Safdar, X. Zhan, F. Wang, Z. Cheng and J. He, *Nano Lett.*, 2015, **15**, 1183–1189.
- 283 J. Kim, C. Bayram, H. Park, C. W. Cheng, C. Dimitrakopoulos, J. A. Ott, K. B. Reuter, S. W. Bedell and D. K. Sadana, *Nat. Commun.*, 2014, **5**, 4836.
- 284 Y. Wen, Q. Wang, L. Yin, Q. Liu, F. Wang, F. Wang, Z. Wang, K. Liu, K. Xu, Y. Huang, T. A. Shifa, C. Jiang, J. Xiong and J. He, *Adv. Mater.*, 2016, **28**, 8051–8057.
- 285 W. Zheng, W. Feng, X. Zhang, X. Chen, G. Liu, Y. Qiu, T. Hasan, P. Tan and P. A. Hu, *Adv. Funct. Mater.*, 2016, **26**, 2648–2654.
- 286 R. Cheng, Y. Wen, L. Yin, F. Wang, F. Wang, K. Liu, T. A. Shifa, J. Li, C. Jiang, Z. Wang and J. He, *Adv. Mater.*, 2017, **29**, 1703122.
- 287 J. Xia, Y. X. Zhao, L. Wang, X. Z. Li, Y. Y. Gu, H. Q. Cheng and X. M. Meng, *Nanoscale*, 2017, **9**, 13786–13793.
- 288 Y. Zhao, M. Boccard, S. Liu, J. Becker, X.-H. Zhao, C. M. Campbell, E. Suarez, M. B. Lassise, Z. Holman and Y.-H. Zhang, *Nat. Energy*, 2016, **1**, 16067.
- 289 D. D. Zhu, J. Xia, L. Wang, X. Z. Li, L. F. Tian and X. M. Meng, *Nanoscale*, 2016, **8**, 11375–11379.
- 290 Q. Wang, Y. Wen, F. Yao, Y. Huang, Z. Wang, M. Li, X. Zhan, K. Xu, F. Wang, F. Wang, J. Li, K. Liu, C. Jiang, F. Liu and J. He, *Small*, 2015, **11**, 5388–5394.
- 291 C. Schliehe, B. H. Juarez, M. Pelletier, S. Jander, D. Greshnykh, M. Nagel, A. Meyer, S. Foerster, A. Kornowski, C. Klinke and H. Weller, *Science*, 2010, **329**, 550–553.
- 292 Z. Y. Al Balushi, K. Wang, R. K. Ghosh, R. A. Vila, S. M. Eichfeld, J. D. Caldwell, X. Qin, Y. C. Lin, P. A. DeSario, G. Stone, S. Subramanian, D. F. Paul, R. M. Wallace, S. Datta, J. M. Redwing and J. A. Robinson, *Nat. Mater.*, 2016, **15**, 1166–1171.
- 293 S. T. Ha, X. Liu, Q. Zhang, D. Giovanni, T. C. Sum and Q. Xiong, *Adv. Opt. Mater.*, 2014, **2**, 838–844.
- 294 J. Liu, Y. Xue, Z. Wang, Z. Q. Xu, C. Zheng, B. Weber, J. Song, Y. Wang, Y. Lu, Y. Zhang and Q. Bao, *ACS Nano*, 2016, **10**, 3536–3542.
- 295 L. Dou, A. B. Wong, Y. Yu, M. Lai, N. Kornienko, S. W. Eaton, A. Fu, C. G. Bischak, J. Ma, T. Ding, N. S. Ginsberg, L. W. Wang, A. P. Alivisatos and P. Yang, *Science*, 2015, **349**, 1518–1521.
- 296 L. Lv, Y. Xu, H. Fang, W. Luo, F. Xu, L. Liu, B. Wang, X. Zhang, D. Yang, W. Hu and A. Dong, *Nanoscale*, 2016, **8**, 13589–13596.
- 297 J. Song, L. Xu, J. Li, J. Xue, Y. Dong, X. Li and H. Zeng, *Adv. Mater.*, 2016, **28**, 4861–4869.
- 298 Z. Tan, Y. Wu, H. Hong, J. Yin, J. Zhang, L. Lin, M. Wang, X. Sun, L. Sun, Y. Huang, K. Liu, Z. Liu and H. Peng, *J. Am. Chem. Soc.*, 2016, **138**, 16612–16615.
- 299 K. Xu, L. Yin, Y. Huang, T. A. Shifa, J. W. Chu, F. Wang, R. Q. Cheng, Z. X. Wang and J. He, *Nanoscale*, 2016, **8**, 16802–16818.
- 300 J. L. Wang, H. H. Fang, X. D. Wang, X. S. Chen, W. Lu and W. D. Hu, *Small*, 2017, **13**, 1700894.
- 301 D. Jariwala, T. J. Marks and M. C. Hersam, *Nat. Mater.*, 2017, **16**, 170–181.
- 302 Y. X. Deng, Z. Luo, N. J. Conrad, H. Liu, Y. J. Gong, S. Najmaei, P. M. Ajayan, J. Lou, X. F. Xu and P. D. Ye, *ACS Nano*, 2014, **8**, 8292–8299.
- 303 T. Hong, B. Chamlagain, T. J. Wang, H. J. Chuang, Z. X. Zhou and Y. Q. Xu, *Nanoscale*, 2015, **7**, 18537–18541.
- 304 L. Ye, H. Li, Z. F. Chen and J. B. Xu, *ACS Photonics*, 2016, **3**, 692–699.
- 305 J. Jia, S. Jeon, J. Jeon, J. Xu, Y. J. Song, J. H. Cho, B. H. Lee, J. D. Song, H. J. Kim, E. Hwang and S. Lee, *Small*, 2018, **14**, 1703065.
- 306 F. G. Yan, L. X. Zhao, A. L. Patane, P. A. Hu, X. Wei, W. G. Luo, D. Zhang, Q. S. Lv, Q. Feng, C. Shen, K. Chang, L. Eaves and K. Y. Wang, *Nanotechnology*, 2017, **28**, 27LT01.
- 307 Z. S. Chen, J. Biscaras and A. Shukla, *Nanoscale*, 2015, **7**, 5981–5986.
- 308 X. F. Li, M. W. Lin, J. H. Lin, B. Huang, A. A. Puretzky, C. Ma, K. Wang, W. Zhou, S. T. Pantelides, M. F. Chi, I. Kravchenko, J. Fowlkes, C. M. Rouleau, D. B. Geohegan and K. Xiao, *Sci. Adv.*, 2016, **2**(4), e1501882.
- 309 R. T. Lu, J. W. Liu, H. F. Luo, V. Chikan and J. Z. Wu, *Sci. Rep.*, 2016, **6**, 19161.
- 310 X. Yuan, L. Tang, S. S. Liu, P. Wang, Z. G. Chen, C. Zhang, Y. W. Liu, W. Y. Wang, Y. C. Zou, C. Liu, N. Guo, J. Zou,



- P. Zhou, W. D. Hu and F. X. Xiu, *Nano Lett.*, 2015, **15**, 3571–3577.
- 311 F. Wang, Z. X. Wang, K. Xu, F. M. Wang, Q. S. Wang, Y. Huang, L. Yin and J. He, *Nano Lett.*, 2015, **15**, 7558–7566.
- 312 S. X. Yang, C. Wang, C. Ataca, Y. Li, H. Chen, H. Cai, A. Suslu, J. C. Grossman, C. B. Jiang, Q. Liu and S. Tongay, *ACS Appl. Mater. Interfaces*, 2016, **8**, 2533–2539.
- 313 S. S. Liu, X. Yuan, P. Wang, Z. G. Chen, L. Tang, E. Z. Zhang, C. Zhang, Y. W. Liu, W. Y. Wang, C. Liu, C. Chen, J. Zou, W. D. Hu and F. X. Xiu, *ACS Nano*, 2015, **9**, 8592–8598.
- 314 A. S. Aji, M. Izumoto, K. Suenaga, K. Yamamoto, H. Nakashima and H. Ago, *Phys. Chem. Chem. Phys.*, 2018, **20**, 889–897.
- 315 X. Zhou, X. Z. Hu, S. S. Zhou, H. Y. Song, Q. Zhang, L. J. Pi, L. Li, H. Q. Li, J. T. Lu and T. Y. Zhai, *Adv. Mater.*, 2018, **30**, 1703286.
- 316 T. F. Yang, B. Y. Zheng, Z. Wang, T. Xu, C. Pan, J. Zou, X. H. Zhang, Z. Y. Qi, H. J. Liu, Y. X. Feng, W. D. Hu, F. Miao, L. T. Sun, X. F. Duan and A. L. Pan, *Nat. Commun.*, 2017, **8**, 1906.
- 317 Y. Wang, W. X. Zhou, L. Huang, C. X. Xia, L. M. Tang, H. X. Deng, Y. T. Li, K. Q. Chen, J. B. Li and Z. M. Wei, *2D Mater.*, 2017, **4**, 025097.
- 318 Y. Huang, X. Y. Zhan, K. Xu, L. Yin, Z. Z. Cheng, C. Jiang, Z. X. Wang and J. He, *Appl. Phys. Lett.*, 2016, **108**, 013101.
- 319 S. X. Yang, M. H. Wu, B. Wang, L. D. Zhao, L. Huang, C. B. Jiang and S. H. Wei, *ACS Appl. Mater. Interfaces*, 2017, **9**, 42149–42155.
- 320 J. D. Yao, Z. Q. Zheng and G. W. Yang, *J. Mater. Chem. C*, 2016, **4**, 7831–7840.
- 321 J. D. Yao, J. M. Shao, Y. X. Wang, Z. R. Zhao and G. W. Yang, *Nanoscale*, 2015, **7**, 12535–12541.
- 322 G. Eda and S. A. Maier, *ACS Nano*, 2013, **7**, 5660–5665.
- 323 W. J. Zhang, Q. X. Wang, Y. Chen, Z. Wang and A. T. S. Wee, *2D Mater.*, 2016, **3**, 2.
- 324 A. Castellanos-Gomez, *Nat. Photonics*, 2016, **10**, 202–204.
- 325 Q. H. Wang, K. Kalantar-Zadeh, A. Kis, J. N. Coleman and M. S. Strano, *Nat. Nanotechnol.*, 2012, **7**, 699–712.
- 326 Y. Takao and A. Morita, *Physica B+C*, 1981, **105**, 93–98.
- 327 H. Asahina, K. Shindo and A. Morita, *J. Phys. Soc. Jpn.*, 1982, **51**, 1193–1199.
- 328 Y. Akahama, S. Endo and S. Narita, *J. Phys. Soc. Jpn.*, 1983, **52**, 2148–2155.
- 329 W. Feng, Z. Jin, J. Yuan, J. Zhang, S. Jia, L. Dong, J. Yoon, L. Zhou, R. Vajtai, J. M. Tour, P. M. Ajayan, P. Hu and J. Lou, *2D Mater.*, 2018, **5**, 2.
- 330 L. Liu, J. Park, D. A. Siegel, K. F. McCarty, K. W. Clark, W. Deng, L. Basile, J. C. Idrobo, A. P. Li and G. Gu, *Science*, 2014, **343**, 163–167.
- 331 X. D. Duan, C. Wang, J. C. Shaw, R. Cheng, Y. Chen, H. L. Li, X. P. Wu, Y. Tang, Q. L. Zhang, A. L. Pan, J. H. Jiang, R. Q. Yu, Y. Huang and X. F. Duan, *Nat. Nanotechnol.*, 2014, **9**, 1024–1030.
- 332 Y. J. Gong, J. H. Lin, X. L. Wang, G. Shi, S. D. Lei, Z. Lin, X. L. Zou, G. L. Ye, R. Vajtai, B. I. Yakobson, H. Terrones, M. Terrones, B. K. Tay, J. Lou, S. T. Pantelides, Z. Liu, W. Zhou and P. M. Ajayan, *Nat. Mater.*, 2014, **13**, 1135–1142.
- 333 W. P. Sun, X. H. Rui, D. Yang, Z. Q. Sun, B. Li, W. Y. Zhang, Y. Zong, S. Madhavi, S. X. Dou and Q. Y. Yan, *ACS Nano*, 2015, **9**, 11371–11381.
- 334 Y. Huang, E. Sutter, J. T. Sadowski, M. Cotlet, O. L. A. Monti, D. A. Racke, M. R. Neupane, D. Wickramaratne, R. K. Lake, B. A. Parkinson and P. Sutter, *ACS Nano*, 2014, **8**, 10743–10755.
- 335 G. X. Su, V. G. Hadjiev, P. E. Loya, J. Zhang, S. D. Lei, S. Maharjan, P. Dong, P. M. Ajayan, J. Lou and H. B. Peng, *Nano Lett.*, 2015, **15**, 506–513.
- 336 F. X. Xiu and T. T. Zhao, *Chin. Phys. B*, 2013, **22**, 96104–96117.
- 337 M. Z. Hasan and C. L. Kane, *Rev. Mod. Phys.*, 2010, **82**, 3045–3067.
- 338 F. Wang, Z. X. Wang, C. Jiang, L. Yin, R. Q. Cheng, X. Y. Zhan, K. Xu, F. M. Wang, Y. Zhang and J. He, *Small*, 2017, **13**, 1604298.
- 339 K. Roy, M. Padmanabhan, S. Goswami, T. P. Sai, G. Ramalingam, S. Raghavan and A. Ghosh, *Nat. Nanotechnol.*, 2013, **8**, 826–830.
- 340 D. Kufer, I. Nikitskiy, T. Lasanta, G. Navickaite, F. H. L. Koppens and G. Konstantatos, *Adv. Mater.*, 2015, **27**, 176–180.
- 341 S. Kallatt, S. Nair and K. Majumdar, *Small*, 2018, **14**, 1702066.
- 342 G. Konstantatos, M. Badioli, L. Gaudreau, J. Osmond, M. Bernechea, F. P. G. de Arquer, F. Gatti and F. H. L. Koppens, *Nat. Nanotechnol.*, 2012, **7**, 363–368.
- 343 J. A. Rogers, T. Someya and Y. G. Huang, *Science*, 2010, **327**, 1603–1607.
- 344 S. I. Park, Y. J. Xiong, R. H. Kim, P. Elvikis, M. Meitl, D. H. Kim, J. Wu, J. Yoon, C. J. Yu, Z. J. Liu, Y. G. Huang, K. Hwang, P. Ferreira, X. L. Li, K. Choquette and J. A. Rogers, *Science*, 2009, **325**, 977–981.
- 345 D. H. Kim, N. S. Lu, R. Ma, Y. S. Kim, R. H. Kim, S. D. Wang, J. Wu, S. M. Won, H. Tao, A. Islam, K. J. Yu, T. I. Kim, R. Chowdhury, M. Ying, L. Z. Xu, M. Li, H. J. Chung, H. Keum, M. McCormick, P. Liu, Y. W. Zhang, F. G. Omenetto, Y. G. Huang, T. Coleman and J. A. Rogers, *Science*, 2011, **333**, 838–843.
- 346 D. H. Kim, J. Z. Song, W. M. Choi, H. S. Kim, R. H. Kim, Z. J. Liu, Y. Y. Huang, K. C. Hwang, Y. W. Zhang and J. A. Rogers, *Proc. Natl. Acad. Sci. U. S. A.*, 2008, **105**, 18675–18680.
- 347 J. H. Chen, M. Ishigami, C. Jang, D. R. Hines, M. S. Fuhrer and E. D. Williams, *Adv. Mater.*, 2007, **19**, 3623–3627.
- 348 S. Das, R. Gulotty, A. V. Sumant and A. Roelofs, *Nano Lett.*, 2014, **14**, 2861–2866.
- 349 F. Withers, O. Del Pozo-Zamudio, A. Mishchenko, A. P. Rooney, A. Gholinia, K. Watanabe, T. Taniguchi, S. J. Haigh, A. K. Geim, A. I. Tartakovskii and K. S. Novoselov, *Nat. Mater.*, 2015, **14**, 301–306.
- 350 M. Yagmurcukardes, R. T. Senger, F. M. Peeters and H. Sahin, *Phys. Rev. B: Condens. Matter Mater. Phys.*, 2016, **94**, 245407.

- 351 J. W. Li, N. V. Medhekar and V. B. Shenoy, *J. Phys. Chem. C*, 2013, **117**, 15842–15848.
- 352 L. Song, L. J. Ci, H. Lu, P. B. Sorokin, C. H. Jin, J. Ni, A. G. Kvashnin, D. G. Kvashnin, J. Lou, B. I. Yakobson and P. M. Ajayan, *Nano Lett.*, 2010, **10**, 3209–3215.
- 353 Q. Wei and X. Peng, *Appl. Phys. Lett.*, 2014, **104**, 372–398.
- 354 H. M. Yan, C. Vajner, M. Kuhlman, L. L. Guo, L. Li, P. T. Araujo and H. T. Wang, *Appl. Phys. Lett.*, 2016, **109**, 032103.
- 355 Y. Tong, F. J. Yi, L. S. Liu, P. C. Zhai and Q. J. Zhang, *Physica B*, 2010, **405**, 3190–3194.
- 356 B. Mortazavi, O. Rahaman, M. Makaremi, A. Dianat, G. Cuniberti and T. Rabczuk, *Physica E*, 2017, **87**, 228–232.
- 357 J. V. N. Sarma, R. Chowdhury and R. Jayaganthan, *Comput. Mater. Sci.*, 2013, **75**, 29–34.
- 358 D. Roundy and M. L. Cohen, *Phys. Rev. B: Condens. Matter Mater. Phys.*, 2001, **64**, 212103.
- 359 H. T. Zhang, J. Tersoff, S. Xu, H. X. Chen, Q. B. Zhang, K. L. Zhang, Y. Yang, C. S. Lee, K. N. Tu, J. Li and Y. Lu, *Sci. Adv.*, 2016, **2**, e1501382.
- 360 D. A. Smith, V. C. Holmberg and B. A. Korgel, *ACS Nano*, 2010, **4**, 2356–2362.
- 361 H. L. Peng, W. H. Dang, J. Cao, Y. L. Chen, W. Wu, W. S. Zheng, H. Li, Z. X. Shen and Z. F. Liu, *Nat. Chem.*, 2012, **4**, 281–286.
- 362 B. Radisavljevic, A. Radenovic, J. Brivio, V. Giacometti and A. Kis, *Nat. Nanotechnol.*, 2011, **6**, 147–150.
- 363 Y. B. Zhou, B. Deng, Y. Zhou, X. B. Ren, J. B. Yin, C. H. Jin, Z. F. Liu and H. L. Peng, *Nano Lett.*, 2016, **16**, 2103–2107.
- 364 S. Bae, H. Kim, Y. Lee, X. F. Xu, J. S. Park, Y. Zheng, J. Balakrishnan, T. Lei, H. R. Kim, Y. I. Song, Y. J. Kim, K. S. Kim, B. Ozyilmaz, J. H. Ahn, B. H. Hong and S. Iijima, *Nat. Nanotechnol.*, 2010, **5**, 574–578.
- 365 K. Kang, S. E. Xie, L. J. Huang, Y. M. Han, P. Y. Huang, K. F. Mak, C. J. Kim, D. Muller and J. Park, *Nature*, 2015, **520**, 656–660.
- 366 K. K. Liu, W. J. Zhang, Y. H. Lee, Y. C. Lin, M. T. Chang, C. Su, C. S. Chang, H. Li, Y. M. Shi, H. Zhang, C. S. Lai and L. J. Li, *Nano Lett.*, 2012, **12**, 1538–1544.
- 367 A. M. van der Zande, P. Y. Huang, D. A. Chenet, T. C. Berkelbach, Y. M. You, G. H. Lee, T. F. Heinz, D. R. Reichman, D. A. Muller and J. C. Hone, *Nat. Mater.*, 2013, **12**, 554–561.
- 368 L. B. Gao, W. C. Ren, H. L. Xu, L. Jin, Z. X. Wang, T. Ma, L. P. Ma, Z. Y. Zhang, Q. Fu, L. M. Peng, X. H. Bao and H. M. Cheng, *Nat. Commun.*, 2012, **3**, 699.
- 369 H. Li, J. M. T. Wu, X. Huang, Z. Y. Yin, J. Q. Liu and H. Zhang, *ACS Nano*, 2014, **8**, 6563–6570.
- 370 Z. Q. Xu, Y. P. Zhang, S. H. Lin, C. X. Zheng, Y. L. Zhong, X. Xia, Z. P. Li, P. J. Sophia, M. S. Fuhrer, Y. B. Cheng and Q. L. Bao, *ACS Nano*, 2015, **9**, 6178–6187.
- 371 Z. X. Lu, L. F. Sun, G. C. Xu, J. Y. Zheng, Q. Zhang, J. Y. Wang and L. Y. Jiao, *ACS Nano*, 2016, **10**, 5237–5242.
- 372 A. Castellanos-Gomez, M. Buscema, R. Molenaar, V. Singh, L. Janssen, H. S. J. van der Zant and G. A. Steele, *2D Mater.*, 2014, **1**, 011002.
- 373 K. Kang, K. H. Lee, Y. M. Han, H. Gao, S. E. Xie, D. A. Muller and J. Park, *Nature*, 2017, **550**, 229–233.
- 374 M. L. Lee, *Nature*, 2017, **544**, 301–302.
- 375 K. Chung, C. H. Lee and G. C. Yi, *Science*, 2010, **330**, 655–657.
- 376 J. Kim, C. Bayram, H. Park, C. W. Cheng, C. Dimitrakopoulos, J. A. Ott, K. B. Reuter, S. W. Bedell and D. K. Sadana, *Nat. Commun.*, 2014, **5**, 4836.